Structure and Dynamics of Glass-Forming Fluids

Dissertation

zur Erlangung des Doktorgrades an der Fakultät
für Mathematik, Informatik und Naturwissenschaften
Fachbereich Physik
der Universität Hamburg

vorgelegt von
Dina Sheyfer
aus Norilsk, Russland

Hamburg
2017

The work described in this thesis is done at the Photon Science division of Deutsches Elektronen-Synchrotron, a Research Centre of the Helmholtz Association.

Gutachter/in der Dissertation:	Prof. Dr. G. Grübel
	Prof. Dr. A. Mews
Gutachter/in der Disputation:	Prof. Dr. G. Grübel
	Prof. Dr. A. Mews
	Prof. Dr. A. Pearson
	Prof. Dr. W. Hansen
	Prof. Dr. M. Schnell
Datum der Disputation:	27.03.2018

ABSTRACT

Colloidal dispersions are ubiquitous in our daily life and find numerous applications in industry and science. They are in particular used as a model system to study phase transitions in soft matter systems. In this thesis charge stabilized colloidal particles have been studied at different particle and electrolyte concentrations in the vicinity of the glass transition. Structural and dynamical properties of the system have been investigated by means of X-ray scattering methods. X-ray Photon Correlation Spectroscopy was employed to uncover the dynamics of the system. It revealed a dramatic slow down of the sample dynamics with increasing particle concentration and decreasing concentration of the electrolyte. The average structural properties were investigated by Small Angle X-ray Scattering. X-ray Cross Correlation Analysis allowed to study higher order structural correlations and investigate the local orientational order in the sample. The degree of higher order correlations was shown to increase for higher particle concentrations. Dominant components of local orientational order were observed for low particle concentrations and high electrolyte concentrations. In the glassy phase the behavior of higher order correlations is significantly distinct from a constant behavior of pair correlations.

ZUSAMMENFASSUNG

Kolloidale Dispersionen sind in unserem täglichen Leben allgegenwärtig und finden vielfach Anwendung in Industrie und Wissenschaft. Sie werden insbesondere als Modelsysteme zur Untersuchung von Phasenübergängen weicher Materie benutzt. Im Rahmen dieser Arbeit wurden ladungsstabilisierte Kolloide mit unterschiedlichen Teilchen- und Elektrolytkonzentrationen im Bereich ihres Glasübergangs untersucht. Strukturelle und dynamische Eigenschaften des Systems wurden mittels Röntgenstreumethoden analysiert. Dabei wurde Röntgenphotonenkorrelationsspektroskopie eingesetzt, um die Dynamik des Systems zu charakterisieren. So wurde eine starke Verlangsamung der Probendynamik mit ansteigender Partikel- und abfallender Elektrolytkonzentration beobachtet. Die mittlere Struktur wurde dagegen mithilfe von Röntgenkleinwinkelstreuung untersucht. Die Röntgenkreuzkorrelationsanalyse ermöglichte eine Untersuchung höherer Ordnungen struktureller Korrelationen und somit eine Bestimmung lokaler Orientierungsordnung in der Probe. Der Ordnungsgrad der Korrelationen steigt für hohe Partikelkonzentrationen. Für niedrige Partikel- und hohe Elektrolytkonzentrationen wurden dominante Symmetrien der lokalen Ordnung ermittelt. Dabei wurde deutlich, dass sich die Ausprägung der Korrelationen höherer Ordnung in der Glasphase deutlich von dem konstanten Verhalten der Paarkorrelationen unterscheidet.

CONTENTS

INTRODUCTION

Colloidal systems are found everywhere in our daily life – from food products to medical solutions. These systems comprise small nanometer sized particles dispersed in homogeneous molecular media. Colloidal dispersions are of increasing scientific interest not only because of their practical applications, but also because of their significance for fundamental research. They bear many similarities to atomic- and molecular-scale systems. However, the length and time scales of processes in colloidal systems are much longer and therefore can be easily accessed by various experimental techniques. This makes them an ideal model system for the study of fundamental phenomena which are not yet fully understood. One of these phenomena is the glass transition which is observed in many systems. Upon approaching the glass transition, the dynamics of the system slowdown by several orders of magnitude while the average structural properties remain almost unchanged. Colloidal systems can exist in several different states, e.g. fluid-like, glassy, or crystalline, owing to the nature of the inter-particle interactions. Phase transitions can be induced in a variety of ways, e.g. by changing the particle concentration or interaction strength. The latter can be tuned with high accuracy using e.g. chemical processes or temperature variations.

The structural and dynamical properties of colloidal systems can be studied by a variety of methods. Especially suited for this purpose are X-ray scattering techniques. Short wavelengths, less than the size of a colloidal particle and high penetration depth permit detailed investigation of colloidal dispersions in different states. Spatially averaged information can be accessed by Small Angle X-ray Scattering (SAXS) measurements, which are widely used for this purpose. Besides that, the local orientational order can be studied by X-ray Cross Correlation Analysis (XCCA). Moreover, the dynamical properties of the system can be investigated by means of X-ray Photon Correlation Spectroscopy (XPCS). The combination of these techniques can shine new light and provide connections between dynamical and structural properties of the system undergoing a phase transition.

The aim of this thesis is to synthesize a charge stabilized colloidal dispersion as a model system for a glass forming fluid and subsequently study its dynamical and structural properties by combining different coherent X-ray scattering methods:

SAXS, XPCS and XCCA. Of particular interest is the behavior of the structural and dynamical parameters of the system in the vicinity of the glass transition as a function of particle concentration and interaction strength. The findings may advance our understanding of phase transitions and elucidate important aspects of the system behavior.

This thesis has been written within the CUI (The Hamburg Centre for Ultrafast Imaging) research project C.1.1: "Correlation and Dynamics in Disordered Model Systems".
The layout of the thesis is as follows:

- In CHAPTER 1 an overview on colloidal systems is given.
- Following CHAPTER 2 describes the theoretical basis of the X-ray scattering methods applied in this thesis.
- CHAPTER 3 describes the sample preparation procedure and X-ray scattering experiments.
- In CHAPTER 4 the data analysis and results of dynamical and structural investigations together with the interpretation are given.
- SUMMARY AND OUTLOOK comprises a short description of the obtained results and ideas for future studies.

CHAPTER 1

COLLOIDAL SYSTEMS

1.1 Introduction

Colloids (colloidal dispersions) are complex systems consisting of two different matter phases: a dispersed phase that is distributed in a continuous dispersion phase. Particles of the dispersed phase of a colloidal system have characteristic dimensions between 1 nm and 1 μm [1]. The particles are larger than the molecules of the dispersion phase, but still small enough to undergo thermally activated Brownian motion [2] that counteracts particle sedimentation.

Colloids are ubiquitous in our daily life, e.g. as detergents, clays, paints, milk and inks. They are of high interest and relevance to the modern technology and find numerous applications in medicine, light industry (coatings, food, and cosmetics), and applied science fields such as production of photonic crystals [3–6].

Depending on the nature of the dispersed and continuous phases colloidal system can be classified as sol, emulsion, foam or aerosol (Table 1.1) [7].

Table 1.1: Types of colloids with examples.

Type of colloids	Dispersed phase	Dispersion medium	Examples
Sol	solid	liquid	paints, toothpaste, clay slurry
Emulsion	liquid	liquid	milk, butter, mayonnaise
Foam	gas	liquid or solid	expanded plastic, fire-extinguisher foam, microporous carbons
Aerosol	liquid or solid	gas	fog, mist, industrial smokes

This thesis deals with research on sols – colloidal systems of solid state particles dispersed in a fluid dispersion medium. They are frequently used as scaled-up models of atomic and molecular systems [8,9]. Because of the large size of a colloidal particle compared to atoms, both the spatial structure and dynamics of colloids are experimentally much easier accessible than it is the case for atomic and molecular systems. It enables the use of colloids as a model system to study processes in atomic systems,

especially the phenomena related to phase transitions such as nucleation [10], melting and freezing [11], and the glass transition [12].

1.2 Particle attraction

The behavior of colloidal systems is determined by the interactions between colloidal particles. Colloidal particles exist in a large variety of shapes [13–15]. However, in the following the particles are considered to be spherical to simplify the description of interactions.

In a dispersion colloidal particles attract each other mainly due to van der Waals forces, caused by interaction between the fluctuating electromagnetic fields of the particles [16]. According to Hamaker [17], the energy of van der Waals interaction between two spheres of radius R with a center-to-center distance r is

$$U_{vdW}(r) = -\frac{A_H}{6}\left[\frac{2R^2}{r^2-4R^2} + \frac{2R^2}{r^2} + \ln\left(1-\frac{4R^2}{r^2}\right)\right], \tag{1.1}$$

where A_H is the Hamaker constant that depends on the material properties of the colloidal particles and the surrounding medium. In order to avoid agglomeration due to the van der Waals forces the particles have to be stabilized by introducing a repelling force. Possible mechanisms of particle stabilization are steric and electrostatic stabilization [16]. Colloidal particles studied in this work are electrostatically stabilized. The electrostatic stabilization is discussed in the following section.

1.3 Electrostatic stabilization

In electrostatically (charge) stabilized systems some of the ionisable groups (e.g. $-SO_3H$, $-COOH$) on the particle's surface can dissociate in a polar solvent (e.g. water) resulting in charged colloidal particles. These particles can be considered as micro-ions. The dissociated counter-ions dispersed in the surrounding medium form an ionic cloud around the colloidal particles resulting in an electric double layer. The schematics of a charge stabilized system is illustrated in Fig. 1.1. If two charged particles approach each other their electric double layers overlap, thus causing a repulsive force that prevents particle agglomeration. The interaction between two isolated micro-ions with radius R separated by the center-to-center distance r can be described by the long-range, screened Coulomb (Yukawa) potential [18]

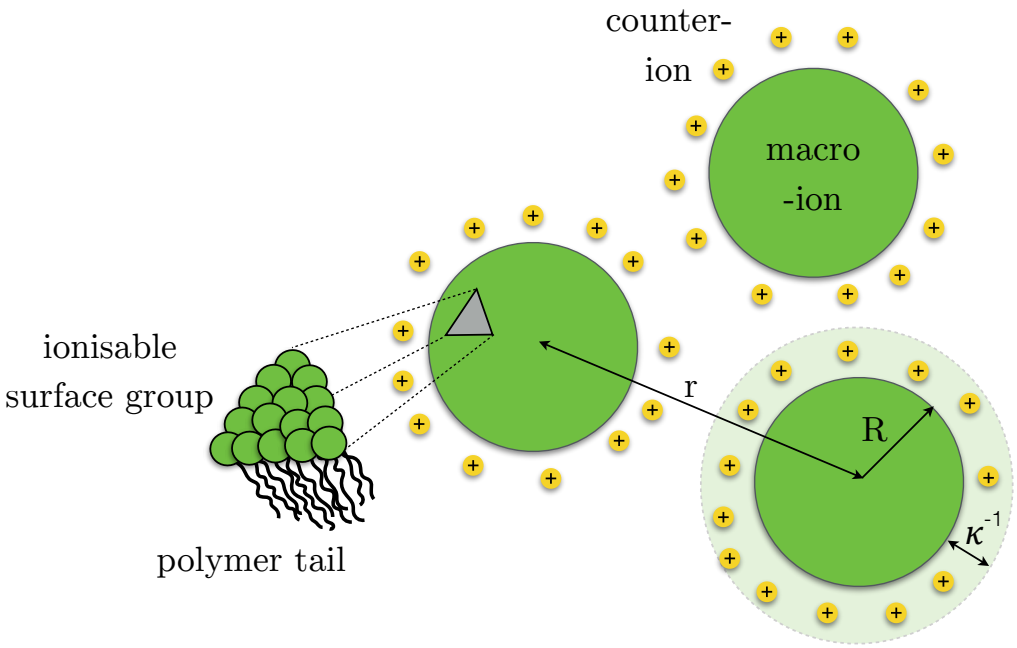

Figure 1.1: Schematic representation of polymeric particles in a charge stabilized system. R is a radius of the colloidal particle, r is the interparticle distance and κ^{-1} is the Debye-Hückel screening length.

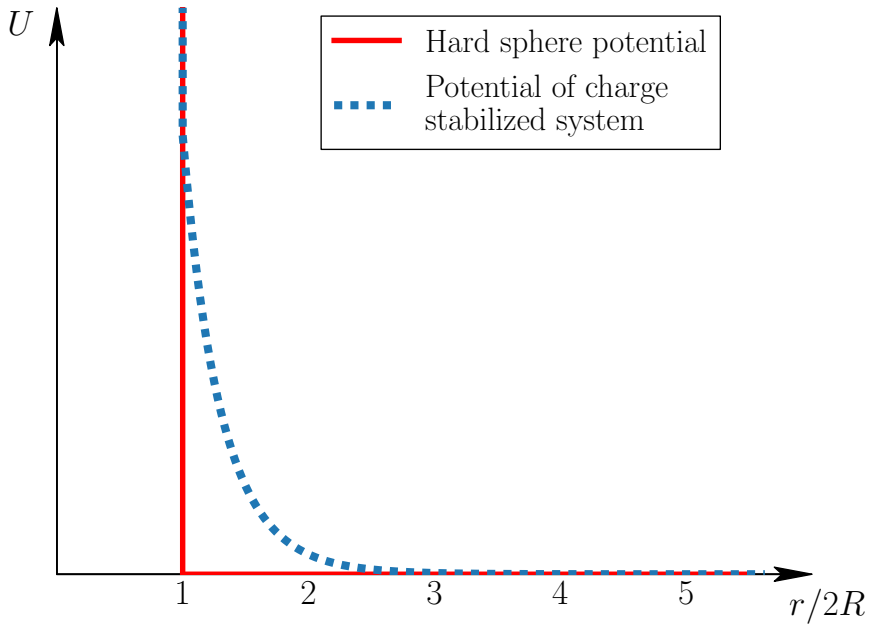

Figure 1.2: Particle interaction potential as a function of the normalized interparticle distance $r/2R$ in colloidal systems.

$$\frac{U_Y(r)}{k_BT} = \begin{cases} \infty, & \text{if } r \leq 2R \\ \dfrac{e_0^2 Z_{\text{eff}}^2}{4\pi\epsilon\epsilon_0 k_B T}\left[\dfrac{e^{\kappa R}}{1+\kappa R}\right]^2 \dfrac{e^{-\kappa r}}{r}, & \text{if } r > 2R \end{cases} . \tag{1.2}$$

The pair interaction potential is shown in Fig. 1.2. In eq. (1.2) k_B is the Boltzmann constant, T is the absolute temperature, e_0 is the elementary charge and Z_{eff} is the effective number of charges per colloidal particle. ϵ_0 is the vacuum dielectric constant and ϵ the relative dielectric permittivity of the solvent. The parameter κ in eq. (1.2) is the inverse Debye-Hückel screening length and is described by the expression

$$\kappa^2 = \frac{e_0^2(n_p Z_{\text{eff}} + 2n_s)}{k_B T \epsilon_0 \epsilon} , \tag{1.3}$$

where n_p is the number density of colloidal particles and n_s the number density of monovalent electrolyte in the solvent. In the absence of ions in the solvent the screening length $\kappa R \to 0$ and the colloidal particles strongly interact with each other through the long-range Coulomb force. In the limit of $\kappa R \to \infty$ the interaction potential becomes strongly screened and the system behavior is similar to the hard sphere case [16, 19]. The hard sphere interaction potential is shown in Fig. 1.2. For strongly screened potentials the van der Waals attraction between colloidal particles can dominate. Such systems can be inherently unstable, causing the particles to aggregate into clusters and, eventually, precipitate due to gravitation [18, 20].

1.4 Colloidal phase behavior

Like atomic and molecular systems, colloidal dispersions can exhibit different phases: liquid, crystal, glass [19, 21–23]. The most frequently studied phase changes in colloidal dispersion are observed in colloidal hard sphere systems [21, 24–30]. The phase transitions depend on the particle volume fraction

$$\phi = N\frac{V_p}{V} , \tag{1.4}$$

where N is the total number of particles in the system of total volume V, and V_p is the single particle volume. The phase diagram of a monodisperse hard spheres system as a function of the volume fraction ϕ is shown in Fig. 1.3. Following the increase of volume fraction, colloidal hard spheres can undergo a transition between liquid, crystal, and glassy phases.

The fluid-crystal transition of the hard spheres system has been studied in several theoretical and experimental works [21, 24–26, 28]. The hard sphere system exhibits

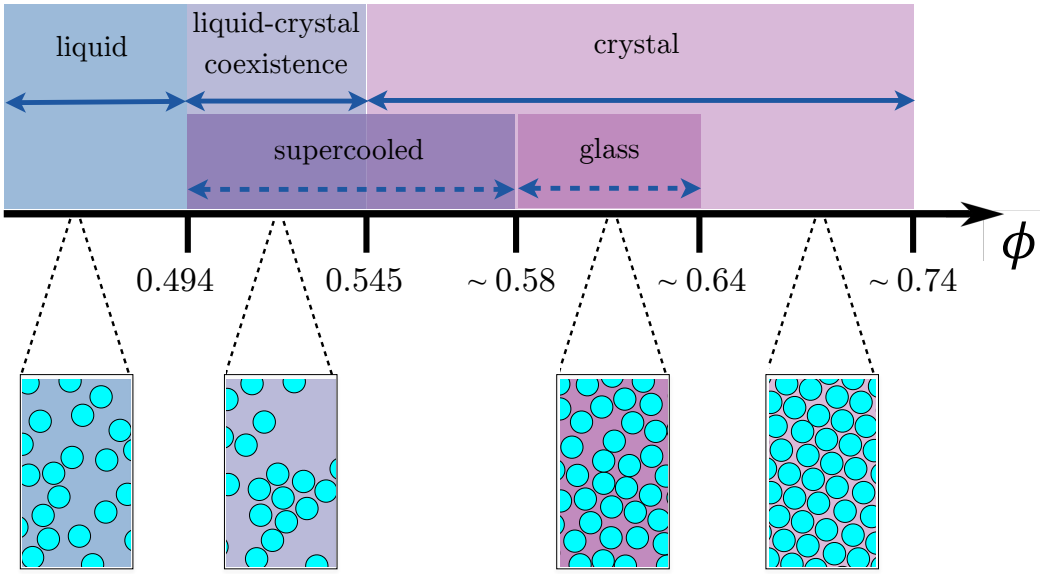

Figure 1.3: Phase diagram of monodisperse hard spheres as a function of volume fraction ϕ. (modified from [33])

liquid phase behavior below the particle volume fraction $\phi_f = 0.494$, while above $\phi_m = 0.545$ the system is in a crystalline state (see Fig. 1.3). A glassy phase can be formed by increasing the volume fraction fast enough to avoid crystallization. The glass state can be observed above volume fraction $\phi \sim 0.58$ up to $\phi \sim 0.64$ [28]. Several other phases (e.g. liquid-crystal coexistence) are observed in hard sphere systems [27, 29, 30]. It has been shown in several studies [31, 32] that the size polydispersity shifts the boundaries between liquid and crystal phases to slightly higher volume fraction values.

In contrast to the hard sphere case the phase diagram of a charge stabilized system not only depends on the volume fraction but also on the particle charge. The long-range electrostatic interaction between charged particles introduces ordering to the system even at volume fractions ϕ as low as 0.01, where the interparticle distance is about several particle diameters [22, 23, 34–38].

In addition, the particle interaction can be tuned by screening the surface charge, achieved by adding salt to the colloidal dispersion [23, 39–41]. Hence, the phase diagram is more complex than for hard sphere systems. The phase diagram of charge stabilized colloids has been determined by mean-field theory [42], computer simulations [38, 43–45] and experiments [22, 23, 36, 46, 47]. The first complete phase diagram of charge stabilized colloids was measured by Sirota et al. [22] by means of synchrotron Small Angle X-ray Scattering (for methods see Chapter 2). The phase diagram is shown in Fig. 1.4 as a function of volume fraction ϕ and salt concentration. At a constant salt concentration the system undergoes glassy-crystal-liquid transition

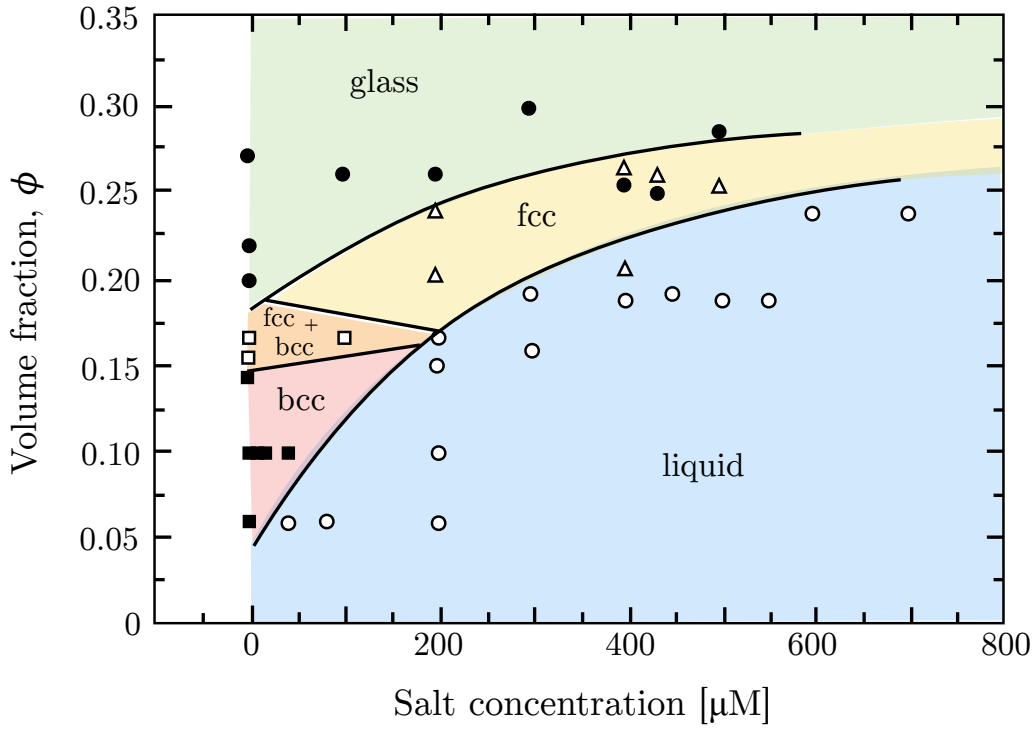

Figure 1.4: Phase diagram of charge stabilized colloidal particles as a function of volume fraction ϕ and salt concentration (KCl). Solid squares - bcc crystal; open triangles - fcc crystal; open squares - bcc + fcc coexistence; solid circles - glass; open circles - liquid. Solid lines for phase boundary are 'guided to eye'. (Redrawn from [22])

with decreasing volume fraction. The ordered phases - fcc (face-centered-cubic), bcc (body-centered-cubic), and coexistant fcc and bcc - are observed at smaller volume fractions compared to the hard sphere system. At high salt amounts the particle charge can be screened and the phase diagram resembles the hard sphere case.

CHAPTER 2

X-RAY METHODS FOR COLLOID STUDIES

2.1 Introduction

In 1895 Wilhelm Conrad Röntgen discovered that highly penetrating radiation of unknown nature is emitted when fast electrons strike on matter [48]. He called that intriguing radiation X-rays.

It is well known nowadays that X-rays are electromagnetic radiation with wavelengths in the range from about 0.1 to about 100 Å. The striking features of X-rays are wavelengths of atomic scale, the ability to penetrate deeply into optically opaque materials, and the high energy of individual X-ray photons comparable to and larger than atomic electron's binding energies. These and other properties of X-rays give rise to a wide spectrum of medical, industrial, and scientific applications.

Since the early 20th century scientists have been using X-ray scattering techniques to probe the structure of matter. Among these techniques Small Angle X-ray Scattering (SAXS) is a suitable method to investigate soft matter systems, in particular colloidal dispersions, which are the focus of this thesis. This method allows determining, for instance, the size and shape of colloidal particles, and in case of high particle concentration the interaction between particles. The basic concepts and equations used to interpret SAXS experiments are adapted from [49] and will follow in the first part of the chapter (sections 2.2 – 2.4).

In the last decades new types of experiments have become available thanks to evolution of X-ray sources. Among them are the two methods employed in this thesis: X-ray Photon Correlation Spectroscopy (XPCS) and X-ray Cross Correlation Analysis (XCCA). These coherent scattering techniques provide information on sample dynamics and local orientational order far beyond conventional SAXS methods. The coherence properties of X-ray radiation and coherent methods will be discussed in sections 2.5 – 2.7.

2.2 Elastic scattering

X-ray radiation scatters through interaction with the electron density of a material. Consider a sample with spatially inhomogeneous electron density (e.g. colloidal particles randomly dispersed in a fluid) and a plane monochromatic X-ray wave incident on the sample. The electric field at position $\mathbf{r}$ and time t (for simplicity the magnetic field is neglected) of the wave is given by

$$\mathbf{E}(\mathbf{r},t) = \hat{\epsilon} E_0 e^{i(\mathbf{k}_{\text{in}}\mathbf{r}-\omega_{\text{in}}t)} \,, \tag{2.1}$$

where $\hat{\epsilon}$ is the polarization unit vector, E_0 is the amplitude of the electric field and ω_{in} its frequency. $\mathbf{k}_{\text{in}}$ is the wave vector and its amplitude is inversely proportional to the wavelength λ of the incoming wave

$$|\mathbf{k}_{\text{in}}| = k = \frac{2\pi}{\lambda} \,. \tag{2.2}$$

In the classical description of X-ray scattering, when such a wave passes through the sample, electrons in the illuminated volume start oscillating at the same frequency as the incoming radiation and thus become sources of secondary waves. These waves have different phase shifts, but their frequencies stay the same (elastic scattering) and thus waves can interfere with each other. A typical scattering scheme is shown in Fig. 2.1.

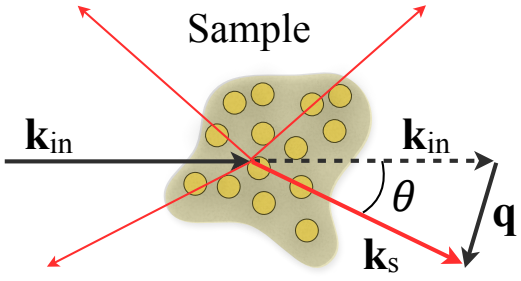

Figure 2.1: Schematic representation of scattering geometry. The incident X-ray radiation with the wave vector $\mathbf{k}_{\text{in}}$ is scattered by the sample into different directions (red arrows) with scattered wave vectors $\mathbf{k}_{\text{s}}$. Scattered radiation observed at the angle θ from the incident wave can be described by the wave vector transfer $\mathbf{q}$ (see eq. (2.3)).

Consider a scattered wave propagating in the direction characterized by the scattering wave vector $\mathbf{k}_{\text{s}}$. The wave vector transfer $\mathbf{q}$ can be then introduced as

$$\mathbf{q} = \mathbf{k}_{\text{s}} - \mathbf{k}_{\text{in}} \,. \tag{2.3}$$

In case of elastic scattering the moduli of scattered and incident wave vectors are equal

$$|\mathbf{k}_{\text{in}}| = |\mathbf{k}_{\text{s}}| \,. \tag{2.4}$$

From eq. (2.2) – (2.4) the magnitude of the scattering vector $\mathbf{q}$ can be derived as

$$q = \frac{4\pi}{\lambda} \sin\left(\frac{\theta}{2}\right) , \tag{2.5}$$

where the scattering angle θ is the angle between wave vectors $\mathbf{k}_{\text{in}}$ and $\mathbf{k}_{\text{s}}$.

2.3 Total scattered intensity

In the following section the expressions for the total scattered amplitude (or intensity) for different systems are derived and discussed. Assuming elastic scattering only, the total wave amplitude is the sum of all scattered amplitudes and the scattered intensity is given by the absolute square of the resulting amplitude: $I(\mathbf{q}) = |A(\mathbf{q})|^2$.

2.3.1 Scattering on single electron

Consider the most elementary scattering process of X-rays on a single free electron. The derivation of the amplitude of the electromagnetic field emitted by an oscillating electron can be found in [50]. The elastically scattered intensity is the square of the amplitude and it is given by well known Thomson formula [49]

$$I = I_0 r_e^2 \frac{\Pi}{L^2} , \tag{2.6}$$

where $I_0 = |E_0|^2$ is the intensity of the incident beam, L is the distance to the observation point and r_e is the classical electron radius or Thomson scattering length ($r_e = 2.82 \times 10^{-5}$Å). Π is the polarization factor describing the effect of the X-ray beam polarization and is given by [50]

$$\Pi = \begin{cases} 1 & \sigma - \text{polarization} \\ \cos^2(\theta) & \pi - \text{polarization} \\ \dfrac{1+\cos^2(\theta)}{2} & \text{unpolarized incident beam} \end{cases} , \tag{2.7}$$

where θ is the scattering angle. In case of σ-polarization the direction of oscillation of the electric field is normal to a scattering plane [1], for π-polarization electric field oscillations occur in-plane. In the frame of this thesis X-rays are polarized linearly in the horizontal plane of the synchrotron (see section 2.5). In case of small scattering angles that is in the interest of this work the polarization factor can be approximated to 1.

2.3.2 Scattering on multiple electrons

Consider the wave scattered by an electron located at the origin of the system and by another located at a position **r** (see Fig. 2.2). In the following the scattering process is described in the far-field limit (Fraunhofer diffraction) [51] and the incident and scattered X-rays can be represented as plane waves. The scattered amplitudes only

[1] Scattering plane is a plane formed by the wave vectors of the incident and the scattered waves.

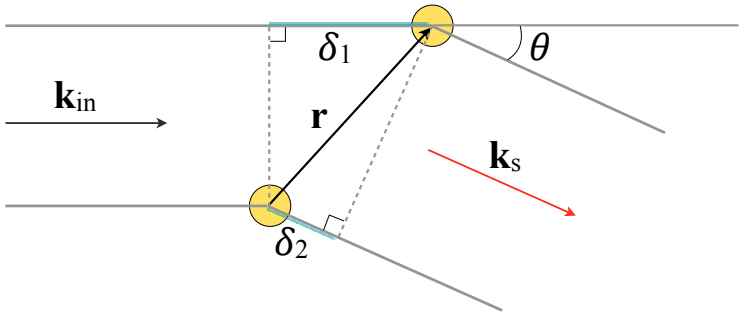

Figure 2.2: Schematic representation of the scattering process by two electrons. The incident and the scattered waves are denoted as $\mathbf{k}_{\text{in}}$ and $\mathbf{k}_{\text{s}}$, respectively. Scattered waves from the two electrons have a path difference of $\delta = \delta_1 - \delta_2$. The lengths δ_1 and δ_2 are projections of the electron-electron distance vector $\mathbf{r}$ on the wave vectors $\mathbf{k}_{\text{in}}$ and $\mathbf{k}_{\text{s}}$, respectively.

differ by their phase ν, which depends on the electron location in space. The phase shift $\Delta\nu$ is defined by $2\pi/\lambda$ times the difference in the optical path, thus

$$\Delta\nu = \frac{2\pi}{\lambda}(\delta_1 - \delta_2) = \mathbf{k}_{\text{in}}\mathbf{r} - \mathbf{k}_{\text{s}}\mathbf{r} = -\mathbf{q}\mathbf{r} \; . \tag{2.8}$$

The total scattering amplitude $A(\mathbf{q})$ of N electrons is the sum of the scattered waves with a phase factor of $e^{-i\mathbf{q}\mathbf{r}}$

$$A(\mathbf{q}) = \frac{E_0}{L}\sum_j^N r_e e^{-\mathrm{i}\mathbf{q}\mathbf{r}_j} \; . \tag{2.9}$$

Introducing a continuous electron density $\rho_e(\mathbf{r})$ the volume element d$\mathbf{r}$ will contain $\rho_e(\mathbf{r})$d$\mathbf{r}$ electrons and the total scattered amplitude can be expressed as

$$A(\mathbf{q}) = \frac{E_0}{L} r_e \int \rho_e(\mathbf{r}) e^{-\mathrm{i}\mathbf{q}\mathbf{r}} \mathrm{d}\mathbf{r} \; . \tag{2.10}$$

Thus, the amplitude $A(\mathbf{q})$ is the Fourier transform of the electron density distribution and the momentum transfer $\mathbf{q}$ is the reciprocal space coordinate.

2.3.3 Scattering on identical particles

In case of the scattering on an atom eq. (2.10) can be re-written in the form

$$A_{\text{atom}}(\mathbf{q}) = \frac{E_0}{L} r_e f^{at}(\mathbf{q}) \; , \tag{2.11}$$

where f^{at} is the atomic form factor, which when multiplied by r_e gives the scattering length of an atom. The scattering amplitude of N atoms labeled by index j can be

calculated as

$$A_{\text{atoms}}(\mathbf{q}) = \frac{E_0}{L} r_e \sum_j^N f_j^{at}(\mathbf{q}) e^{-\mathrm{i}\mathbf{q}\mathbf{r}_j} \ , \tag{2.12}$$

where $f_j^{at}(\mathbf{q})$ is the form factor of the j'th atom and $\mathbf{r}_j$ defines its position.

Eq. (2.9) and eq. (2.12) can be generalized for the case of N identical scatterers (atoms, molecules, colloidal particles)

$$A(\mathbf{q}) = \frac{E_0}{L} \sum_j^N F(\mathbf{q}) e^{-i\mathbf{q}\mathbf{r}_j} \ , \tag{2.13}$$

where $F(\mathbf{q})$ is the amplitude form factor of a scatterer in the units of r_e. $F(\mathbf{q})$ can be determined by integration over the particle volume V_p

$$F(\mathbf{q}) = \int_{V_p} \Delta\rho(\mathbf{r}) e^{-\mathrm{i}\mathbf{q}\mathbf{r}} \mathrm{d}\mathbf{r} \ , \tag{2.14}$$

where the density contrast $\Delta\rho$ is given by

$$\Delta\rho(\mathbf{r}) = \rho(\mathbf{r}) - \tilde{\rho} \ . \tag{2.15}$$

In eq. (2.15) $\rho(\mathbf{r}) = r_e \rho_e(\mathbf{r})$ is the scattering length density at position $\mathbf{r}$ and $\tilde{\rho}$ is the mean scattering length density of the surrounding medium. The corresponding scattered intensity of N particles is

$$I(\mathbf{q}) = |A(\mathbf{q})|^2 = \frac{I_0}{L^2} \left| \sum_j^N F(\mathbf{q}) e^{-\mathrm{i}\mathbf{q}\mathbf{r}_j} \right|^2 \ . \tag{2.16}$$

Although eq. (2.16) has the same form for scattering from atoms, molecules or particles, the scattering from these systems will differ mainly in the scattering angle (or wave vector $\mathbf{q}$). According to the Bragg formula [51] the characteristic structural sample size d and scattering angle θ are inversely related

$$d \sim \frac{\lambda}{\sin(\theta/2)} \ . \tag{2.17}$$

Therefore, for large objects compared to the X-ray wavelength, e.g. colloidal particles studied in this thesis, the scattered intensity has to be recorded at small angles which corresponds to small $\mathbf{q}$ vectors. Thus, small angle scattering experiments are dedicated for such samples.

2.4 Small Angle X-ray Scattering (SAXS)

SAXS is based on elastic scattering and is a tool for probing structure in the nanometer to micrometer range by measuring scattering intensities at angles θ close to 0°[2]. SAXS studies started from the classical work of A. Guinier, published in 1938 [53]. The theoretical and experimental fundamentals of SAXS are described by Guinier and Fournet [54]. Since that time much progress has been made in instrumentation of SAXS and in computational methods for extracting structural information from SAXS data [49, 55–59]. A lot of computer software is available nowadays for modeling of SAXS data.

In the framework of this thesis SAXS is the technique of choice to study colloidal dispersions. Since the size of colloidal particles ($\sim$100 nm) is much larger than the wavelength of X-rays ($\sim$1 Å), the scattering angles are very small. A typical small angle scattering geometry is shown in Fig. 2.3. The incident X-ray beam impinges on a sample and the scattered intensity is recorded by a two dimensional detector located at distance L from the sample. The transmitted primary beam is absorbed by the beamstop placed in front of the detector. Typically, X-ray detectors measure energy deposited by the radiation. Therefore only the scattered intensity, and not the complex amplitude, can be obtained in an experiment. Note that in an experiment the measured intensity will naturally be a time average taken over the acquisition time. For a given sample the intensity distribution on a detector will depend on the wavelength λ and sample to detector distance.

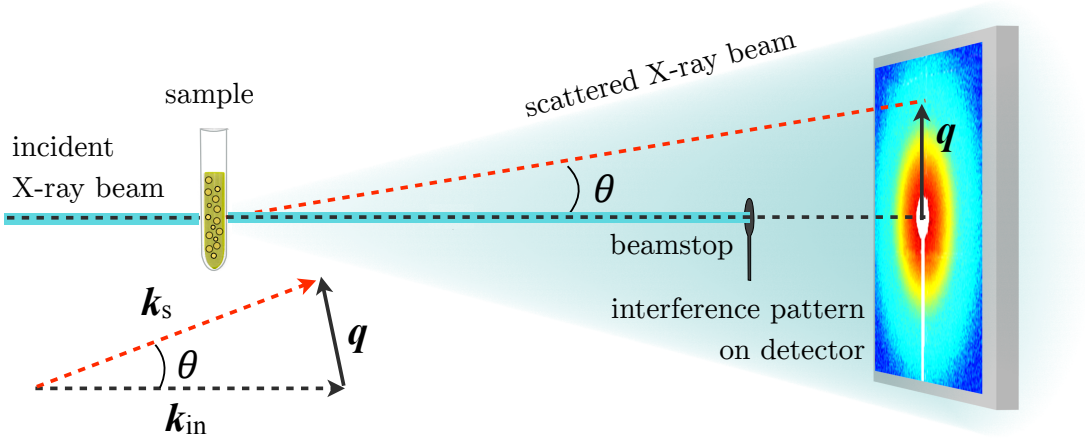

Figure 2.3: Schematic representation of the SAXS scattering geometry. The incident X-ray beam is diffracted by the sample and the resulting pattern is recorded by a 2D detector. The direct beam is blocked by the beamstop.

[2]Typical values of scattering angles are 0.1° – 10°[52].

The scattering patterns from colloidal particles dispersed in solution reflect the size and shape of the colloidal particles and the time averaged spatial distribution of the particles. For identical particles with spherical symmetry the scattered intensity can be expressed as a product of the intensity particle form factor $P(q)$ and the structure factor $S(q)$ which describes the spatial correlation of particles

$$I(q) \sim P(q)S(q) \; . \tag{2.18}$$

In general when particles are neither identical nor spherical objects, it is not always possible to describe $I(q)$ through the two terms $P(q)$ and $S(q)$ without the help of additional models, e.g. the decoupling approximation [60] or local monodisperse approximation [61].

2.4.1 The form factor

For a dilute system containing of N non-interacting identical particles the inter-particle interaction can be neglected. As a consequence the structure factor $S(q) = 1$ and the scattered intensity can be described by the intensity form factor $P(q)$

$$I(\mathbf{q}) = P(\mathbf{q}) = NP_1(\mathbf{q}), \tag{2.19}$$

where $P_1(\mathbf{q})$ is an intensity form factor of a single particle which is connected to the amplitude form factor (see eq. (2.14)):

$$P_1(\mathbf{q}) = |F(\mathbf{q})|^2 = \left| \int_{V_p} \Delta\rho(\mathbf{r}) e^{-\mathrm{i}\mathbf{qr}} \mathrm{d}\mathbf{r} \right|^2 . \tag{2.20}$$

In case of spherical particles with uniform electron density $P(\mathbf{q})$ will depend only on the modulus $q = |\mathbf{q}|$ and not on its direction. Therefore the integral in eq. (2.20) takes the form

$$\int_{V_p} \Delta\rho(\mathbf{r}) e^{-\mathrm{i}\mathbf{qr}} \mathrm{d}\mathbf{r} = 4\pi\Delta\rho \int_0^\infty r^2 \langle e^{-i\mathbf{qr}} \rangle \mathrm{dr} \; , \tag{2.21}$$

where brackets $\langle\rangle$ indicate a spherical average over all orientations. The averaging results in [62]

$$\langle e^{-i\mathbf{qr}} \rangle = \frac{\sin qr}{qr} \; . \tag{2.22}$$

Substituting eq. (2.22) to eq. (2.21) and performing the integration, the intensity form factor for spherical particles with radius R can be obtained from eq. (2.20)

$$P_{\text{sph}}(q) = 9\Delta\rho^2 V_{\text{sph}}^2 \frac{(\sin(qR) - qR\cos(qR))^2}{(qR)^6} \; . \tag{2.23}$$

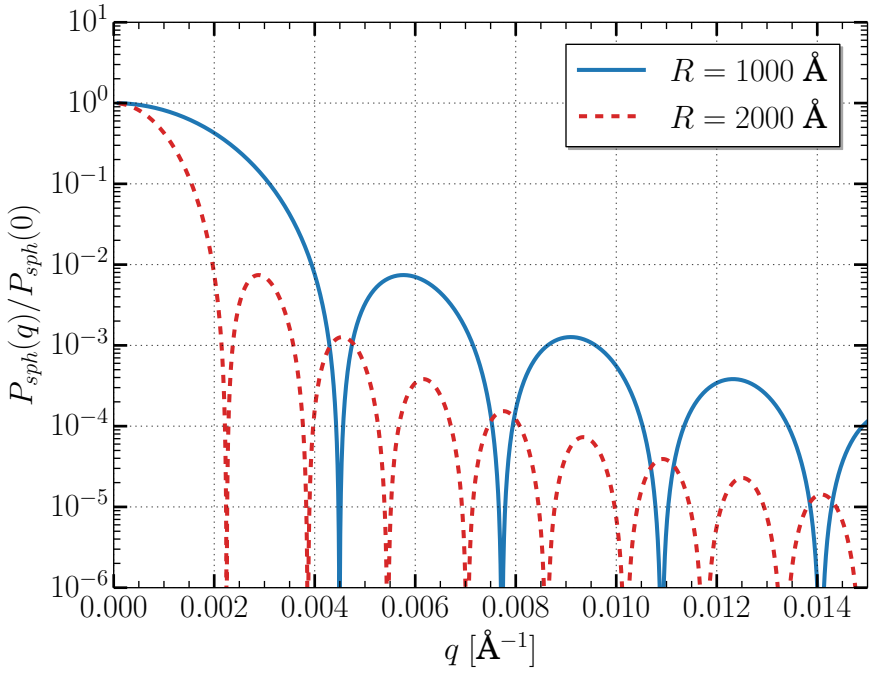

Figure 2.4: Calculated form factors of spherical particles as a function of momentum transfer q. The particle radii are given in the legend.

In Fig. 2.4 form factors of spherical particles normalized on $P_{\text{sph}}(0) = \Delta\rho^2 V_{\text{sph}}^2$ are shown as a function of momentum transfer q for two different sphere radii of 1000 Å and 2000 Å. From eq. (2.23) it follows that $P_{\text{sph}}(q)$ has a first minimum when $qR \simeq 4.49$. The particle radius R can therefore be estimated if the q position of the first minimum is known. The asymptotic behavior at large q (Porod regime [50]) of the form factor of spheres follows a power law such that $P_{\text{sph}}(q) \propto q^{-4}$.

2.4.2 Form factor models for polydisperse systems

Colloidal suspensions consist of many nanoparticles that may not be always monodisperse (e.g. different particle shape and size). In general, if the system consists of K different types of non-interacting particles, the measured scattering intensity can be written as a sum of the intensity form factors of the K types of particles ($P_k(q)$) with coefficients ν_k which describe the corresponding fractions of the solute volume

$$I(q) = P(q) = \sum_{k}^{K} \nu_k P_k(q) \,. \tag{2.24}$$

Consider a system of particles with the same general shape but different sizes.

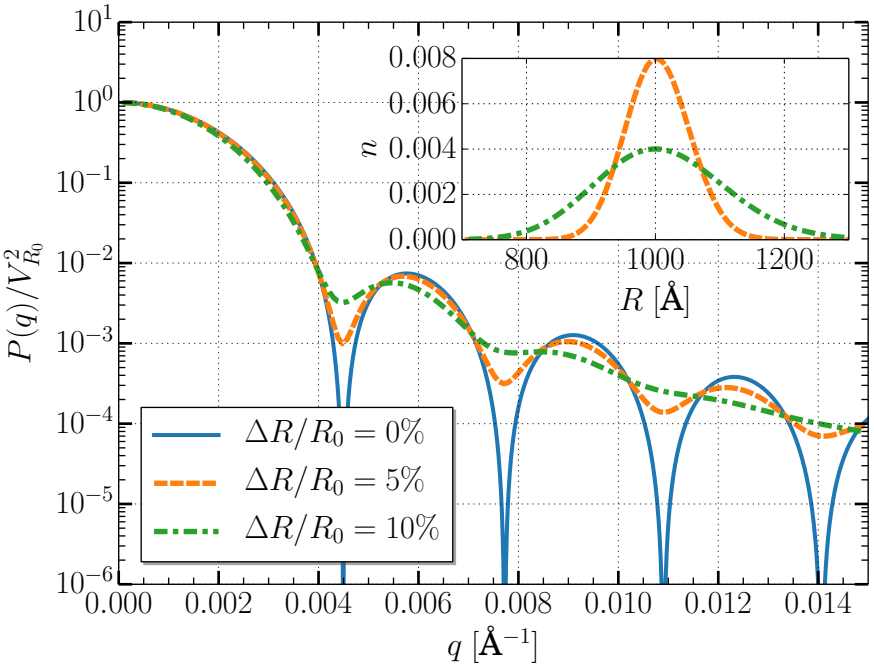

Figure 2.5: Calculated form factors of spherical particles with an average radius $R_0 = 1000$ Å and different size polydispersity. The form factors are normalized to the square of the volume of the particle $V_{R_0} = 4/3\pi R_0^3$. The inset shows the *Schulz-Zimm* (eq. (2.26)) particle radius distribution.

The size polydispersity can be described by a size distribution function, $n(R)$, with $\int n(R)dR = 1$. Therefore the intensity form factor of the system is given by:

$$P(q) = \int n(R) P_1(q, R) dR \,. \tag{2.25}$$

The *Schulz-Zimm* distribution [59] is commonly used to describe polydisperse particles:

$$n(R, R_0, Z) = \frac{1}{(Z+1)!}\left(\frac{Z+1}{R_0}\right)^{Z+1} R^Z \exp\left(-\frac{Z+1}{R_0}R\right), \tag{2.26}$$

R_0 denotes the average size of the particles. The parameter Z relates to the particle polydispersity $\hat{p}$

$$\hat{p} = \frac{\Delta R}{R_0} = \sqrt{\frac{1}{Z+1}} \,. \tag{2.27}$$

Fig. 2.5 shows the form factors of polydisperse spherical particles (in eq. (2.25) P_1 equals P_{sph} from eq. (2.23)) with an average particle radius $R_0 = 1000$ Å and assuming *Schulz-Zimm* distribution. Note that the size distribution is number weighted. The form factor oscillations smear out with increasing polydispersity.

2.4.3 The structure factor

Consider the case of interacting colloidal particles with $S(q) \neq 1$. The scattered intensity in eq. (2.16) can be written in the form

$$I(\mathbf{q}) \sim \sum_{j}^{N}\sum_{j\prime}^{N} F(\mathbf{q})F^{*}(\mathbf{q})e^{-i\mathbf{q}(\mathbf{r}_j-\mathbf{r}_{j\prime})}$$

$$= NP_1(\mathbf{q})\left(1+\frac{1}{N}\sum_{j}^{N}\sum_{j\prime\neq j}^{N} e^{-i\mathbf{q}(\mathbf{r}_j-\mathbf{r}_{j\prime})}\right) . \tag{2.28}$$

Thus, the structure factor $S(\mathbf{q})$ is given by

$$S(\mathbf{q}) = \frac{1}{N}\sum_{j}^{N}\sum_{j\prime}^{N} e^{-i\mathbf{q}(\mathbf{r}_j-\mathbf{r}_{j\prime})} . \tag{2.29}$$

When particles (or particle superstructures) are randomly oriented and distributed homogeneously within a sample, the scattering from the system is isotropic. This situation is equivalent to powder diffraction [50]. The isotropic structure factor $S(q)$ of such a system is related to its radial distribution function or pair distribution function $g(r)$ [62]

$$S(q) = 1 + 4\pi n\int_0^\infty r^2\big(g(r)-1\big)\frac{\sin(qr)}{qr}\mathrm{d}r , \tag{2.30}$$

where n is the particle number density. The pair distribution function $g(r)$ describes the probability to find a particle at a distance r from another particle. Eq. (2.30) suggests that the Fourier transform of $g(r)-1$ is $S(q)-1$, allowing one to connect real and reciprocal space.

The structure factor $S(q)$ depends on the direct particle interaction described by the interaction potential $U(r)$. In a dilute particle solution, the probability of a particular distance between two particles can be described by the Boltzmann distribution and thus $g(r)$ is connected to the interaction potential as

$$g(r) = e^{-U(r)/(k_BT)} \approx 1 - \frac{U(r)}{k_BT} . \tag{2.31}$$

In this case, for a given $U(r)$, $g(r)$ is calculated by eq. (2.31), and then $S(q)$ is computed from $g(r)$ using eq. (2.30).

In the case of concentrated particle dispersions, the many-body system approach is typically used [59] in which a particle interacts with all neighboring particles accounting for both the direct and the indirect interactions. The derivation of the structure factor $S(q)$ in such a system can be achieved with the Ornstein-Zernike integral

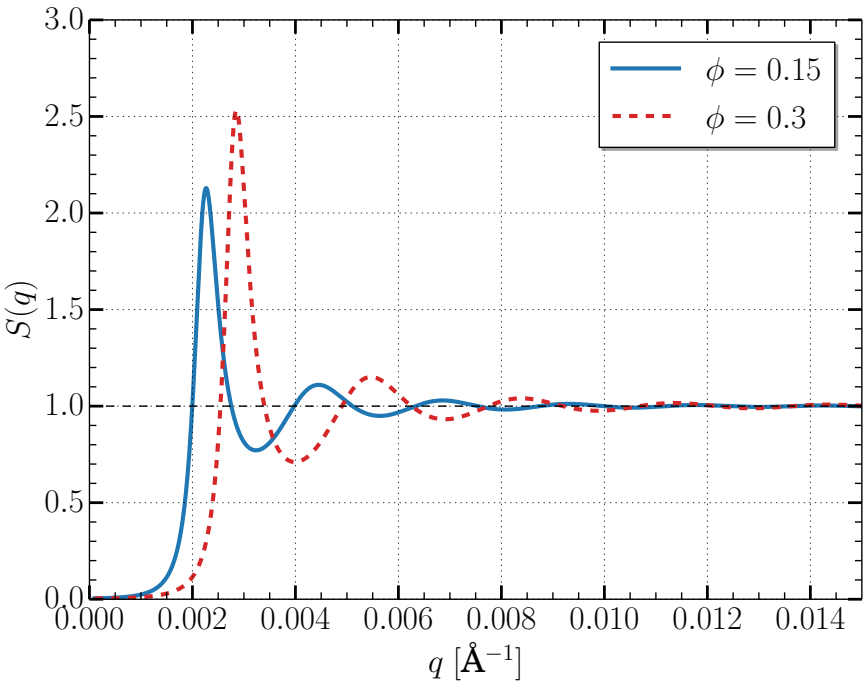

Figure 2.6: Static structure factors $S(q)$ obtained within the RMSA as a function of momentum transfer q. The colloidal particles are dispersed in a medium at temperature $T = 305$ K with a relative dielectric permittivity $\epsilon = 80$. The particle radius is $R = 1000$ Å and effective charge $Z_{eff} = 200e_0$. The volume fractions are given in the legend.

equation (OZ) that connects the total correlation function $h(r) = g(r) - 1$ to the direct two-particle correlation function $c(r)$ [63]. To solve the OZ equation for a given potential, a closure relation [63] is required. In literature several possible closure relations are used [59]. In the case of charge stabilized systems the mean spherical approximation (MSA) and rescaled mean spherical approximation (RMSA) are used [41, 64, 65]. The closure relation in the MSA and RMSA is

$$c(r) = -\frac{U(r)}{k_B T} \,. \tag{2.32}$$

The structure factor can be derived using the following equations:

$$\begin{aligned} C(q) &= 4\pi \int r^2 c(r) \frac{\sin(qr)}{qr} \mathrm{d}r \,, \\ S(q) &= \frac{1}{1 - nC(q)} \,. \end{aligned} \tag{2.33}$$

In Fig. 2.6 the calculated structure factors $S(q)$ of charge stabilized systems are shown. It was obtained within the RMSA with the use of the interaction potential $U_Y(r)$ defined in eq. (1.2) for different particle volume fractions. It is typical that at large momentum transfers q, the structure factor $S(q)$ tends to one due to absence of

long-range order in colloidal dispersion.

In SAXS experiments the structure factor is determined by measuring the scattered intensity $I(q)$ and intensity form factor $P(q)$ (in the non-interacting system). The structure factor $S(q)$ is then extracted with eq. (2.18). It has been shown in several works [41, 66, 67] that eq. (2.18) can be used for systems consisting of spherical particles with certain size polydispersity.

2.5 Coherent X-ray sources and their properties

In the last decades SAXS has become a standard technique at synchrotron light sources. Synchrotron radiation is produced when charged particles travel at relativistic speed in a curved trajectory. Typically, a particle (electron or positron) beam is stored for several hours circulating in a large ring, where bending magnets [50] keep its trajectory round. In the straight sections of the storage ring, so-called insertion devices – wigglers [50] and undulators [68] – can be installed. In the scattering experiments of this work, X-rays emitted in undulators were used to take maximum advantage of the intrinsic brightness of the synchrotron radiation. A schematic sketch of an undulator is shown in Fig. 2.7. An undulator consists of closely spaced vertically oriented dipole magnets with alternating polarity. When electrons pass through the undulator they oscillate in the horizontal plane and at each bend of the trajectory electromagnetic radiation is emitted in a cone. The overlap of the radiation cones gives rise to a constructive interference, resulting in a X-ray beam with high spectral brightness and high degree of coherence (see section 2.5.1). These partially coherent X-ray beams at

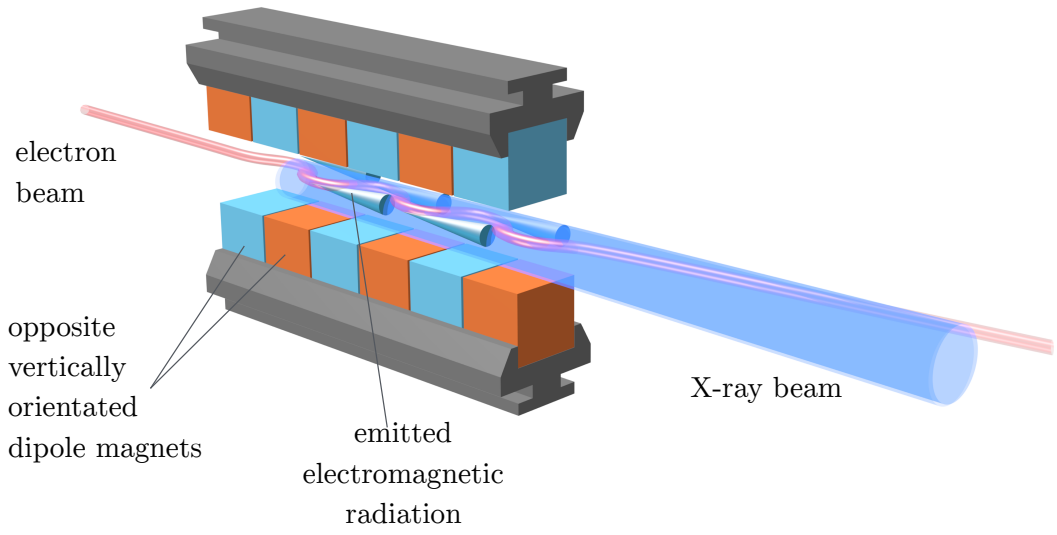

Figure 2.7: Schematic sketch of an undulator X-ray source.

state-of-the-art third generation storage rings [3] [68] opened the way for several types of experimental methods e.g. Coherent X-ray Diffraction Imaging (CXDI) [69], Fourier transform holography [70], ptychography [71], XPCS [72], XCCA [73, 74] and others. XPCS and XCCA experiments performed in SAXS geometry are used in this work. Prior to discussion of these methods the degree of coherence and the coherent properties of the X-ray beam important for these experiments will be discussed.

2.5.1 Coherence of light

The statistical nature of light implies that every electromagnetic field has some fluctuations associated with it. This can be easily illustrated if one considers a composite source which consists of several independent point sources radiating with different frequencies and phases. Due to the superposition of emissions from individual point sources, their total radiation field is random and fluctuates in space and time. These fluctuations can be small, as in the output of a well-stabilized laser, or large, as in the output of a thermal source. However, in both critical cases the fluctuations are too fast to be detected (on the order of 10^{18} s^{-1}), therefore only statistical properties of these fluctuations can be determined. The theory which deals with the statistical description of the various fluctuations present in an optical field is the optical coherence theory. The general framework of the optical coherence theory is well established and can be found in numerous textbooks and publications [75–78].

The most important concept in optical coherence is the degree of correlation between different points in an electromagnetic wave field. The quantitative coherence measure can be introduced as a first order cross correlation function:

$$\Gamma(\mathbf{r}_1, \mathbf{r}_2; t_1, t_2) = \langle E^*(\mathbf{r}_1, t_1) E(\mathbf{r}_2, t_2) \rangle \, . \tag{2.34}$$

It describes the correlation between two complex values of the wave field $E(\mathbf{r}_1, t_1)$ and $E(\mathbf{r}_2, t_2)$ taken at two different locations ($\mathbf{r}_1$ and $\mathbf{r}_2$) and at two different times (t_1 and t_2). The * means complex conjugation and brackets $\langle\rangle$ indicate the ensemble average. This function is also known as the mutual coherence function and its normalized form defines the complex degree of coherence

$$\gamma(\mathbf{r}_1, \mathbf{r}_2; t_1, t_2) = \frac{\Gamma(\mathbf{r}_1, \mathbf{r}_2; t_1, t_2)}{\sqrt{\langle I(\mathbf{r}_1, t_1) \rangle} \sqrt{\langle I(\mathbf{r}_2, t_2) \rangle}} \, , \tag{2.35}$$

where $\langle I(\mathbf{r}, t) \rangle = \langle |E(\mathbf{r}, t)|^2 \rangle$ is an averaged intensity.

[3] For example, ESRF in France, PETRA III in Germany, APS in the USA, SLS in Switzerland, Spring-8 in Japan, and others.

From eq. (2.35) it follows that $|\gamma(\mathbf{r}_1, \mathbf{r}_2; t_1, t_2)|$ lies in the range $0 \leq |\gamma(\mathbf{r}_1, \mathbf{r}_2; t_1, t_2)| \leq 1$ for all values of $\mathbf{r}_1, \mathbf{r}_2; t_1, t_2$. Experimentally this modulus can be obtained via the visibility of interference fringes. Two extreme cases, when $|\gamma(\mathbf{r}_1, \mathbf{r}_2; t_1, t_2)| = 1$ and $|\gamma(\mathbf{r}_1, \mathbf{r}_2; t_1, t_2)| = 0$, characterize fully coherent and completely incoherent light sources, respectively. All intermediate values characterize a partially coherent source. When $\mathbf{r}_1 = \mathbf{r}_2 = \mathbf{r}$ and $t_1 = t_2 = t$ one obtains $\gamma(\mathbf{r}, \mathbf{r}; t, t) = 1$ which means that the field is always coherent with itself in a single point. The degree of coherence typically drops down below 1 as the separation in space $|\mathbf{r}_1 - \mathbf{r}_2|$ and time $t_1 - t_2$ increases. Therefore there is a region throughout space and time where the electromagnetic field is highly correlated. It is called the coherence volume and its size in the spatial and in temporal domain are called transverse and longitudinal coherence length, respectively. These coherence properties usually play an important role in practical cases and will be discussed in the next section.

2.5.2 Coherent X-ray beams

In general, an undulator source is usually considered incoherent, as the radiation produced by different electrons is uncorrelated. However, since the radiation is confined to a narrow cone and due to the large source-to-sample distance and the small source size, the light arriving at the sample is partially coherent. The coherence properties of the photon beam can be described in terms of the transverse and longitudinal coherence lengths ξ_t and ξ_l mentioned above.

The transverse or spatial coherence defines the degree to which the phase of the wave is correlated at two separate points in the plane perpendicular to the direction of the beam propagation. The transverse coherence length ξ_t at distance R_s from the source is determined by the source size s and wavelength λ:

$$\xi_t = \frac{\lambda R_s}{2s} \,. \tag{2.36}$$

This formula comes from the Van Cittert-Zernike theorem [76]. According to this formula, radiation from fully incoherent sources has a non-zero degree of coherence at large distances from the source. In practice, the degree of transverse coherence can be measured in Young's double slit experiments. If the two slits are separated by more than the transverse coherence length ξ_t, the fringes' visibility will be significantly decreased [78].

The longitudinal or temporal coherence describes the phase relation of the emitted radiation in the propagation direction. It is related to the non-monochromaticity of the source, i.e. its spectral bandwidth (BW). The corresponding coherence length

formula arises from the Wiener-Khintchine theorem [76]:

$$\xi_l = \frac{\lambda^2}{2\delta\lambda} \,. \tag{2.37}$$

The longitudinal coherence length ξ_l is the distance over which the two waves with bandwidth $\delta\lambda$ both emitted from one source will interfere destructively. Thus, a narrower BW radiation results in a larger longitudinal coherence. Experimentally the longitudinal coherence can be determined by measuring the path length difference with a Michelson interferometer.

To obtain a coherent beam at a 3rd generation synchrotron source, one has to spectrally and spatially filter the emitted undulator beam. In practice, narrowing the BW $\delta\lambda$ usually can be performed with a monochromator (crystal) or a mirror. The spatial filtering can be performed by cutting the X-ray beam with apertures in order to obtain transverse beam dimensions that are on the order of the transverse coherence length in both horizontal and vertical directions. A sufficient number of photons passes through such apertures only at high-brilliance synchrotron sources. To elaborate, the number of photons per second per unit solid angle from a source of brilliance B is a product of the brilliance and the source size Bs_hs_v/π. s_h and s_v are source sizes in the horizontal and vertical directions, respectively. The coherent flux is the number of photons that pass through the solid angle *i.e.* $\pi\xi_{th}\xi_{tv}/R_s^2$, where ξ_{th} and ξ_{tv} are transverse coherence lengths in horizontal and vertical directions. Thus, the coherence flux is given by:

$$F_c = \frac{Bs_hs_v\xi_{th}\xi_{tv}}{R_s^2} = \frac{\lambda^2}{4}B \,. \tag{2.38}$$

2.5.3 Scattering under coherent illumination: speckle pattern

When (partially) coherent light scatters off a disordered material, constructive and destructive interference from randomly distributed scatterers within the sample leads to a random 'speckled' diffraction pattern. Such a speckle pattern uniquely reflects the exact spatial distribution of scatterers in the illuminated sample volume. It is in a marked contrast to the scattering of incoherent radiation, where speckles are not resolved. Here the scattering pattern is determined only by the probability distribution of the disorder, and so only average sample properties can be studied. Beginning from the 1960s speckle phenomena have been often observed with laser light [79]. Observation of speckles with X-rays has become possible with the advent of 3rd generation synchrotron sources which possess a high brilliance in comparison to previous X-ray sources (e.g. X-ray tubes, 1st and 2nd generation storage rings). In 1991 Sutton et al. [80] first demonstrated that one can get sufficient coherent flux from high-brilliance

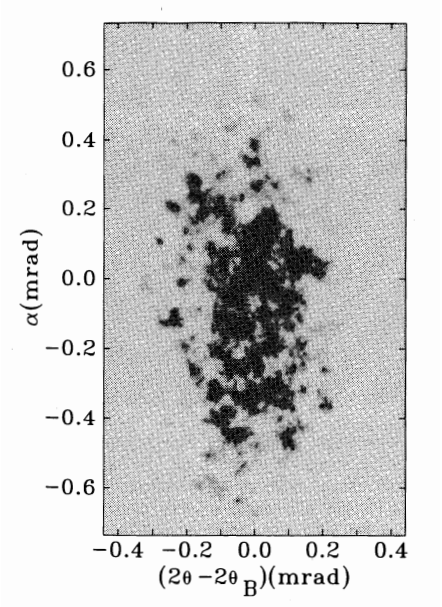

Figure 2.8: Static speckle pattern of a Bragg peak from a Cu_3Au single crystal [80].

synchrotron X-ray sources to observe speckle patterns. In that experiment, performed at NSLS (National Synchrotron Light Source), they observed a static speckle pattern in the diffraction of coherent X-rays from a single crystal of Cu_3Au with randomly arranged antiphase domains (see Fig. 2.8).

A unique advantage of coherent scattering is the ability to study the dynamics of the sample. As the sample evolves with time, so does its speckle pattern. Thus, by studying intensity fluctuations of the speckles one gains information about the underlying sample's dynamics. Analysis of the fluctuations can be performed with X-ray Photon Correlation Spectroscopy (see section 2.6). Although resolving the exact spatial structure of disorder from a speckle pattern may be difficult, the structural information, e.g. local orientational order, can be extracted through spatial correlation of intensity in speckle pattern – X-ray Cross Correlation Analysis (XCCA) (see section 2.7).

2.6 X-ray Photon Correlation Spectroscopy (XPCS)

X-ray Photon Correlation Spectroscopy (XPCS) is a coherent X-ray scattering technique used to study nanoscale dynamics by means of observing time-dependent changes in the speckle pattern.

2.6.1 Literature review

The Photon Correlation Spectroscopy (PCS) method was first applied using optical light - so called Dynamic Light Scattering (DLS) or PCS with visible coherent light [79, 81]. In DLS one can study slow dynamics ($\omega < 10^6$ Hz) at resolutions of $q < 10^{-3}$ Å^{-1}. Extension of the PCS technique to the X-ray regime enables the analysis of dynamics on much smaller length scales. At state-of-the-art synchrotron facilities XPCS is typically used to probe the low frequency dynamics (10^{-3} Hz $< \omega < 10^6$ Hz) in a q range from 10^{-3} Å^{-1} up to several Å^{-1} [72, 82]. An additional advantage of XPCS over DLS is the ability to study opaque samples [83]. The frequency and wave vector range accessible by XPCS is shown in Fig. 2.9 in comparison to other techniques. At the currently available X-ray sources XPCS is ideally suited to probe slow nanoscale dynamics of matter at length scales unreachable by visible light techniques and time scales inaccessible by inelastic X-ray or neutron scattering techniques. Moreover newly commissioned or currently under construction DLSR (Diffraction-Limited Storage-Ring) [68] and XFELs (X-ray Free Electron Lasers) [68] will allow to perform

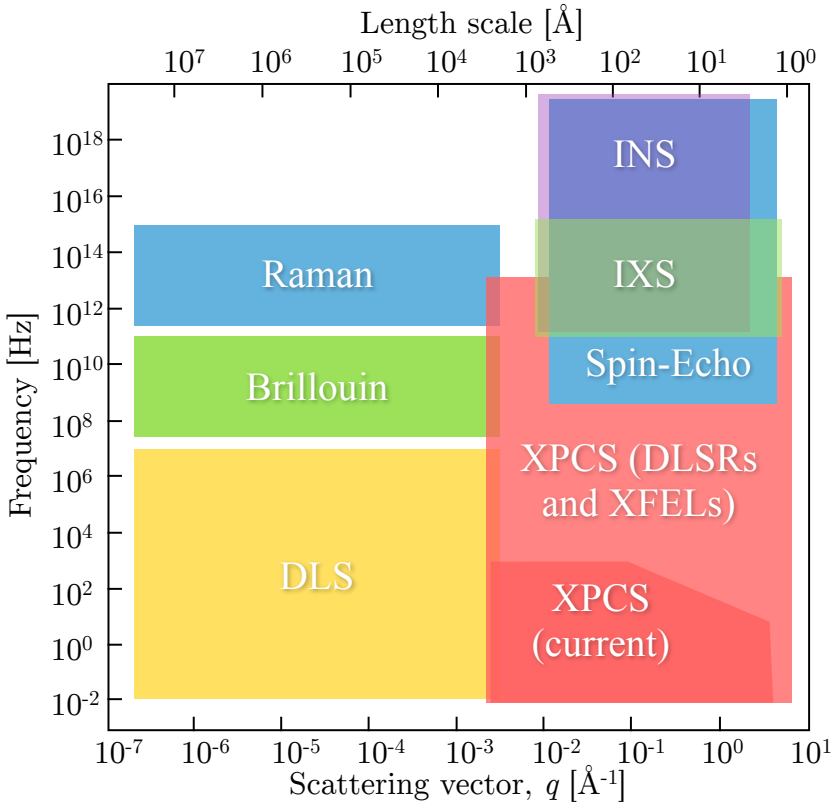

Figure 2.9: Schematic representation of the approximate frequency and wave vector ranges accessible by different techniques employing X-rays, neutrons and visible light. DLS - Dynamic Light Scattering; INS - Inelastic Neutron Scattering; IXS - Inelastic X-ray Scattering. Modified from [82, 84].

ultrafast XPCS studies (up to $\omega \sim 10^{13}$ Hz) providing a time-domain probe complementary to the inelastic scattering techniques.

First XPCS experiments were performed at ESRF (European Synchrotron Radiation Facility) [85, 86] and NSLS [83] in 1995. Brauer et al. studied the order-disorder transition in Fe_3Al alloys and observed the intensity fluctuations of speckle patterns above the critical temperature T_c [86]. Furthermore, XPCS allowed the determination of the diffusion coefficient for Brownian motion of optically opaque gold colloidal particles dispersed in glycerol [83].

Since that time XPCS has significantly contributed to understanding of nanoscale dynamics in numerous hard and soft condensed matter systems: colloidal glasses and gels [41, 83, 87–111], polymers [112–126], metals and alloys [86, 127–130] as well as metallic and molecular glasses [131–134], liquid crystals [135–137] and magnetic systems [84, 90, 138–140]. A variety of important dynamical phenomena in these systems have been studied with XPCS e.g.: phase-separation dynamics of colloid-polymer mixture [94], heterogeneous dynamics in colloidal and granular systems undergoing a jamming transition [100, 111], dynamics of capillary waves [141, 142] and surfaces fluctuation in polymer films [114, 115], ballistic atomic motion in metallic glasses [134]. The XPCS capabilities were expanded by use of two-time correlation functions [127, 128, 143] to study non-equilibrium dynamics. Combinations of XPCS with droplet algorithm [132] and event correlator [144] have been used to study dynamics at low scattering signals.

An exhaustive summary of XPCS research studies can be found in several reviews by G. Grübel [72], M. Sutton [145], R. L. Leheny [146], O. G. Shpyrko [84] and A. Nogales [126].

2.6.2 Intensity-Intensity Correlation Functions in the time domain

In XPCS experiments the information on sample dynamics is extracted from the fluctuating intensity by constructing its intensity-intensity correlation function

$$\langle I(\mathbf{q},t)I(\mathbf{q},t+\Delta t)\rangle = \lim_{T_0\to\infty}\frac{1}{T_0}\int_0^{T_0} I(\mathbf{q},t)I(\mathbf{q},t+\Delta t)\mathrm{d}t\ , \tag{2.39}$$

which compares the signal $I(\mathbf{q},t)$ with a time-delayed signal $I(\mathbf{q},t+\Delta t)$ for all starting times t and delay times Δt. In eq. (2.39) T_0 is a total time of measurement and, t and Δt satisfy that $0 < t, \Delta t < T_0$. Fig. 2.10 shows a typical behavior of the correlation function defined in eq. (2.39). At zero delay time it reduces to

$$\lim_{\Delta t\to 0}\langle I(\mathbf{q},t)I(\mathbf{q},t+\Delta t)\rangle = \langle I^2(\mathbf{q},t)\rangle\ . \tag{2.40}$$

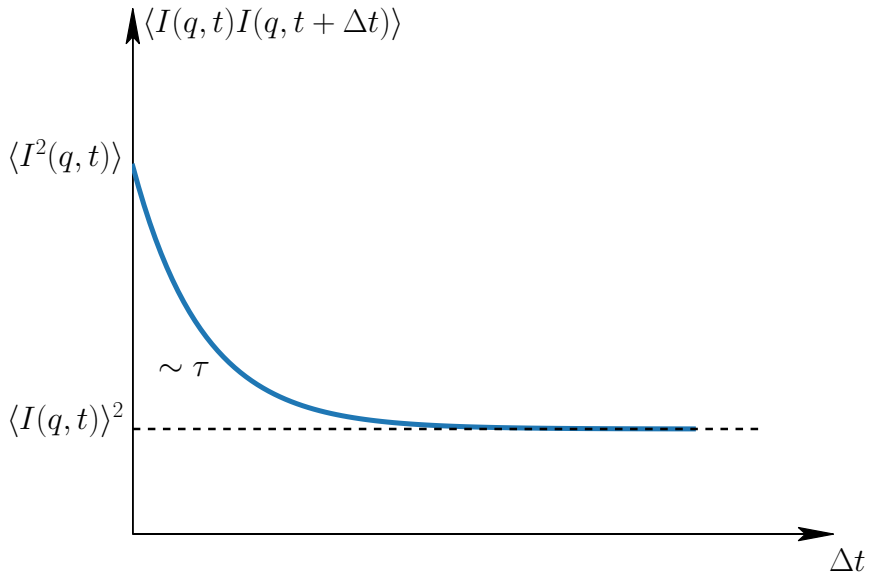

Figure 2.10: The time-dependent part of the correlation function decays with a time constant τ characterizing typical time of fluctuations in scattered intensity

For delay times much greater than the typical fluctuation time τ of the intensity, fluctuations in $I(\mathbf{q},t)$ and in $I(\mathbf{q},t+\Delta t)$ are uncorrelated and the average in eq. (2.39) can be split

$$\lim_{\Delta t\to\infty}\langle I(\mathbf{q},t)I(\mathbf{q},t+\Delta t)\rangle = \langle I(\mathbf{q},t)\rangle\langle I(\mathbf{q},t+\Delta t)\rangle = \langle I(\mathbf{q},t)\rangle^2 . \tag{2.41}$$

Thus, the intensity correlation function decays from the mean square intensity at small delay times to the square of the mean at long times.

A normalized form of the intensity correlation function is a second order correlation function of the electric-field amplitude

$$\begin{aligned} g^{(2)}(\mathbf{q},\Delta t) &= \frac{\langle I(\mathbf{q},t)I(\mathbf{q},t+\Delta t)\rangle_t}{\langle I(\mathbf{q},t)\rangle_t^2} \\ &= \frac{\langle E(\mathbf{q},t)E^*(\mathbf{q},t)E(\mathbf{q},t+\Delta t)E^*(\mathbf{q},t+\Delta t)\rangle}{\langle E(\mathbf{q},t)E^*(\mathbf{q},t)\rangle^2} . \end{aligned} \tag{2.42}$$

If the scattered intensity obeys Gaussian statistics the $g^{(2)}(\mathbf{q},t)$ function can be connected to the first order correlation function $g^{(1)}(\mathbf{q},t)$ via the Siegert relation [79]

$$g^{(2)}(\mathbf{q},\Delta t) = 1 + \left|\frac{\langle E(\mathbf{q},t)E^*(\mathbf{q},t+\Delta t)\rangle}{\langle E(\mathbf{q},t)E^*(\mathbf{q},t)\rangle}\right|^2 = 1 + |g^{(1)}(\mathbf{q},\Delta t)|^2 . \tag{2.43}$$

This connection is only true in case of a fully coherent source. Due to partial coherence

of the source in a typical XPCS experiment eq. (2.43) has to be slightly modified to

$$g^{(2)}(\mathbf{q}, \Delta t) = 1 + \beta |g^{(1)}(\mathbf{q}, \Delta t)|^2 \, . \tag{2.44}$$

The factor β is called the speckle contrast or Siegert/coherence factor [145]. The contrast relates to the complex degree of coherence and can be obtained experimentally e.g. by measuring speckle patterns from a static sample.

The autocorrelation function $g^{(1)}(\mathbf{q}, \Delta t)$ is also frequently called the normalized intermediate scattering function $f(\mathbf{q}, \Delta t)$ and can be expressed as

$$f(\mathbf{q}, \Delta t) = \frac{\tilde{S}(\mathbf{q}, \Delta t)}{S(\mathbf{q})} \, , \tag{2.45}$$

where $\tilde{S}(\mathbf{q})$ is the intermediate scattering function given for N identical particles by

$$\tilde{S}(\mathbf{q}, \Delta t) = \frac{1}{N} \sum_{i=1}^{N} \sum_{j=1}^{N} \langle e^{\mathbf{q}[\mathbf{r}_i(t) - \mathbf{r}_j(t+\Delta t)]} \rangle \, , \tag{2.46}$$

and $S(\mathbf{q})$ is the static structure factor defined in eq. (2.29).

2.6.3 Dynamical models

Consider the simple case of monodisperse particles undergoing Brownian motion [2]. In the absence of any interactions the static structure factor $S(\mathbf{q}) = 1$ and all cross terms ($i \neq j$) in eq. (2.46) average to zero. The mean square displacement of a free Brownian particle is [2]

$$\langle [\mathbf{r}_i(t) - \mathbf{r}_j(t + \Delta t)]^2 \rangle = 6 D_0 \Delta t \, , \tag{2.47}$$

where D_0 is the Stokes-Einstein diffusion coefficient of a particle with radius R in a medium with viscosity η given as

$$D_0 = \frac{k_B T}{6 \pi \eta R} \, . \tag{2.48}$$

The intermediate scattering function in eq. (2.45) reduces to a simple exponential decay

$$f(\mathbf{q}, \Delta t) = e^{-\Gamma \Delta t} \, , \tag{2.49}$$

with the relaxation rate $\Gamma = D_0 q^2$. The relaxation rate Γ is related to the relaxation time τ of the system as

$$\Gamma = \frac{1}{\tau} \, . \tag{2.50}$$

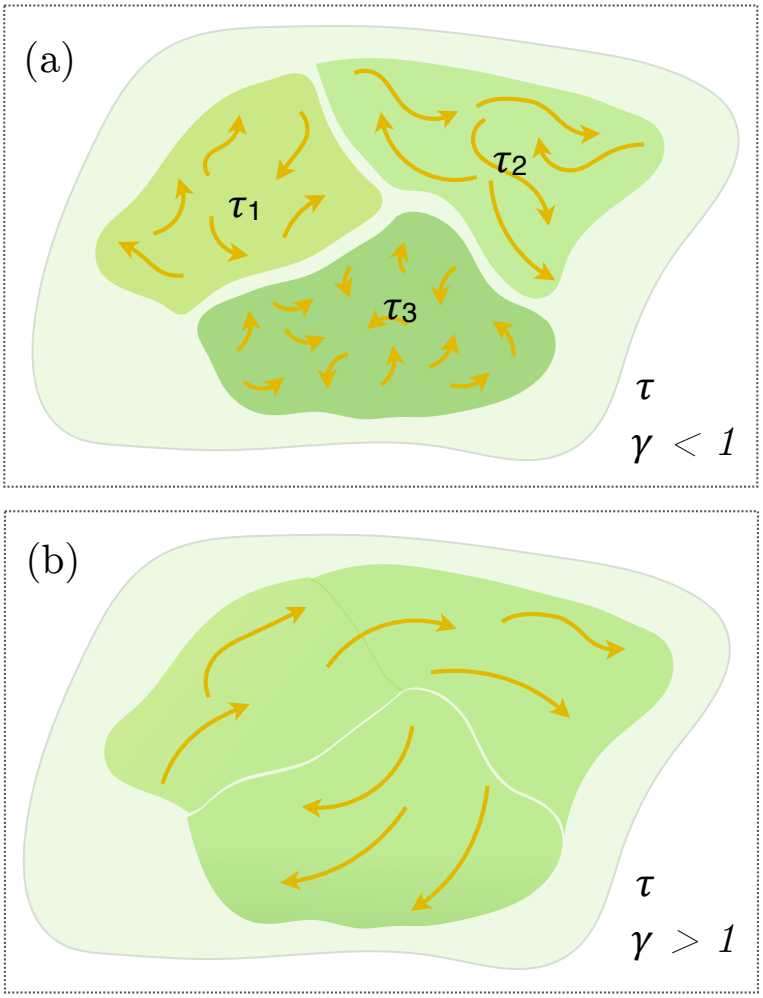

Figure 2.11: Schematic drawing of complex dynamical processes within the sample. (a) Schematic representation of the particle diffusion behavior in the case of $\gamma < 1$. Regions with different diffusion rates τ_i are represented by different colors. (b) Schematic representation of the particle diffusion behavior in the case of $\gamma > 1$. In (a) and (b) τ is the relaxation time of the whole system.

Substituting eq. (2.49) and eq. (2.50) in eq. (2.44) the second order correlation function takes the form

$$g^{(2)}(\mathbf{q}, \Delta t) = 1 + \beta e^{-2\Delta t/\tau} \, . \tag{2.51}$$

In the case of interacting particles the free diffusion coefficient D_0 has to be replaced by the effective short-time diffusion coefficient $D(\mathbf{q})$ [147]. This dynamical model has been employed in numerous XPCS works [88, 114, 129, 135] .

Consider the case of multiple dynamical processes with similar decay rates observed at the same time in different regions within the sample. Such dynamical behavior is typical for a majority of systems (e.g. supercooled and glassy soft matter systems). The model can be corrected for the effect of inhomogeneity by introduction of the stretching exponential parameter γ common for the whole sample. The intensity

autocorrelation function takes the form

$$g^{(2)}(\mathbf{q},t) = 1 + \beta e^{-2(\Delta t/\tau)^{\gamma}} \ . \tag{2.52}$$

Eq. (2.52) is also known as Kohlrausch-Wiliams-Watts (KWW) model where the stretching parameter γ is called KWW parameter. In this model τ characterizes the dynamics of the whole system.

For colloidal systems the case of $\gamma < 1$ (stretched exponential function) usually describes the sub-diffusive motion of the particles [91, 94, 123, 125]. The sub-diffusive motion of particles is schematically shown in Fig. 2.11 (a). In each region the dynamics can be described by a single exponential decay but with different relaxation times τ_i. The stretched behavior arises from the ensemble averaging [148].

Values of $\gamma > 1$ (compressed exponential function) indicate non-equilibrium dynamics [94, 97, 125, 131, 133, 135]. In this case there are regions within the sample with spatially cooperative motion of particles (Fig. 2.11 (b)).

For example the evolution of correlation functions from the stretched exponential form ($\gamma < 1$) to a compressed decay ($\gamma > 1$) mode have been observed in metallic glasses when the system transitioned from the supercooled state to the glass state [133, 134]. The temperature dependence of the stretching exponential parameter γ was also investigated on the sterically stabilized Si spherical nanoparticles dispersed in propanediol mixture [97] and in polypropylene glycol solvent [125].

In the frame of this work we limit ourselves to the KWW model. However, a great variety of dynamical models are used to describe the XPCS experiments, e.g. capillary waves [141], XPCS under flow [101] and others.

2.7 X-ray Cross Correlation Analysis (XCCA)

X-ray Cross Correlation Analysis (XCCA) is a coherent scattering technique that allows to investigate the structure of individual particles and structural properties of disordered and partially ordered systems such as alloys or colloidal glasses. In this approach the scattered intensities $I(\mathbf{q},t)$ at different scattering vectors $\mathbf{q}$ are correlated at the same or different times $t_1,\ t_2$ as

$$C(\mathbf{q}_1,\mathbf{q}_2,t_1,t_2) \sim I(\mathbf{q}_1,t_1)I(\mathbf{q}_2,t_2), \tag{2.53}$$

where $C(\mathbf{q}_1,\mathbf{q}_2,t_1,t_2)$ is called an intensity cross correlation function (CCF). Its detailed properties will be described in section 2.7.2.

2.7.1 Literature review

The idea of cross correlation analysis was originally proposed by Kam in 1977 as the means to determine the structure of individual macromolecules in solution [73]. The scattered intensity from identical, non-oriented particles is recorded with time resolution shorter than the time required for particles to reorient themselves. An analysis of angular variations in the scattered intensity using CCF in addition to the radial variations as in conventional SAXS analysis makes it possible to recover information about the particle structure. The idea behind the method was verified by results obtained in light scattering studies [149–151] and electron microscopy [152–154]. Clark [149] extended Kam's approach to study the local order in condensed phases. There, a 2D system, a single liquid layer of polystyrene spheres of about 230 nm in size, was investigated in a visible light scattering experiment. The obtained two-point CCFs displayed pronounced modulations corresponding to sixfold symmetry that were associated with 2D hexagonal close packed structure of particles. Evidence for higher-order spatial correlation of particles was found in cross correlation functions observed in a similar experiment on 3D colloidal liquid [150]. Clark et al. [149, 150] pointed out that intensity correlations in light scattering experiments are observed due to the small scattering volume, on the order of the correlation length in the liquid.

The progress of X-ray source technology (leading to e.g. a high degree of coherence[4] [155, 156]) and in instrumentation (e.g. detectors, lenses) makes it possible to apply the cross correlation approach in X-ray scattering experiments. Wöchner et al. demonstrated that hidden symmetries in a colloidal glass of polymethylmethacrylate (PMMA) spheres can be observed by XCCA [74]. This work revived interest in further theoretical and experimental XCCA studies. A number of theoretical and experimental XCCA studies were published during the last decade. A theoretical treatment of CCF data supported by computer simulations on 2D (dilute and dense) and 3D model systems is given in several works [155, 157–167]. XCCA studies can be divided in two main subfields: single particle structure determination [73, 157, 158, 162, 167–181] and studies of structural properties of disordered systems [66, 74, 149, 150, 163, 166, 182–198].

The XCCA method was adapted to the Single Particle Imaging (SPI) experiments that are now being realized at state-of-the-art storage ring sources and Free Electron Laser (FEL) facilities [199]. FELs with ultra-bright and ultra-short (femtosecond duration) X-ray pulses provide snapshots of randomly oriented particles unchanged during the pulse propagation. Two main approaches to the structure determination of individual particles based on the use of CCFs were developed. In the

[4] In [155] the role of coherence for XCCA is discussed.

first approach the results from CCFs are used as support for iterative phase retrieval algorithm [158, 162, 168, 170, 172, 173, 179]. The second approach is based on directly fitting the real-space structure to measured X-ray data using CCFs as constraints [174,175,177,180]. The structure determination through the use of spatial correlations of X-ray diffraction patterns measured at LCLS (Linac Coherent Light Source) from single polystyrene dimers was demonstrated in [172]. In X-ray scattering experiment performed at SLS (Swiss Light Source) Pedrini et al. applied a similar approach to 2D systems and recovered the structure of three-fold gold nanoparticles [173].

In disordered systems, XCCA has been applied to investigate the local order in colloidal 2D and 3D systems [149, 150, 186, 193, 195, 198, 200], to quantify the bond orientational order in liquid crystals [183,189,196], investigate the structure of a nanocrystal superlattice [197], to reveal structural inhomogeneities in polymers [184, 185, 188], and to study local order of magnetic domains [201–203].

Cross correlation studies on colloidal systems are especially important for this work. The first light scattering correlation studies on 2D and 3D colloidal systems have already been mentioned above [149–151]. A recent cross correlation analysis study in ultra-small angle light scattering experiment on 2D colloidal films has also been performed [186]. CCFs quantitatively describe the degree of hexagonal ordering in 2D films when differently sized microspheres are mixed. The results of cross correlation analysis were in good agreement with the results of spatial correlation analysis performed on scattering patterns obtained from microscopy images of 2D films. In recent years, the application of cross-correlation analysis to X-ray studies on colloidal systems attracted a lot of interest [74]. Microscopy and cross correlation techniques were combined in the X-ray region to extend a spatial correlation approach to nanometer length scales [66]. XCCA revealed regions of different predominant sizes of colloidal nanospheres in dried multilayer colloidal films and various degrees of orientational order of particles in them. Theoretical investigations of XCCA allowed the development of an approach to study dense colloidal systems such as colloidal glasses [166]. The combination of SAXS and XCCA studies on suspensions of colloidal crystallites in water at high pressures revealed a pressure-dependent increase in the orientational order of the crystallites [193]. XCCA performed on 3D colloidal suspensions of hard sphere crystallites revealed the face centered cubic structure of the system through correlation of intensities at different Bragg peak positions [190]. In 3D colloidal hard sphere systems at supercooled conditions XCCA technique allowed the observation of the local orientational order and indications for crystalline precursor structures [67].

2.7.2 Intensity-Intensity Correlation Functions in the space domain.

The form of the cross correlation function (CCF) can be chosen differently depending of the purpose and measured parameters of the XCCA experiment. Here, in order to investigate of local order in colloidal dispersions, the cross correlation function is introduced in its most common form following [74] through angular correlations of scattered intensity in reciprocal space with a constant modulus of wave vector transfer q ($|\mathbf{q}_1| = |\mathbf{q}_2| = q$)

$$C(q, \Delta\varphi) = \frac{\langle I(q,\varphi) I(q,\varphi+\Delta\varphi)\rangle_\varphi - \langle I(q,\varphi)\rangle_\varphi^2}{\langle I(q,\varphi)\rangle_\varphi^2} \,. \tag{2.54}$$

The correlations of intensities are performed at the same time value $t_1 = t_2$. The momentum transfer vector $\mathbf{q}$ lies in the plane normal to the incident beam and is expressed in the polar coordinates as $\mathbf{q} \equiv (q, \varphi)$. In eq. (2.54) $\Delta\varphi$ is an angular difference between momentum transfers $\mathbf{q}_1$ and $\mathbf{q}_2$, and it varies from 0 to 2π. $\langle\rangle_\varphi$ denotes the average over the angle φ. The instructional guide to the construction of $C(q, \Delta\varphi)$ is given in Fig. 2.12. An expansion of correlation function $C(q, \Delta\varphi)$ into a Fourier series with respect to $\Delta\varphi$ allows detailed study of the function's symmetry properties [159–161, 165, 204]. The Fourier expansion is defined as

$$C(q, \Delta\varphi) = \sum_{l=-\infty}^{\infty} C_l(q) e^{il\Delta\varphi} \tag{2.55}$$

where the Fourier coefficients

$$C_l(q) = \frac{1}{2\pi} \int_0^{2\pi} C(q, \Delta\varphi) e^{-il\Delta\varphi} \mathrm{d}\Delta\varphi \tag{2.56}$$

allow study of the local orientational order of the sample. The connection between the Fourier coefficients $C_l(q)$ and structural orientational order is demonstrated on a simple example of a 2D system (see Fig. 2.13). The system contains 5 randomly oriented hexagonal clusters of spherical particles (Fig. 2.13 (a)). A simulated scattering pattern [159, 161, 166] from this system is shown in Fig. 2.13 (b). The Fourier coefficients $C_l(q)$ of the function $C(q, \Delta\varphi)$ obtained from simulated scattering pattern are shown as a function of the l-component in Fig. 2.13 (c). It is clearly visible that the Fourier coefficients with $l = 6, 12$ are dominating, reflecting the 6-fold symmetry of the real structure of the system. Several simulation works on 2D and 3D systems with more complexity have been performed in order to advance the understanding of the XCCA approach [155, 159–161, 164–166, 204].

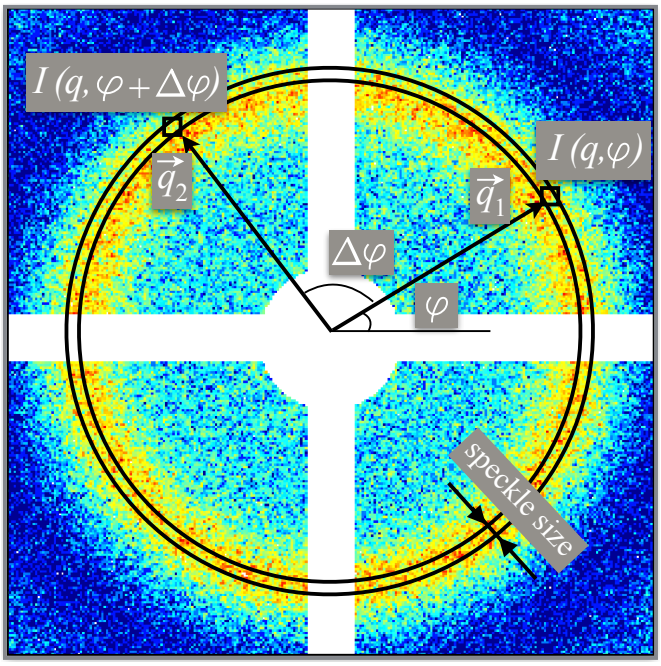

Figure 2.12: Parameter definitions for the angular cross correlation function $C(q, \Delta\varphi)$ in XCCA.

Fourier coefficients $C_l(q)$ can be connected to Fourier coefficients of the normalized intensity fluctuation $\tilde{I}(r, \varphi)$, introduced as

$$\tilde{I}(q, \varphi) = \frac{I(q, \varphi) - \langle I(q, \varphi) \rangle_\varphi}{\langle I(q, \varphi) \rangle_\varphi}. \tag{2.57}$$

Substituting eq. (2.54) in eq. (2.56) (see Appendix B) the following expression is obtained

$$C_l(q) = |\tilde{I}_l(q)|^2 \,, \tag{2.58}$$

where $\tilde{I}_l(q)$ is the angular Fourier coefficient in the Fourier decomposition of normalized intensity fluctuation $\tilde{I}(q, \varphi)$. Usually in XCCA investigations of local order in simulation models or in real 2D and 3D colloidal systems the ensemble average over many realizations of the speckle pattern is performed in order to achieve sufficient statistics for Fourier coefficient $C_l(q)$.

Moreover, in [166, 190] the function

$$\Psi_l(q) = \langle \tilde{I}_l^2(q) \rangle_e - \langle \tilde{I}_l(q) \rangle_e^2 \tag{2.59}$$

was introduced which is the variance of the Fourier coefficients $\tilde{I}_l(q)$. This function is more sensitive to the orientational order in the system [166]. The $\langle \rangle_e$ denotes the ensemble average.

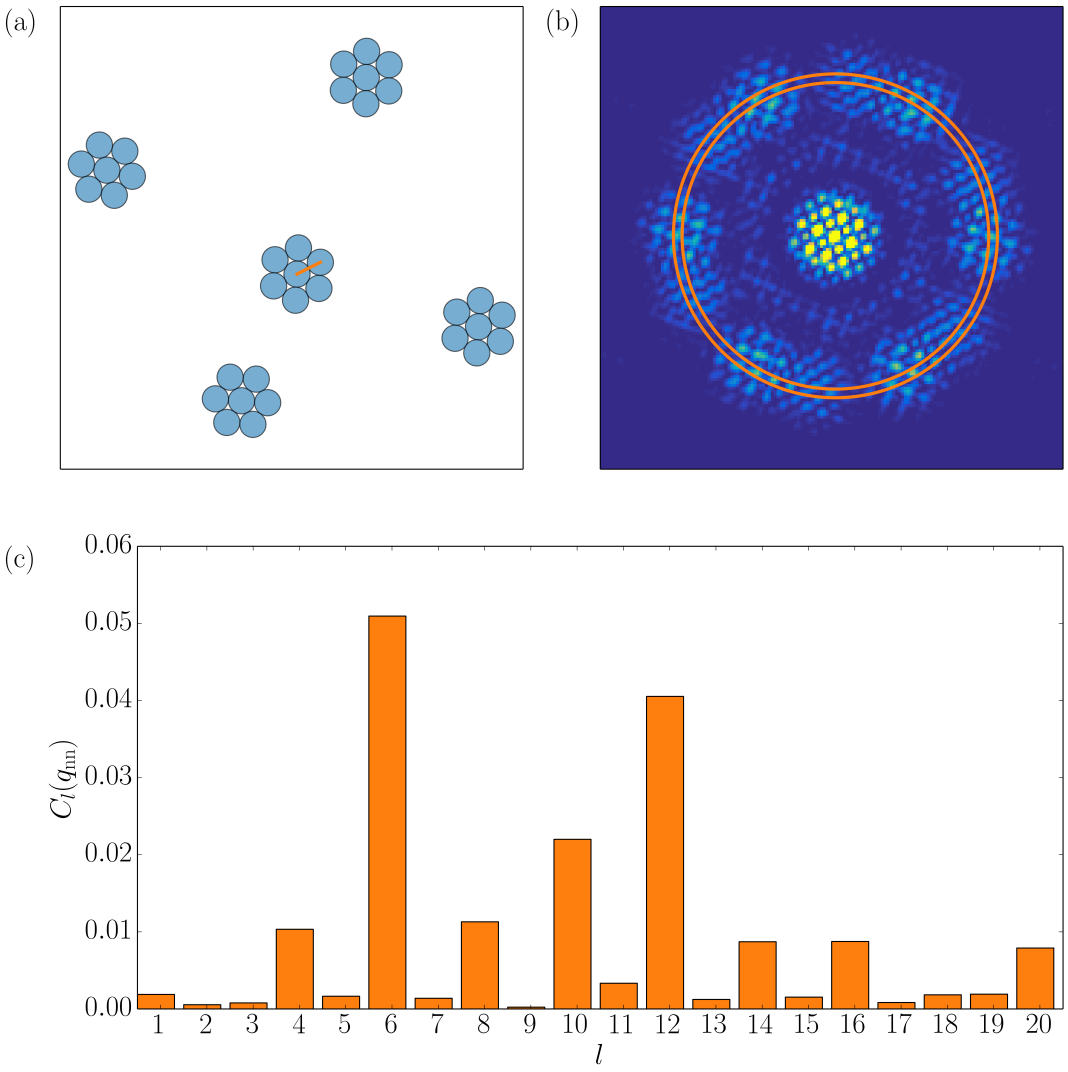

Figure 2.13: (a) XCCA on a model system of 5 randomly oriented hexagonal clusters of spherical particles. (b) Simulated scattering intensity pattern from the structure shown in (a). (c) The Fourier coefficients $C_l(q_{\rm nn})$ as a function of l-component calculated at the momentum transfer $q_{\rm nn} = 2\pi/r_{\rm nn}$ shown in (b). The next-neighbor distance $r_{\rm nn}$ is shown in (a) by the orange line.

CHAPTER 3

EXPERIMENTAL PART

3.1 Sample preparation

In the framework of this thesis charge stabilized polymethacrylate (PA) nanoparticles were synthesized by means of the free radical emulsion polymerization method. The theoretical aspects of the method are described in the section 3.1.1. The synthesis procedure of PA nanoparticles is described in section 3.1.2.

3.1.1 Free radical emulsion polymerization method

Free radical emulsion polymerization is a standard method for the preparation of polymeric colloids. The polymerization mechanism was originally described in the works of Smith and Ewart [205] and Harkins [206]. The main components of the polymerization reaction are the monomer(s), the dispersing medium (usually water), the surfactant (not always used), and the initiator. Fig. 3.1 schematically shows the polymerization process that can be divided in three intervals: the initiation, the propagation and the termination [205].

In the first interval the particle nucleation takes place. First initiating radicals are formed by dissociation of initiator molecules. The initiating radicals attach monomers dispersed in medium and thereby the small chains of oligomer radicals grow. These small oligomer radicals are hydrophilic and continue to grow into bigger oligomer chains which still have a radical center on one end of the growing chain. There are two different nucleation mechanisms of the precursor particles: either via micelles formation by oligomer chains [207], or the formation of a precursor particle from oligomer radicals after they reach a critical molecular weight (or critical length z_{crit}) [208]. In the first nucleation mechanism the growing micelle turns into a small polymer sphere, while in the second several oligomer precursor particles combine to a mature particle. In the first interval of the synthesis the number of precursor particles increases and then remains constant during the next intervals.

In the second interval, newly formed oligomers have a higher probability to attach to the existing polymer particles rather than to form a new one. If the surfactants are also present in the solvent they will be absorbed on the particle surface. While the polymer particles increase in size, the amount of monomers decreases. When the radicals and monomers are exhausted in the dispersing medium, the third interval starts in which the polymerization proceeds only within the particles until the reaction finally stops.

Colloidal particles synthesized by radical emulsion polymerization usually have spherical form. The particle size can be obtained in the range from 50 up to 300 nm in diameter at will [210]. Different mechanisms of the particle stabilization are possible

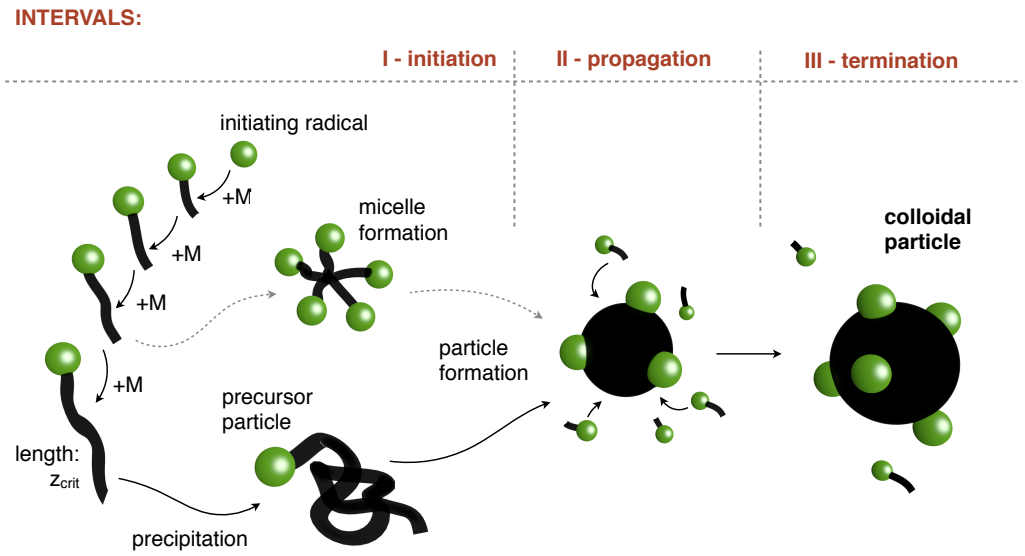

Figure 3.1: Schematic representation of the radical emulsion polymerization reaction divided into three intervals: the initiation, the propagation and the termination. M stands for monomer, z_{crit} for the critical chain length of the formed oligomers. The dashed and solid arrows show two ways of particle formation: via the micelle formation or by propagation and coagulation of oligomers with critical length z_{crit}. (modified from [209]).

such as steric or electrostatic (see section 1.3).

3.1.2 Polymethacrylate nanoparticles synthesis

Polymethacrylate nanoparticles (PA) were chosen as the sample system. These particles contain fluorine and silicon groups that enhance the scattering properties of this system.

Chemical reagents

The following chemical reagents are used for the synthesis procedure and preparation of the PA samples:

- monomers: 1H,1H,5H-Octafluoropentylmethacrylate (M1), Methacryloxymethyltrimethylsilan (M2), 2,2,3,3,4,4,5,5-octafluorohexanediol-1,6-dimethacrylate (M3), ABCR GmbH & Co. KG, Germany
- redox system: $NaSO_3$ and $(NH_4)_2Fe(SO_4)_2$, Fluka, Switzerland
- initiator: $K_2S_2O_8$, Merck, Germany
- salt: KCl, Merck, Germany.

Synthesis procedure

The synthesis was performed in a round bottom three necked flask (2.5 L) supplied with a reflux condenser and a nitrogen inlet tube. The reaction temperature of 57 °C was kept constant during the whole synthesis process by immersing the reaction vessel in an oil bath. First to remove the oxygen the deionized water (1.5 L) in the flask was saturated by nitrogen flowing through the solution. Then the redox system was added. The solution was stirred at a speed of about 700 rpm (rpm = revolutions per minute). After 10 min functionalized monomers (M1, M2) were added to the solution. The addition of cross-linker monomers (M3) to the mixture allowed the cross-linking of the propagating chains to stabilize the formed nanoparticles. The reaction was initiated by adding potassium peroxydisulfate ($K_2S_2O_8$). The reaction vessel was continuously stirred and kept under nitrogen atmosphere during the following 24 h. The dispersion turned milky white during the polymerization process. The resulting particles are negatively charged macroions due to the adsorption of sulfate groups (from the initiator) on the particle surface. The dissociated counter ions in the dispersion medium form an ionic cloud around the particle, resulting in an electrical double layer (see electrostatic stabilization in section 1.3).

After the synthesis was finished the remaining products of the synthesis (monomers, low weighted oligomers) were removed by dialysis against distilled water for one week. Afterwards, in order to increase the colloidal particle's concentration the solvent was partially removed under a reduced pressure at 40°C using a rotary evaporator. Concentration was further increased in a centrifugation procedure. The dispersion was gently centrifugated and the excess solvent was removed by decanting the upper solvent. Several repetitions were performed until the desired concentration was reached. Three stock samples were obtained with 40.6 (A), 33.3 (B) and 19.6 (C) wt.% concentration, respectively.

For the experiments, two sample series were prepared. The first series consisted of samples with different volume fractions which varied in the range $0.6 \leq \phi \leq 0.34$. The desired volume fraction was achieved via dilution of the samples A, B, C with deionized water. The volume fractions were calculated using the density values of a PA particle (1.3 g/cm^3 [211]) and the solvent (water, 1 g/cm^3). The second series were prepared by adding small volumes of differently concentrated dissolved potassium chloride (KCl) in deionized water. The concentration of salt was varied from 10 μM to 1 mM, while the volume fraction of samples was kept constant at $\phi = 0.27$. The characteristics of the individual samples are summarized in Table 3.1 and Table 3.2. According to the phase diagram for charge stabilized particles (see Fig. 1.4) samples PA-1, PA-2, PA-3 can be considered as glasses (see Table 3.1). PA-4 sample lies on the glassy-to crystal transition border, sample PA-5 is a coexistence of fcc (face-centered-

cubic) and bcc (body-centered-cubic) structure, and samples PA-6 and PA-7 have a pure bcc structure. PA-8 lies on a crystal-liquid phase transition border. Three samples with salt: PA-2a, PA-2b, and PA-2c are in the glass state (see Table 3.2). Higher salt concentration suggests that the sample PA-2d exists as an fcc structure, and further addition of salt suggests a liquid phase of sample PA-2e.

Strongly diluted sample of $\phi \sim 0.001$ with additional salt amount (333 μM) was also prepared for form factor measurements. All samples before the experiment were filled into quartz capillaries with 0.7 mm thickness. The capillaries were sealed with glue on top.

Pre-characterization of the particle size was done via DLS (Dynamic Light Scattering) [79]. It resulted in a particle radius estimate of about 120 ± 10 nm.

Table 3.1: Dilution factor of the stock sample and volume fractions ϕ for the first sample series

sample	diluted stock sample	volume fraction, ϕ	phase state
PA-1	A (99:100)	0.34	glass
PA-2	B (99:100)	0.27	glass
PA-3	B (90:100)	0.25	glass
PA-4	B (70:100)	0.19	glass or fcc + bcc
PA-5	C (99:100)	0.16	fcc + bcc
PA-6	C (80:100)	0.13	bcc
PA-7	C (55:100)	0.09	bcc
PA-8	C (40:100)	0.06	bcc or liquid

Table 3.2: Salt concentration for the second sample series. For a dilution factor of the stock sample and volume fraction ϕ see parameters of the sample PA-2 in Table 3.1

sample	Salt [μM]	phase state
PA-2a	10	glass
PA-2b	50	glass
PA-2c	100	glass
PA-2d	500	fcc
PA-2e	1000	fcc or liquid

3.2 Experimental details

3.2.1 Experimental setup

The experiment was performed at the coherent scattering beamline ID10 of the European Synchrotron Radiation Facility (ESRF) in Grenoble. A schematic overview with basic components of the beamline set-up is given in Fig. 3.2.

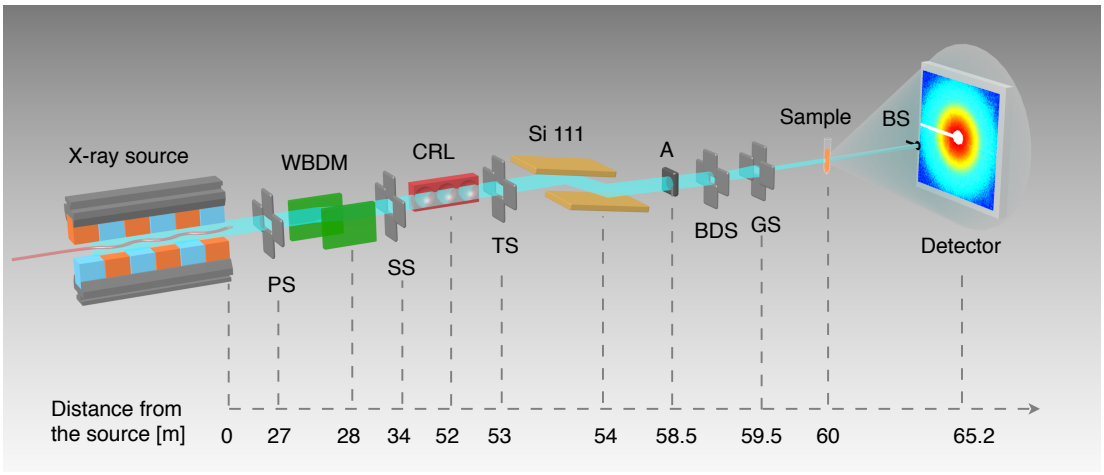

Figure 3.2: Sketch of the beamline ID10. PS - primary slits, WBDM - white beam double mirror, SS - secondary slits, CRL - compound refractive lenses, TS - ternary slits, A - attenuator, BDS - beam-defining slits, GS - guard slits, BS - beamstop.

The X-ray beam is generated by a set of three undulators [212] and passes through a system of primary slits (PS). The X-ray source parameters were optimized for a photon energy around 8 keV. The source size and the divergence of the photon beam are given in Table 3.3.

Table 3.3: Source size (FWHM[1]) and divergence (FWHM) of the photon beam from the undulator at beamline ID10.

Source parameter	Horizontal	Vertical
Size [μm]	928	23
Divergence [μrad]	28	17

In order to suppress high harmonics generated by the undulator a white beam double mirror system (WBDM) is used. It is placed at 28 m from the source and reflects the X-ray beam in the horizontal plane.

[1] full width at half maximum

Further downstream the X-ray beam passes through a system of secondary slits (SS), focusing system and ternary slits (TS). The beam focusing is provided by a beryllium compound refractive lens (CRL) placed at 52 m from the source. After focusing the X-ray beam is monochomatized by a water-cooled pseudo channel-cut Si(111) monochromator diffracting in vertical geometry and placed at 54 m from the source. The monochromator is made from a polished crystal cut into two plane Si (111) crystals that are mounted on an invar holder to act similar to a real channel-cut monochromator [213]. The photon energy selected by the monochromator was 8.1 keV corresponding to a wavelength of $\lambda = 1.53$ Å. The bandwidth obtained with the monochromator is $\delta\lambda/\lambda \simeq 1.4 \times 10^{-4}$.

The beam is guided to the sample position (60 m from the source) through the segmented vacuum flight-path tube with a Si_3N_4 exit window of 500 nm thickness. The final X-ray beam size is defined by a set of beam-defining roller-blade slits (BDS) with a 10×10 μm^2 opening placed 500 mm upstream the sample. The radiation diffracted from the BDS was blocked by the Si blade guard slits (GS). By taking into account that the storage ring was operated in a 16-bunch filling mode with a maximum ring current of 90 mA, the photon flux can be estimated as 4×10^{10} photons s^{-1}.

In case one needs to decrease the beam intensity (e.g. to limit radiation induced damage) an attenuator consisting of thin metal foils can be inserted at 58.5 m from the source.

The quartz capillary of 0.7 mm in diameter is filled with the sample and mounted in a SAXS chamber [214] that is installed onto a 4-circle diffractometer. The entrance window of the SAXS chamber is a Mica-window with 10 μm thickness. It is located 4 cm upstream of the sample.

The X-rays scattered by the sample propagate to the detector through a vacuum flightpath. The flightpath's exit window is Kapton foil of 75 μm thickness. A round tantalum beam-stop[2] blocking the direct beam is glued on the exit window of the flight tube in front of the detector. The scattering patterns are measured by a two-dimensional photon-counting pixel detector Maxipix 2×2 placed in the far-field at 5.2 m from the sample. The detector has a matrix area of 516×516 pixels with a pixel size of 55×55 μm^2 and can be operated in a 300 Hz full frame rate.

Beamline characteristics are used further to estimate additional parameters important for experiment interpretation.

[2]Beam-stop diameter is about 2 mm

Speckle size

The speckle size is given by

$$\sigma = \frac{\lambda d}{a} \,, \tag{3.1}$$

where λ is the wavelength, d is the sample-to-detector distance, and a is the size of the illuminated area. In our case the speckle size was estimated to be about 80 μm. Note that the pixel size of the Maxipix detector is comparable to the speckle size allowing the detection of the intensity fluctuations of the speckles.

Longitudinal coherence length

The longitudinal coherence length $\xi_l \simeq 1\mu$m is estimated via eq. (2.37).

Transverse coherence length

The estimates for the horizontal and vertical transverse coherence lengths can be obtained via eq. (2.36). The distance from the source to the sample is 60 m. The source size can be found in Table 3.3. For a photon energy of 8.1 keV ($\lambda = 1.53$ Å) eq. (2.36) yields 5 μm and 200 μm of coherence length in horizontal and vertical directions, respectively.

3.2.2 Data collection procedure

In order to study the sample dynamics XPCS measurements were performed. The averaged and local structural properties of the sample were investigated by performing XCCA measurements. In order to estimate the scattering background the scattering patterns of the empty capillaries and pure solvents were also recorded.

XPCS procedure

An XPCS run consists of a series of scattering patterns successively recorded in time from one sample position. The main XPCS parameters are listed below.

- **The number of recorded scattering patterns** varied from 200 and 1000.
- **The exposure time** was usually set to 3 ms. In some cases the exposure time was set to 10 ms.
- **The delay time between scattering patterns** was dependent on estimated sample dynamics. The delay time was varied from 0 to 5 s and stayed the same during each XPCS run. Introduction of such a delay also helps to prevent sample beam damage. Depending on the delay time the XPCS run was operated in

different regimes: continuous or frame modes. In "continuous mode" the delay is 0 and the beam shutter stayed open during the whole run. However, in addition to the read-out time there is a 6 μs dead read out time of the detector that has to be accounted for in the data analysis as a delay between scattering patterns. In the "frame mode" when the delay time is different from 0 the shutter is closed during the delay time and opened during the exposure time.

For most of the XPCS runs the incoming intensity of the beam was reduced by a factor of 10 by insertion of the attenuator ensuring a coherent flux of 4×10^9 photons s^{-1}.

XCCA procedure

In the XCCA measurements the sample was probed at 1000 - 2000 different spots. Typically an XCCA run involved 20×100 probe positions (H$\times$V) with horizontal and vertical steps of 20 μm and 30 μm, respectively, to avoid beam overlap. The scanned sample area was therefore 400×3000 μm^2 (H$\times$V). In order to obtain sufficient statistical information at each position 20 scattering patterns were recorded without delay time between the frames. The beam was not attenuated and the exposure time was set to 3 ms . The limited number of scattering patterns and the shortest possible exposure time are necessary to limit the radiation induced damage. Scanning was always performed in the top-to-bottom direction. This direction was chosen to avoid the disturbance of the not-yet-scanned area with perturbations caused by X-ray exposure (e.g. bubbles).

CHAPTER 4

EXPERIMENTAL RESULTS AND DISCUSSIONS

4.1 Form factor analysis

Information about the shape, the size and the size distribution of the colloidal particles can be obtained by performing a SAXS measurement on dilute non-interacting samples. In this case the scattered intensity is proportional to the particle form factor (see section 2.4.1).

The particle form factor of the PA system was measured from a dilute particle dispersion at a volume fraction of $\phi \sim 0.001$ where the direct particle interactions were electrostatically screened by the addition of KCl electrolyte solution leading to a salt concentration of 333 μM. The measurements were performed at beamline ID10 at the ESRF (see section 3.2). The recorded scattering intensity patterns (500 patterns with exposure time 0.03 s per pattern) were averaged to one 2D pattern and corrected for the scattering of X-rays from a water-filled capillary. Fig. 4.1 shows the form factor intensity profile $I(q)$ obtained from the corrected 2D pattern by azimuthal averaging at constant q. The intensity of the averaged signal falls off with increasing q and shows an oscillating behavior indicating sufficiently monodisperse particles (see section 2.4.1).

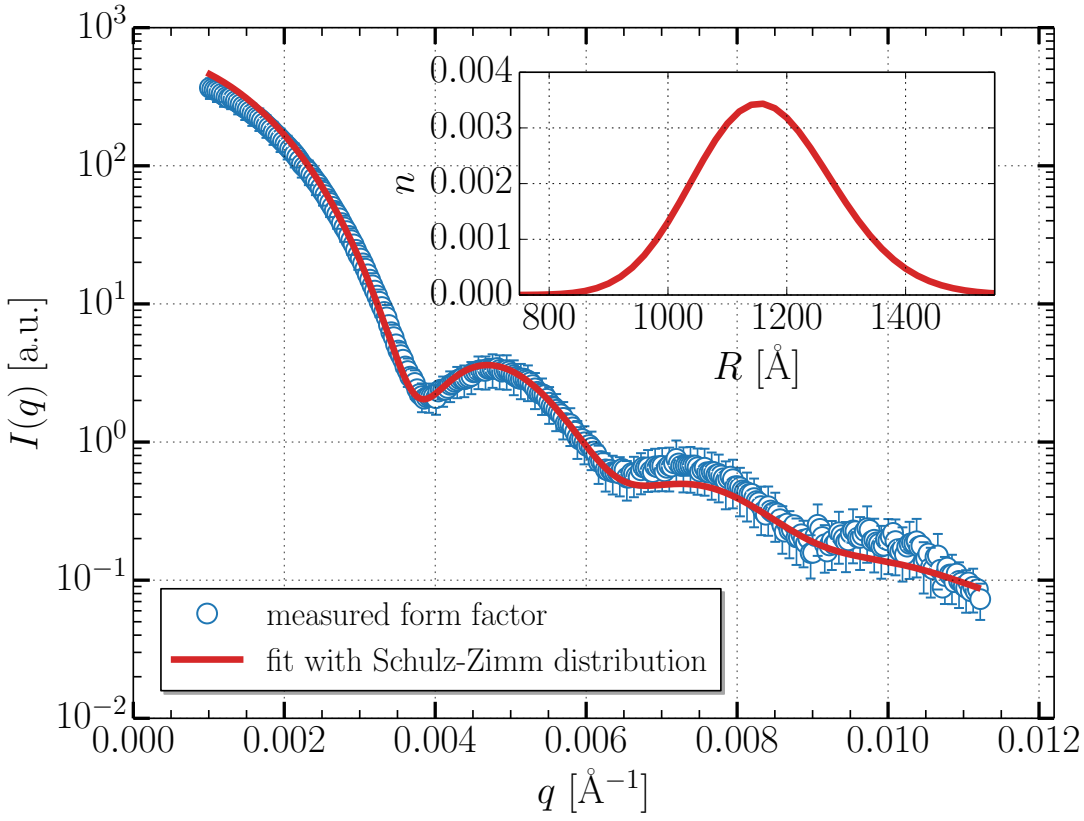

Figure 4.1: Scattered intensity profile of the dilute PA sample as a function of the momentum transfer q. The solid red line is a fit of eq. (4.1) to the data. The inset is the particle size distribution obtained by the Schulz-Zimm function (see eq. (2.26)).

The experimental data were fitted with an extended polydisperse sphere model:

$$I(q) = BG + I_0 \int_0^\infty n(R, R_0, Z) P_{sph}(q, R) \mathrm{d}R, \tag{4.1}$$

where BG is the background signal from solvent and the capillary, I_0 is an intensity scaling factor, $P_{\text{sph}}(q, R)$ is the intensity form factor of spherical particles (see eq. (2.23)) and $n(R, R_0, Z)$ is the Schulz-Zimm size distribution function (see eq. (2.26)). The fit was performed within the q-region of 0.002 Å$^{-1} < q < 0.01$ Å^{-1} and yielded an averaged particle radius $R_0 = 1165$ Å and a size polydispersity $\Delta R/R_0 = 10\%$. The fit and the particle size distribution are shown in Fig. 4.1.

4.2 Structure factors

The static behavior changes dramatically in the case of interacting particles. The scattered intensity $I(q)$ contains information on both particle shape and size described by the form factor $P(q)$ and the inter-particle correlations described by the structure factor $S(q)$.

Fig. 4.2 shows the intensity profiles as a function of momentum transfer q for samples at different volume fractions. Intensity profiles are scaled for easier comparison. The intensity profiles $I(q)$ for the samples with $\phi \geq 0.13$ were obtained by azimuthal averaging of 2000 scattering patterns taken at different spots on the sample. These measurements provide sufficient statistics for data analysis, which is especially important for higher momentum transfer q. The data analysis for samples with volume fractions $\phi < 0.13$ was performed on 200 scattering patterns measured at one sample spot. All intensity curves were corrected for the scattering of X-rays from a water-filled capillary.

The scattering at large q values ($q > 0.006$ Å^{-1}) is mostly defined by the form factor $P(q)$ (solid line). The intensity falls off as q^{-4}. Such a slope is expected for spherical particles in the Porod regime [50]. The deviation from the slope for samples with $\phi < 0.13$ at higher q values ($q > 0.008$ Å^{-1}) is due to a smaller number of scattering patterns in combination with background scattering signal, which dominates the signal from particles at these volume fractions. Therefore the structure factor analysis for these samples was performed for a limited q-range ($q < 0.008$ Å^{-1}, dashed line b in Fig. 4.2).

The intensity profiles show a pronounced peak at low q values ($q < 0.004$ Å^{-1}). The amplitude of the peak increases with increasing volume fraction ϕ. Changes of shape of the second intensity peak (0.004 Å$^{-1} < q < 0.006$ Å^{-1}) are observed at different particle concentrations. The behavior at low q values can no

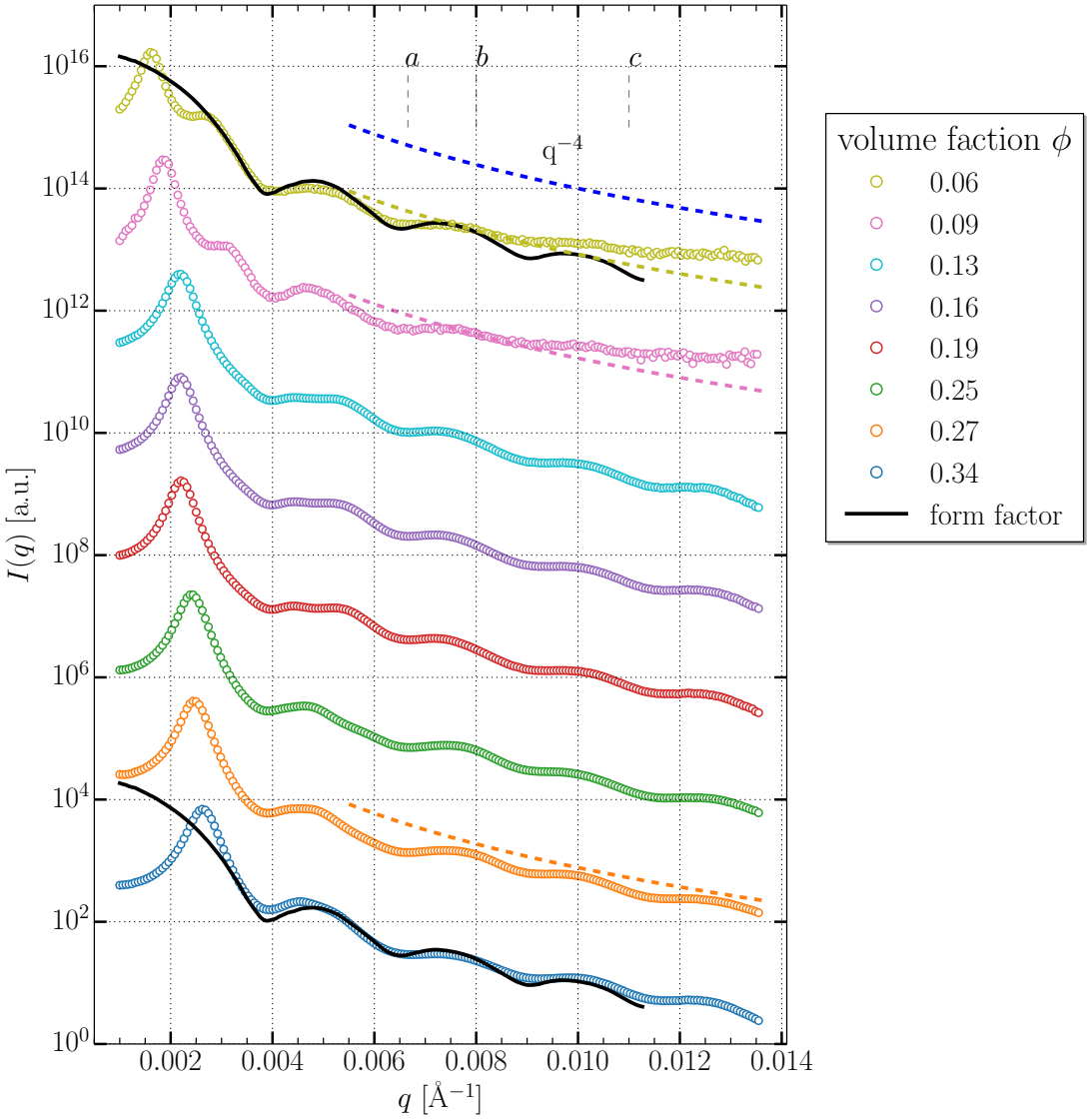

Figure 4.2: Scaled intensity profiles as a function of momentum transfer q for different volume fractions. Dashed lines show the slope of q^{-4}. The solid black line is a scaled form factor from Fig. 5.1. The values a, b and c define q regions for scaling of the intensity curves and the form factor.

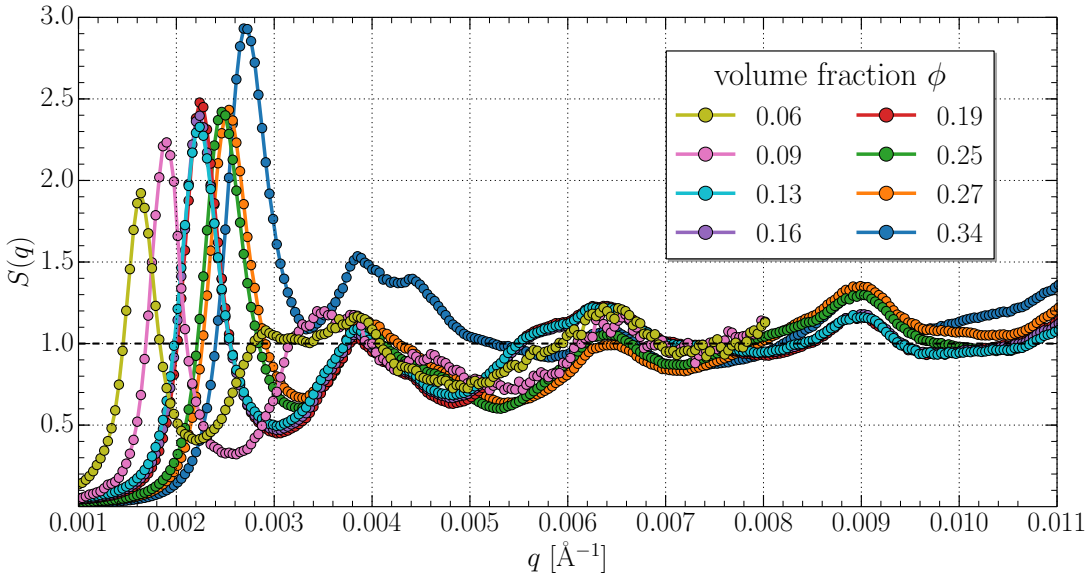

Figure 4.3: Static structure factors $S(q)$ of PA particles as a function of momentum transfer q for different volume fractions.

longer be described by the particle form factor $P(q)$ (solid line) due to direct inter-particle interactions. In order to quantify these interactions the structure factor $S(q)$ was calculated by dividing the measured data $I(q)$ by the experimental form factor $P(q)$ (see Fig. 4.2)[1]. The scattering profiles $I(q)$ were first scaled to the form factor intensity curve $P(q)$ in the q regions 0.0067 Å$^{-1} < q < 0.011$ Å^{-1} and 0.0067 Å$^{-1} < q < 0.008$ Å^{-1} for samples with $\phi < 0.13$ and $\phi \geq 0.13$, respectively. These regions are shown in the Fig. 4.2 as intervals ac and ab.

The extracted static structure factors $S(q)$ are shown in Fig. 4.3 as a function of momentum transfer q. $S(q)$ shows a pronounced peak at small momentum transfers q and oscillates toward unity at large q. $S(q)$ shows further maxima in 3 q-regimes ($q \sim 0.004$ Å^{-1}, $q \sim 0.0065$ Å^{-1}, $q \sim 0.009$ Å^{-1}) for all samples (see Fig. 4.3). They coincide with the minima of the form factor and may arise from the mismatch between form factor and intensity curves for interacting samples (see Fig. 4.2).

The positions of the first structure factor peak shift to higher momentum transfers q with increasing particle concentration. The respective peak values $S(q_{\text{peak}})$ increase, except for volume fractions of 0.25 and 0.27. However, the amplitude of the first structure factor peak $S(q_{\text{peak}})$ depends on the scaling region chosen for the particle form factor $P(q)$ and the intensity curve $I(q)$ to extract $S(q)$. The uncertainty of the peak amplitude $S(q_{\text{peak}})$ was determined by extracting $S(q)$ with two different scaling regions. The results of the first scaling are shown above (see Fig. 4.2). In the second case scattering profiles $I(q)$ were scaled to the form factor intensity curve $P(q)$ in the

[1] The experimental form factor was smoothed.

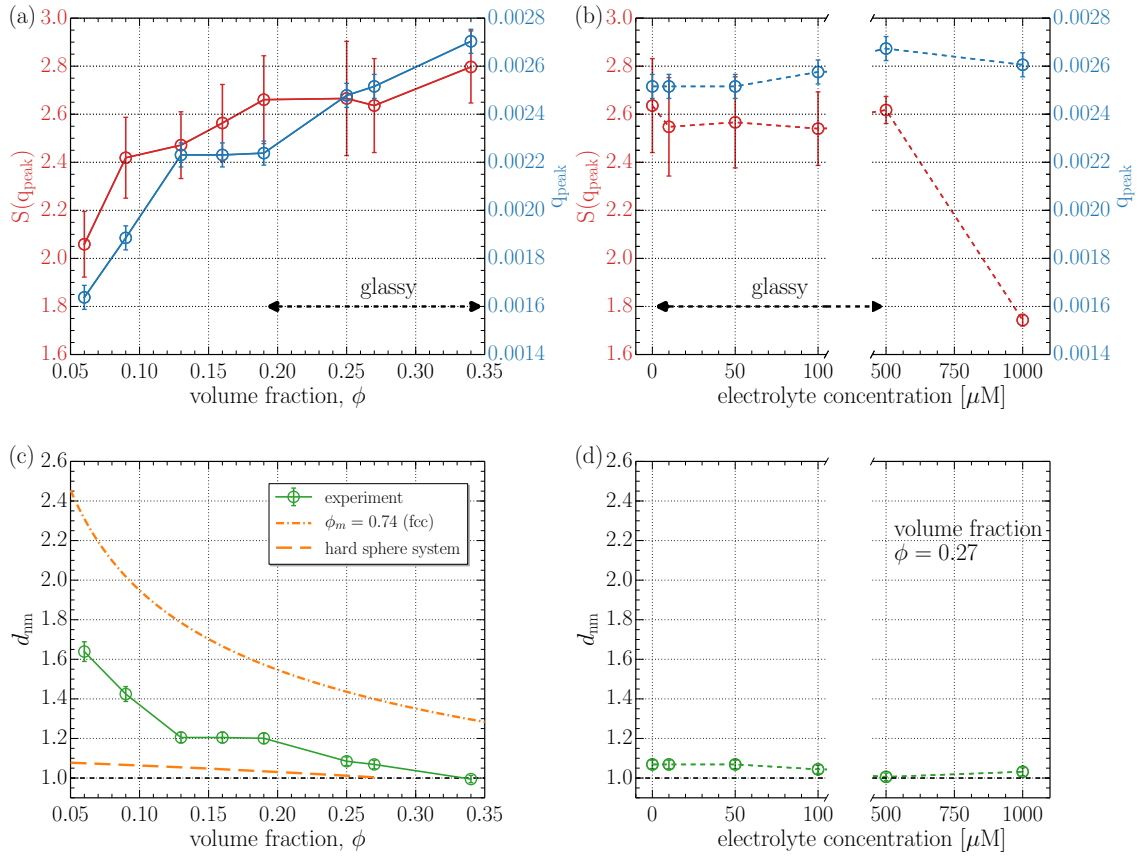

Figure 4.4: Static structural parameters. Amplitude of the structure factor peak $S(q)$ and its position q_{peak} as a function of volume fraction ϕ (a) and electrolyte concentration (b). Normalized mean interparticle distance d_{nm} as a function of the volume fraction ϕ (c) and electrolyte concentration (d). The volume fraction of samples in (b) and (c) is constant $\phi = 0.27$. In (c) the dashed orange line corresponds to a model of hard spheres, the dotted orange line corresponds to an fcc model. The dashed black line in (c) and (d) shows the minimum possible interparticle distance of 1.

q regions 0.004 Å$^{-1} < q < 0.011$ Å^{-1} and 0.004 Å$^{-1} < q < 0.008$ Å^{-1} for samples with $\phi < 0.13$ and $\phi \geq 0.13$, respectively.

In Fig. 4.4 (a) the amplitude of the structure factor peak $S(q_{\mathrm{peak}})$ and its position q_{peak} are shown as a function of volume fraction. The uncertainties are shown by the errorbars. The amplitude of the structure factor peak $S(q_{\mathrm{peak}})$ characterizes pair correlations within the sample and can be considered as a measure of degree of translational order within the sample. $S(q_{\mathrm{peak}})$ increases with increasing volume fraction ϕ up to a concentration of $\phi = 0.19$. In the phase diagram of charge stabilized particles (see Fig. 1.4) samples at volume fractions $0.13 \leq \phi \leq 0.19$ are in the crystal regions – fcc, coexistence of fcc and bcc, and bcc. Due to the absence of Bragg reflections, the structure factor analysis does not indicate a crystal phase for these samples. However, these samples crystallized within two months after the experiment. Therefore samples

at $0.13 \leq \phi \leq 0.19$ can be considered to be in a metastable liquid state. At a volume fraction of $\phi = 0.19$ the amplitude reaches a value around 2.6 and stays almost constant with increasing volume fraction up to $\phi = 0.34$. These volume fractions are in the glassy region on the phase diagram.

The position of the structure factor peak q_{peak} does not depend on the chosen scaling region for form factor $P(q)$ and intensity profile $I(q)$. The peak position q_{peak} increases with volume fraction with a small plateau between $\phi = 0.16$ and $\phi = 0.19$ (Fig. 4.4 (a)).

When volume fractions are far from unity the position of the peak is related to the mean interparticle distance by

$$d_{\mathrm{m}} \approx 2\pi / q_{\mathrm{peak}} \; . \tag{4.2}$$

In Fig. 4.4 (c) the normalized mean interparticle distance $d_{\mathrm{nm}} = d_{\mathrm{m}}/(2R_0)$ is shown as a function of the volume fraction ϕ. d_{nm} decreases with increasing volume fraction, as expected since at higher volume fractions the system is more compressed. The minimum possible interparticle distance is 1. For the most concentrated system of $\phi = 0.34$ the parameter d_{nm} is close to unity. Also in Fig. 4.4 (c) the dependence of the normalized mean interparticle distance on volume fraction for hard sphere system is shown. The distance has been calculated from the peak position of structure factors of hard spheres. The structure factors have been obtained within Percus-Yevick approximation [215]. Note that within this model the mean interparticle distance can be estimated reliably only up to volume fraction of 0.27. The normalized mean interparticle distance d_{nm} for PA samples with volume fractions up to $\phi = 0.27$ is above the one for hard spheres due to electrostatic interactions between particles. An upper limit for d_{nm} as a function of the volume fraction ϕ is given by the mean interparticle distance between the colloidal particles placed in the fcc lattice that has a maximum packing factor of $\phi_{\mathrm{m}} = 0.74$. In this case the normalized mean interparticle distance at a particular ϕ has been calculated as $(\phi_{\mathrm{m}}/\phi)^{1/3}$ [216] and is presented in Fig. 4.4 (c). The normalized mean interparticle distance d_{nm} is below the maximum possible geometrical distance for all PA samples.

The electrostatically stabilized particles are usually described by the RMSA model (see section 1.3). However, the observed structure factors do not follow the behavior expected in this approximation. This is illustrated for the sample with $\phi = 0.27$ in Fig. 4.5 by the dashed line showing the calculated RMSA structure factor for $R = 1165$ Å. It is clear from the figure that the fit of this model does not describe the measured data. Modeling of the static data therefore requires the development of a more adapted approach which is beyond the scope of this work.

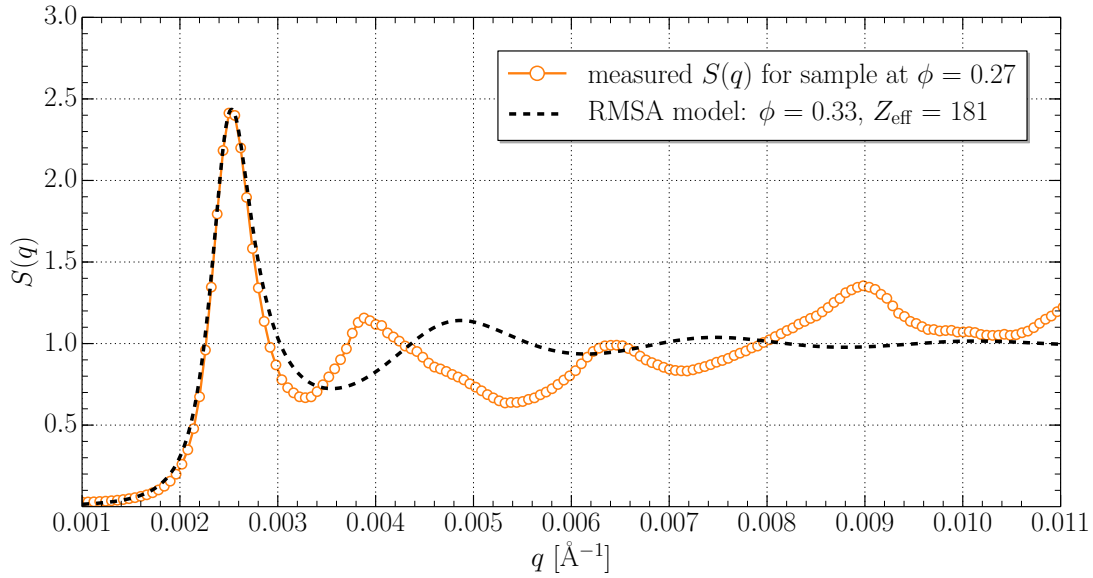

Figure 4.5: Static structure factors $S(q)$ of PA particles as a function of momentum transfer q for $\phi = 0.27$ (circles). The dashed line shows a calculated structure factor by RMSA model (dashed line) with parameters $\phi = 0.33$ and $Z_{\text{eff}} = 181$.

.

By keeping a constant volume fraction of one sample ($\phi = 0.27$) and adding salt to the dispersion the static behavior was studied as a function of the electrolyte concentration. The intensity profiles as a function of momentum transfer q for different electrolyte concentrations are shown in Fig. 4.6. The structure factors were extracted in a similar way to the case of different volume fractions that was considered above. The scaling region is marked by values a and c in Fig. 4.6.

The structure factors $S(q)$ are shown in Fig. 4.7. They are mostly unchanged at low electrolyte concentrations (≤ 100 μM). At high q values the structure factors deviate from unity as before. The high q regime shows also spurious maxima.

The amplitude $S(q_{\text{peak}})$ and position q_{peak} of the first peak of the structure factor $S(q)$ were analyzed in a similar way to the case of different volume fractions[2]. The dependencies of $S(q_{\text{peak}})$ and q_{peak} on electrolyte concentration are shown in Fig. 4.4 (b). From the peak position the normalized mean interparticle distance d_{nm} is calculated. Its dependence on electrolyte concentration is shown in Fig. 4.4 (d). The amplitude of the structure factor peak $S(q_{\text{peak}})$ is almost unchanged for samples with electrolyte concentration up to 500 μM and decreases dramatically for the highest salt concentration of 1000 μM. This is consistent with the phase diagram for charge stabilized colloids (see Fig. 1.4). In the phase diagram (see Fig. 1.4) samples with

[2]To define the uncertainties structure factor $S(q)$ was also obtained with scaling region in q of 0.004 Å$^{-1} < q < 0.011$ Å^{-1}

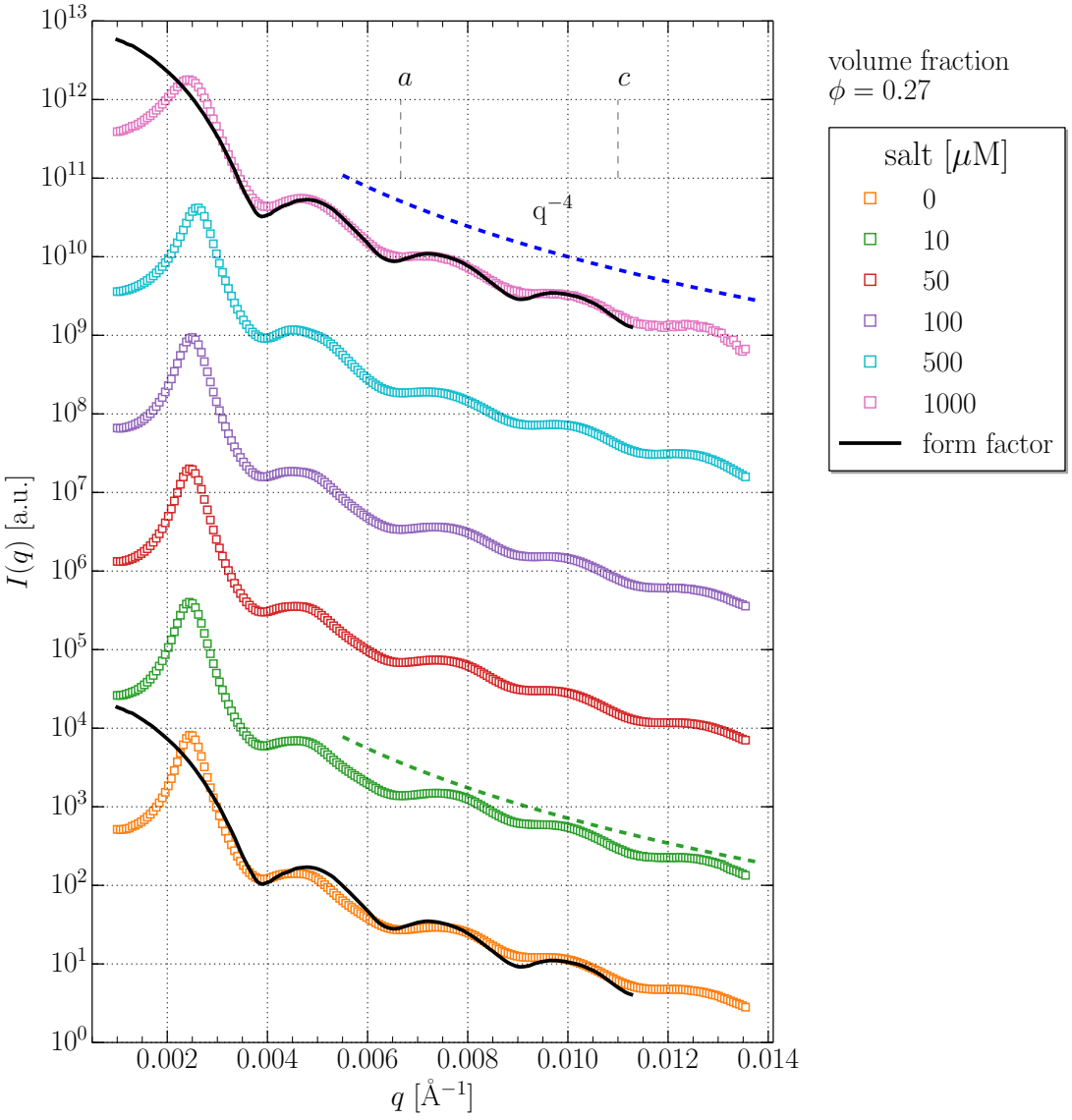

Figure 4.6: Scaled intensity profiles $I(q)$ as a function of momentum transfer q for different electrolyte concentrations. Dashed lines show the slope of q^{-4}. The solid black line is a scaled form factor intensity. The values a and c define q regions for scaling of the intensity curves and the form factor.

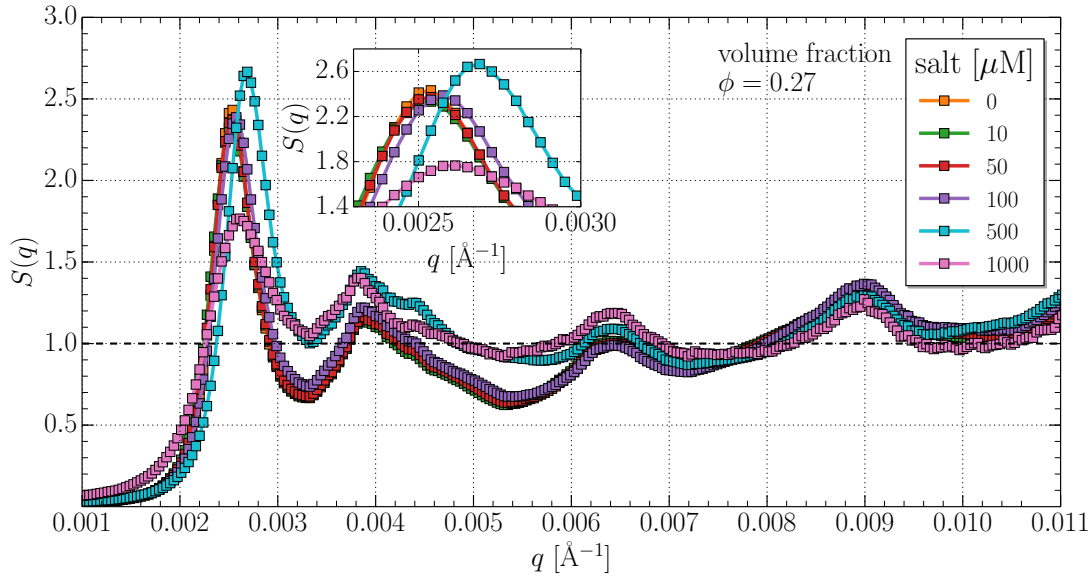

Figure 4.7: Static structure factors $S(q)$ of PA particles as a function of momentum transfer q for different electrolyte concentrations at volume fraction $\phi = 0.27$. The inset shows a scaled region around the first structure factor peak.

electrolyte concentration up to 500 μM lie in the glassy state and glass to crystal transition, while the sample with 1000 μM electrolyte concentration is located in the liquid region. The position of q_{peak} (see Fig. 4.4 (b)) and the normalized mean interparticle distance d_{nm} (see Fig. 4.4 (d)) do not change dramatically depending on the electrolyte concentration as they do in response to changes in the volume fraction ϕ (see Fig. 4.4 (a) and (c)). This is consistent with the fact that the particle concentration stays constant. Samples with electrolyte concentration below 100 μM on phase diagram are in the glassy phase (see Fig. 1.4), and q_{peak} and d_{nm} are almost unchanged. The maximum (minimum) in q_{peak} (d_{nm}) is observed at an electrolyte concentration of 500 μM (Fig. 4.4 (b) and (d)), at which the sample is assumed to be in the crystal phase (see Fig. 1.4). The following decrease (increase) of q_{peak} (d_{nm}) might be connected with transition to liquid phase for sample with 1000 μM of salt.

The behavior of the $S(q_{\mathrm{peak}})$ – almost constant for volume fractions $\phi > 0.19$ and for small amounts of salt up to 500 μM – motivates the investigation of local orientational order in PA samples at different volume fractions and electrolyte concentrations. The investigation of the local order, however, is beyond the scope of conventional SAXS analysis. It required another approach which will be which will be discussed in section 4.4.

4.3 Dynamics of colloidal particles

The dynamics of PA particles were investigated in this work via XPCS (see section 2.6). In the first part of the section two important limitations of the XPCS data analysis are considered: radiation damage and Poisson noise at low intensities[3] [217, 218]. Radiation induced damage of the PA particles in XPCS experiments is discussed in subsection 4.3.1. The signal-to-noise ratio (SNR) is evaluated in section 4.3.2. Afterwards, results of the XPCS analysis are presented and discussed for different particle and electrolyte concentrations (see section 4.3.3).

4.3.1 Observation of the sample radiation damage

Radiation damage presents a challenge for dynamical investigations of colloidal dispersions by XPCS [219, 220]. Charge stabilized particles are susceptible to various kinds of damage upon prolonged exposure to X-ray radiation, e.g. atomic ionization that can affect the inter-particle interactions. Typically the radiation induced damage is cumulative over time. One way to track the radiation induced damage of the sample is to compare the scattered intensity at different times in the XPCS series.

Fig. 4.8 illustrates the effects of radiation damage on scattering patterns using the sample with volume fraction of $\phi = 0.09$ as an example. Scattering intensity patterns were recorded in continuous mode (open shutter) with exposure time of 0.003 s per pattern. A single masked scattering intensity pattern is shown in Fig. 4.8 (a). The total scattered intensity I_{tot} per pattern was obtained by averaging over all pixels excluding the masked ones. Fig. 4.8 (b) shows the intensity $\langle I_{tot} \rangle_5$ averaged over groups of 5 subsequent patterns as a function of the elapsed experimental time. The intensity changes less than 2 percent in the first 0.3 s, and the sample is considered undamaged in this timeframe. The decrease in intensity at longer times indicates radiation induced damage in the sample. One of the possible explanations of the observed effect is ionization of the particles by X-rays and therefore a change of the inter-particle interactions. For example, a stronger repelling force between the particles can lead to local structural changes, e.g. decrease of the particle concentration in the sample area illuminated by X-rays. In order to test for these structural changes the intensity profiles $I(q)$ averaged over the first 5 and the last 5 scattering intensity patterns are compared in Fig. 4.8 (c). The position of the first peak in the intensity $I(q)$ coincides with the maximum position of the structure factor $S(q)$. Fig. 4.8 (c) demonstrates that with time the maximum of the intensity profile $I(q)$ shifts to lower q values. Therefore, the inter-particle distance increases and the particle concentration becomes smaller.

[3] Poisson noise is proportional to square root of intensity and is therefore more significant at low signal counts

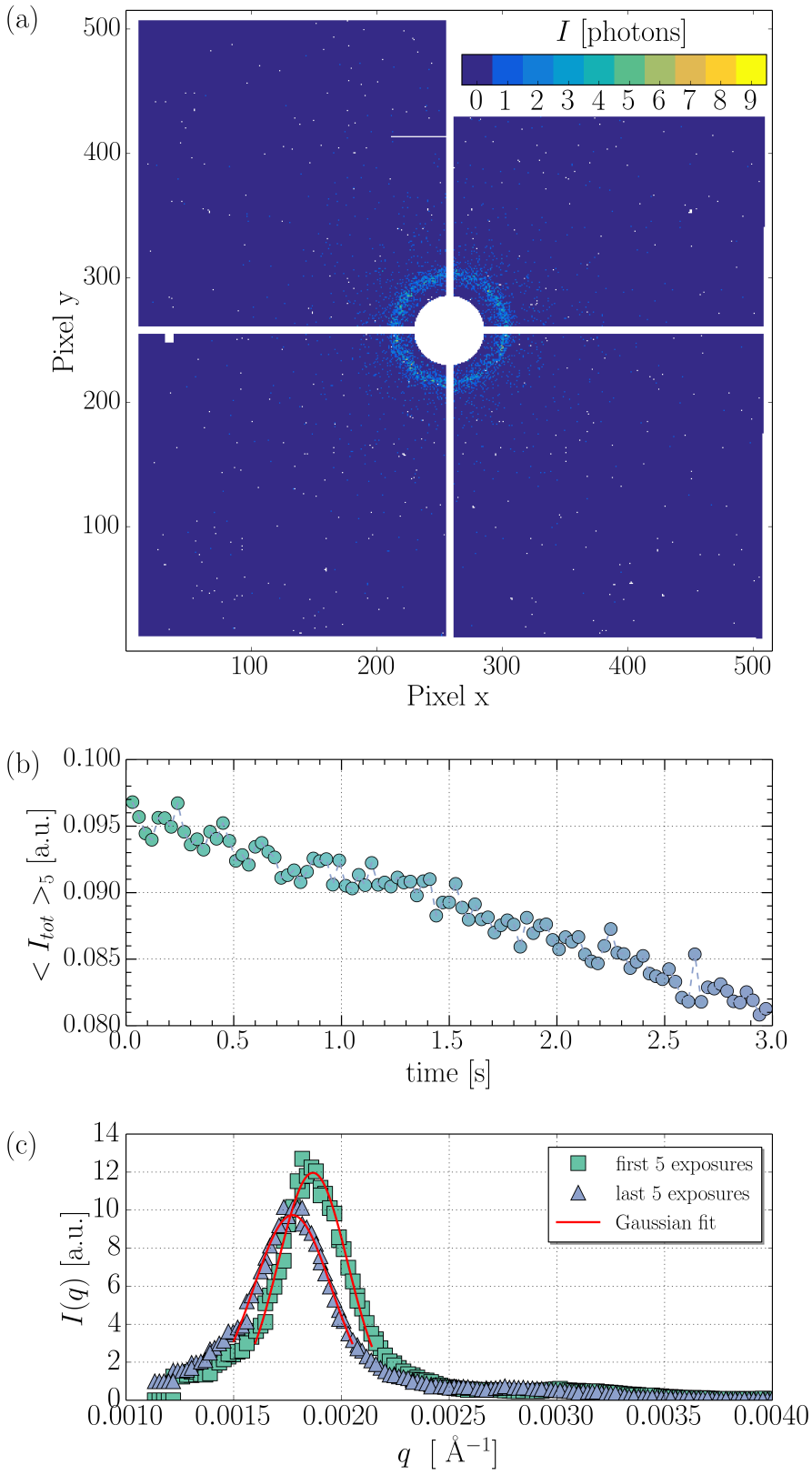

Figure 4.8: Beam damage observations for the sample with volume fraction $\phi = 0.09$. (a) A single masked scattering intensity pattern taken with exposure time of 0.003 s. (b) The total scattered intensity $\langle I_{tot} \rangle_5$ averaged over every 5 exposures as a function of time. (c) The radial scattered intensity profiles $I(q)$ averaged over the first 5 (green squares) and the last 5 (blue triangles) exposures of a series of 1000 scattering intensity patterns. Red curves are Gaussian fits of the first peak intensity profile.

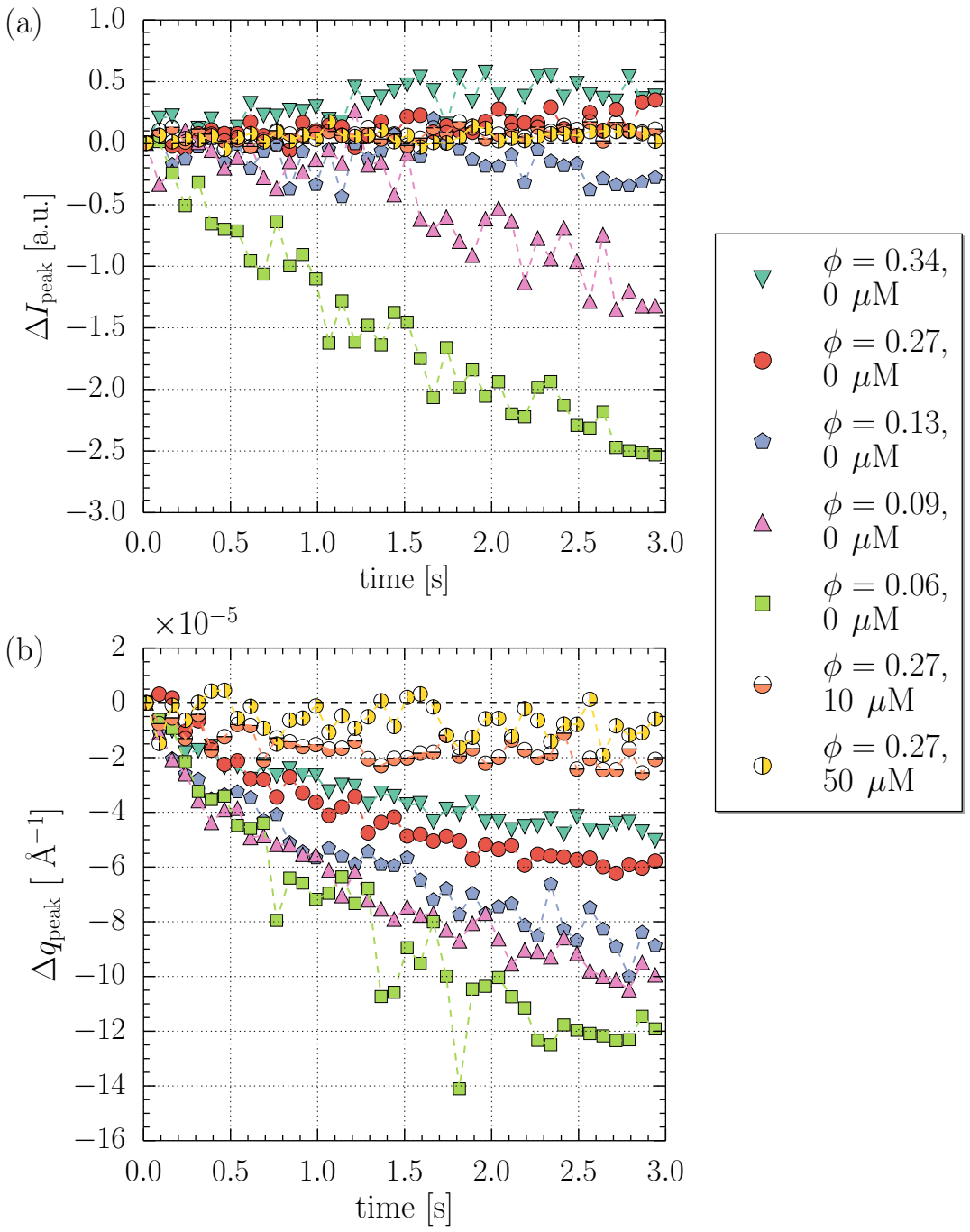

Figure 4.9: Beam damage observation. The absolute change of the amplitude (a) and peak position (b) to its initial positions obtained from the Gaussian fits as a function of the elapsed experimental time for samples with different particle (full-filled markers) and electrolyte (half-filled circles) concentrations.

The decreasing amplitude of the peak supports this proposition.

The first peak of the intensity profile $I(q)$ was fitted with a Gaussian function (see Fig. 4.8 (c)). The amplitudes and positions of the peak obtained through fitting were used to evaluate the degree of the sample damage with time depending on particle and electrolyte concentrations. Absolute changes of the amplitude and position of the peak as a function of elapsed experimental time are presented in Fig. 4.9 (a) and (b), respectively. Each curve corresponds to a different sample[4]. For samples without additional electrolyte different behavior of the peak amplitude is observed. For high sample volume fractions ($\phi \geq 0.27$) the amplitude increases with time while for low particle concentration ($\phi \leq 0.25$) it decreases. However, the peak position for all samples shifts to smaller q-values with time. As discussed above the smaller amplitude values and the shift of the peak position can be due to a decrease in the number of PA particles within the illuminated part of the sample. This decrease is attributed to the stronger repelling force between particles due to particle ionization under X-ray irradiation. In case of high volume fractions the amplitude increase might suggest particle ordering in the local illuminated area. Much less significant changes in peak position and amplitude are observed for samples with non-zero electrolyte concentration. The addition of ions in the solution screens the surface charges of particles and makes the particle behavior more similar to hard spheres, and therefore less sensitive to the X-ray dose. The observed data leads to a possible conclusion that low concentrated PA samples are more sensitive to the X-ray dose, while additional salt may reduce the radiation damage and decrease the amount of structural changes.

Several approaches can be applied to mitigate effects of radiation damage: introducing a time delay between X-ray exposures, reducing exposure time and attenuating the incident beam. However despite these measures radiation induced damage was still observed in most XPCS runs.

Therefore, in the following XPCS data analysis the sample is considered to be undamaged when two conditions are satisfied. First, the total intensity deviates less than 10% from its initial value; second, the first peak in $I(q)$ does not change its amplitude by more than 10% and its position is defined within 2% of its width.

4.3.2 Signal-to-noise ratio in XPCS at different q values

XPCS is a technique that strongly depends on the precise determination of the scattered signal in every diffraction pattern. Thus, it is important to optimize experimental conditions as much as possible to obtain a sufficient signal-to-noise ratio (SNR). However, options for increasing SNR are limited because the radiation damage

[4]Parameters of the runs such as exposure time, delay time and attenuation are the same for all samples.

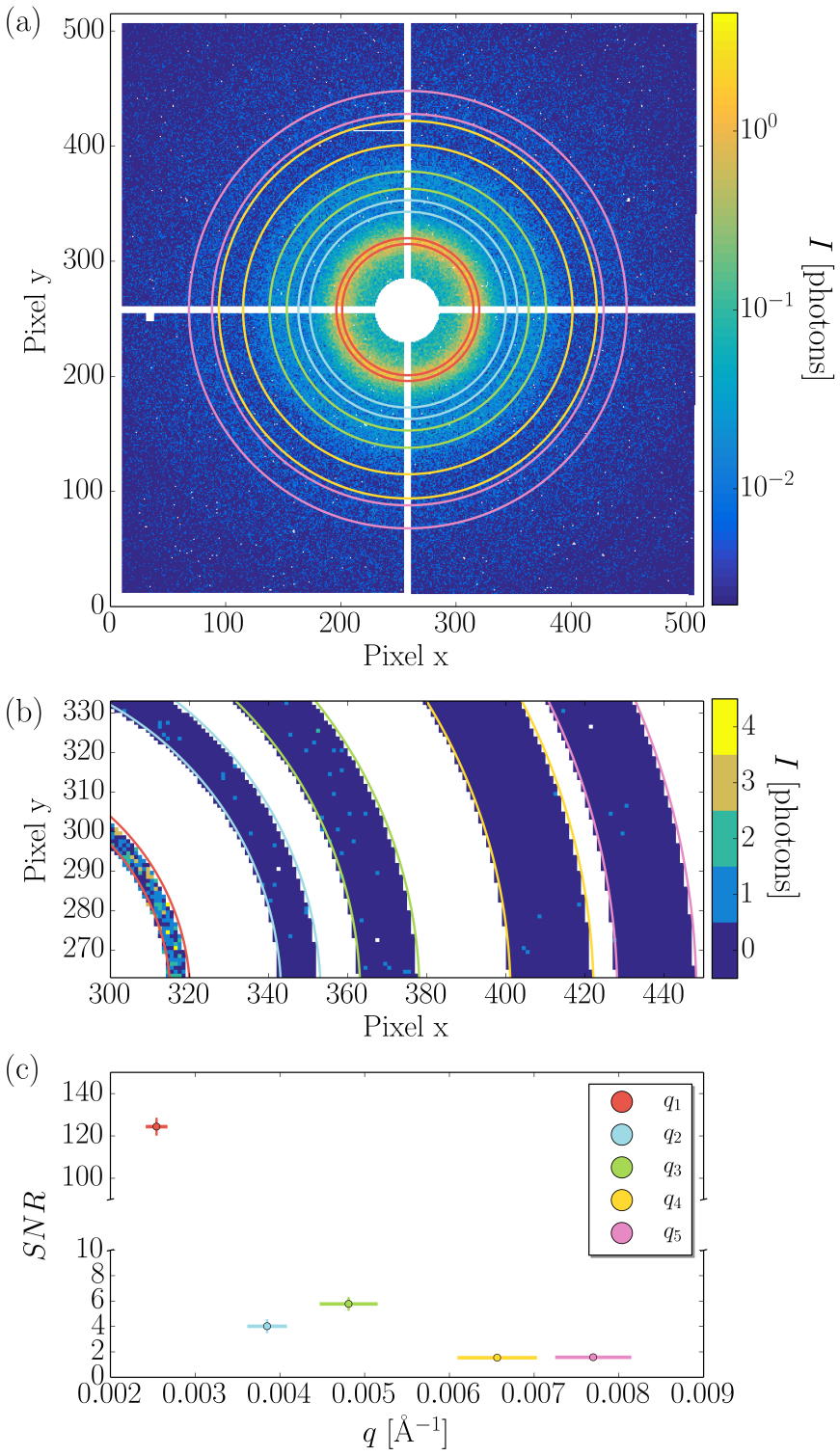

Figure 4.10: The signal-to-noise ratio. (a) Scattering signal averaged over 200 scattering patterns for the sample with $\phi = 0.27$. The five rings show different q-partitions for SNR analysis. (b) Expansion of small region of a single scattering pattern masked by five rings shown in (a). (c) SNR calculated at different q-rings indicated in legend. The horizontal lines at the points show the width of the q-rings. The vertical ones are error bars of the SNR.

defines an upper boundary for the total X-ray dose and incident intensity. Therefore, values of the SNR are further estimated in different q-regions.

The following demonstration of a SNR analysis is performed for a sample with volume fraction $\phi = 0.27$. The XPCS measurements were performed in the frame mode (see section 3.2.2) with 5 s delay between exposures. Such experimental parameters mostly prevent the sample from being damaged by radiation during the XPCS run. Fig. 4.10 (a) shows the scattered signal averaged over 200 measured patterns together with highlighted q-rings. The corresponding central q-positions and width dq of the rings are:

- $q_1 = 0.0025$ Å^{-1} with d$q = 0.0002$ Å^{-1},
- $q_2 = 0.0038$ Å^{-1} with d$q = 0.0004$ Å^{-1},
- $q_3 = 0.0048$ Å^{-1} with d$q = 0.0006$ Å^{-1},
- $q_4 = 0.0066$ Å^{-1} with d$q = 0.0009$ Å^{-1},
- $q_5 = 0.0077$ Å^{-1} with d$q = 0.0008$ Å^{-1}.

The q_1, q_3, q_5-rings and q_2, q_4-rings correspond to the first three local maxima and the first two local minima of $I(q)$, respectively.

Fig. 4.10 (b) shows sectors of a single scattering pattern masked by these q-rings. Radial intensity is nearly uniform within each ring. The SNR at a certain q-ring can be calculated by [218]

$$SNR = \beta I (T_a \tau n_{pix})^{1/2} \, . \tag{4.3}$$

Here, β is the speckle contrast ($\beta \sim 0.22$), I is the mean intensity per pixel per time, τ is the accumulation time, T_a is the total accumulated time in the XPCS series and n_{pix} is the number of pixels in the q-ring.

The SNR results obtained for 200 scattering intensity patterns ($T_a = 0.6$ s) are shown in Fig. 4.10 (c). The SNR decreases non-monotonically with q (e.g. SNR at q_2 and q_3). At q_1 it is a factor of 20 higher in comparison to other q_i-rings. The SNR values at the first intensity maximum were found to be between 26 and 250 for different samples. For all of the samples the SNR at the first intensity maximum is a factor of more than 15 – 20 higher than SNR at the rings with larger q. Typically SNR values at larger q-rings are less than 7. Such small values of SNR make obtaining XPCS results impossible [117, 132], and thus only the q-region corresponding to the first intensity peak was selected to perform XPCS analysis.

4.3.3 Dynamics of the PA samples

In order to investigate the sample dynamics a time series of speckle patterns was recorded following the XPCS measurement scheme described in section 3.2.2. The

data was corrected by the detector flatfield. The pixels behind the beamstop, broken pixels and detector gaps were masked. These pixels will be called masked pixels in the following. XPCS data were first checked for radiation damage effects in order to choose only scattering patterns from undamaged samples for the subsequent XPCS data analysis. Depending on the sample and the run the number of obtained scattering patterns varied from 10 to 500.

The two-dimensional (pixel) detection scheme enables the calculation of the autocorrelation function (see Eq. (2.42) in the form [221]:

$$g^{(2)}(q,\Delta t) = \frac{\langle\langle I_p(t) I_p(t+\Delta t)\rangle_t\rangle_p}{\langle\langle I_p(t)\rangle_t\rangle_p^2} \,, \tag{4.4}$$

where $I_p(t)$ is the intensity measured by a detector pixel p, $\langle\rangle_t$ denotes the time average over all frames, and $\langle\rangle_p$ is an average over all pixels in the region of interest (ROI), here given as ring defined by q.

Based on the SNR values for different q values discussed in the previous section, the XPCS data analysis is restricted to the region corresponding to the first peak of $I(q)$. The position of the first peak of $I(q)$ almost coincides with the maximum of the structure factor $S(q)$. The q-position of the ROI was chosen around the first peak of $S(q)$. The typical thickness of a q-ring is d$q = 0.00013$ Å^{-1} (~ 3 pixels). Fig. 4.11 shows the ROI for the sample with volume fraction $\phi = 0.34$. The upper right quadrant of the speckle pattern and corresponding ROI around the peak of $S(q)$ are shown in Fig. 4.11 (a) and (b), respectively.

Since the dynamical behavior of the sample was unknown before the experiment the measurements were performed with different XPCS parameters: the exposure time, the delay time between two exposures, and the beam attenuation (see section 3.2.2). As an example the $g^{(2)}(q_{\text{peak}},\Delta t)$ functions obtained from two XPCS runs for the sample with volume fraction $\phi = 0.34$ are shown in Fig. 4.12. The first run was performed in the continuous mode, the second in the frame mode with 2 s delay between exposures. The exposure time was 0.003 s for both runs. The second run was effectively a continuation of the first one, since sample dynamics were too slow in comparison to the total duration of the first run. The data from two runs can be joined after renormalization of the $g^{(2)}(q,\Delta t)$ function to account for differences in contrast between runs. The correlation function $g^{(2)}(q,\Delta t)$ can be represented in the form (see eq. (2.44) in section 2.6.2)

$$g^{(2)}(q,\Delta t) = B + \beta |g^{(1)}(q,\Delta t)|^2 \,. \tag{4.5}$$

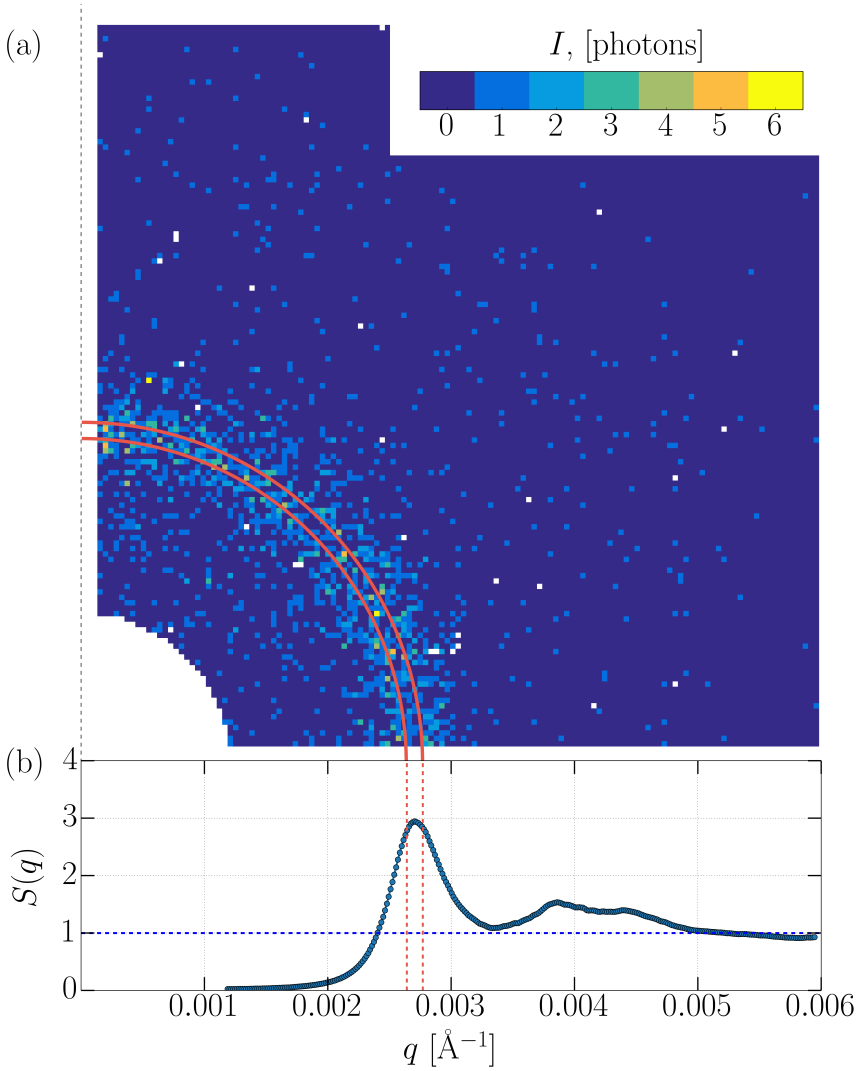

Figure 4.11: Part of the upper right quadrant of a single scattering pattern (a) and structure factor $S(q)$ (b) for the sample with $\phi = 0.34$. The red lines show the limits of the q-region used in XPCS analysis, colorbar is linear scale.

The baseline B was determined from dilute sample series as $B = 1.000 \pm 0.005$. The contrast β varies between 0.2 and 0.3. For the correlation functions presented in Fig. 4.12 the values of β are $\beta_1 \simeq 0.22$ and $\beta_2 \simeq 0.23$ for the first and second runs, respectively. Each correlation function was corrected to the baseline $B = 1.0$ and normalized by the contrast β_i

$$|g^{(1)}(q, \Delta t)|^2 \equiv g_n^{(2)}(q, \Delta t) = \frac{1}{\beta}(g^{(2)}(q, \Delta t) - 1) \, . \tag{4.6}$$

As shown in section 2.6.3 the experimentally obtained intensity correlation function can be connected to the sample dynamics within the Kohlrausch-Williams-Watts (KWW) model. Therefore, the normalized and joined $g_{nj}^{(2)}(q, \Delta t)$ function was fitted

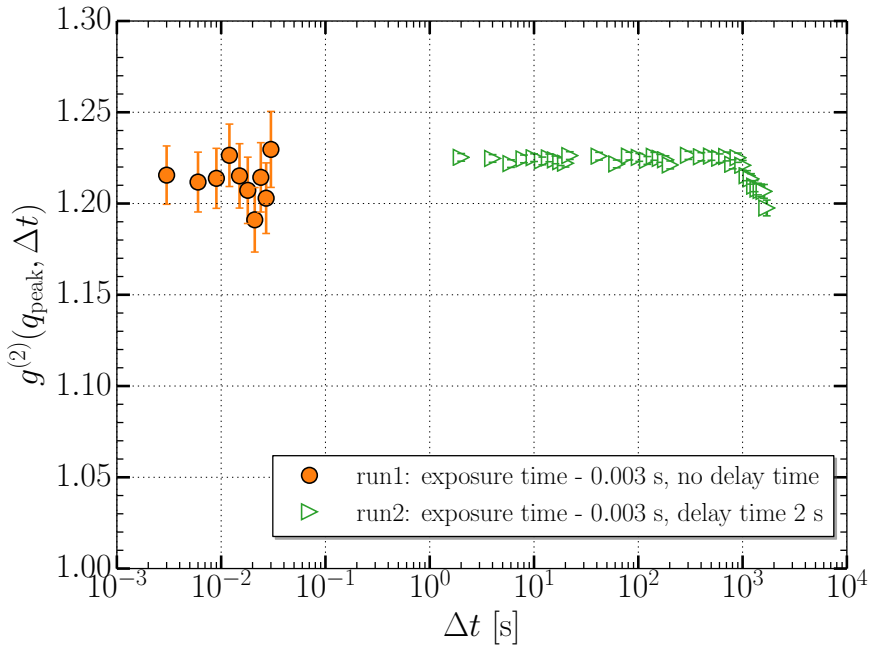

Figure 4.12: The $g^{(2)}(q_{peak}, \Delta t)$ correlation functions detected at the $q_{peak} = 0.0027\text{Å}^{-1}$ for sample with $\phi = 0.34$. The parameters (exposure time and delay time between frames) of the XPCS runs are presented in legend.

with a stretched exponential decay

$$g_{nj}^{(2)}(q, \Delta t) = e^{-2(\Delta t/\tau)^{\gamma}} \ . \tag{4.7}$$

Note that the fit was performed only if a drop of more than 8% in the $g_{nj}^{(2)}(q, \Delta t)$ function was observed. Fig. 4.13 shows the resulting normalized $g_{nj}^{(2)}(q_{\text{peak}}, \Delta t)$ functions at the first maximum of $S(q)$ and their fits for samples with different volume fractions. The fit could not be performed for samples with $\phi = 0.27$ and $\phi = 0.25$ due to insufficient probing of the decay region. However, from the constant behavior of $g_{nj}^{(2)}(q_{\text{peak}}, \Delta t)$ it can be concluded that the relaxation time for these samples is longer than 500 s. In the same way the dynamical properties of samples with different salt concentrations were analyzed. The results are shown in Fig. 4.14. The obtained fit parameters, the characteristic relaxation time τ and stretching exponential parameter γ as a function of volume fraction and electrolyte concentration are shown in Fig. 4.15 and Fig. 4.16, respectively.

Different dynamics are observed for PA particles depending on volume fraction and electrolyte concentration. The relaxation time varies from as short as 1 s for the lowest volume fraction $\phi = 0.06$ up to 7×10^3 s for the highest volume fraction $\phi = 0.34$ (see Fig. 4.15). The stretching parameter γ changes from 2 to 0.5 with decreasing particle concentration (see Fig. 4.16). When the volume fraction is fixed at $\phi = 0.27$

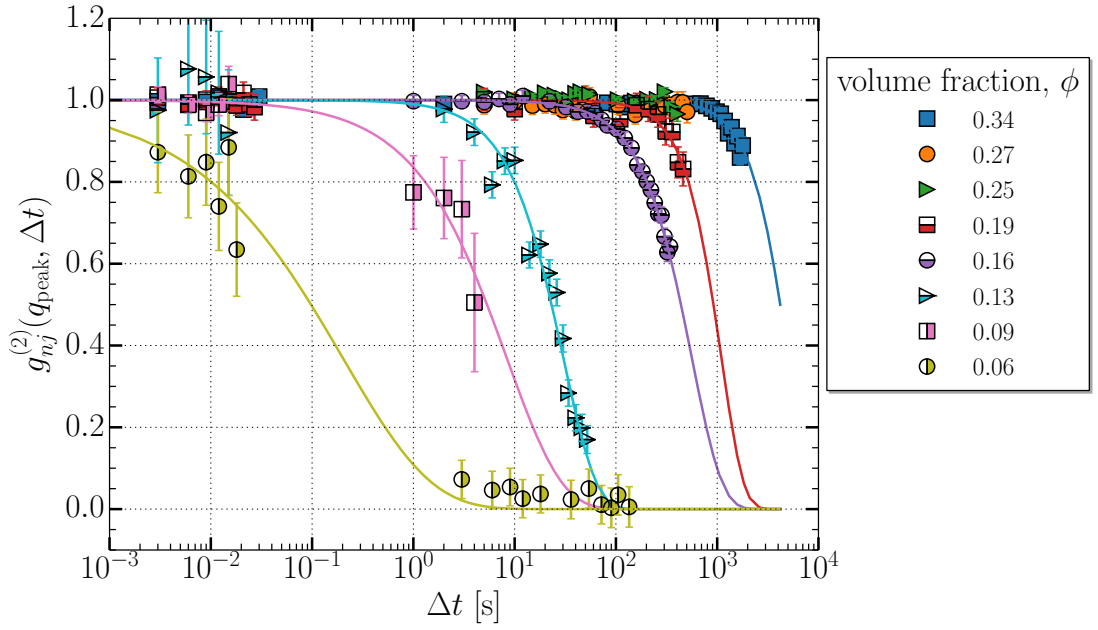

Figure 4.13: Normalized and joined intensity autocorrelation functions $g^{(2)}_{nj}(q_{\text{peak}}, \Delta t)$ as functions of the lag time Δt for samples with different volume fraction ϕ indicated in the legend. The autocorrelation functions have been calculated at the momentum transfer value q_{peak} corresponding to the first maxima of $S(q)$. The solid lines show fits of Eq. (4.7).

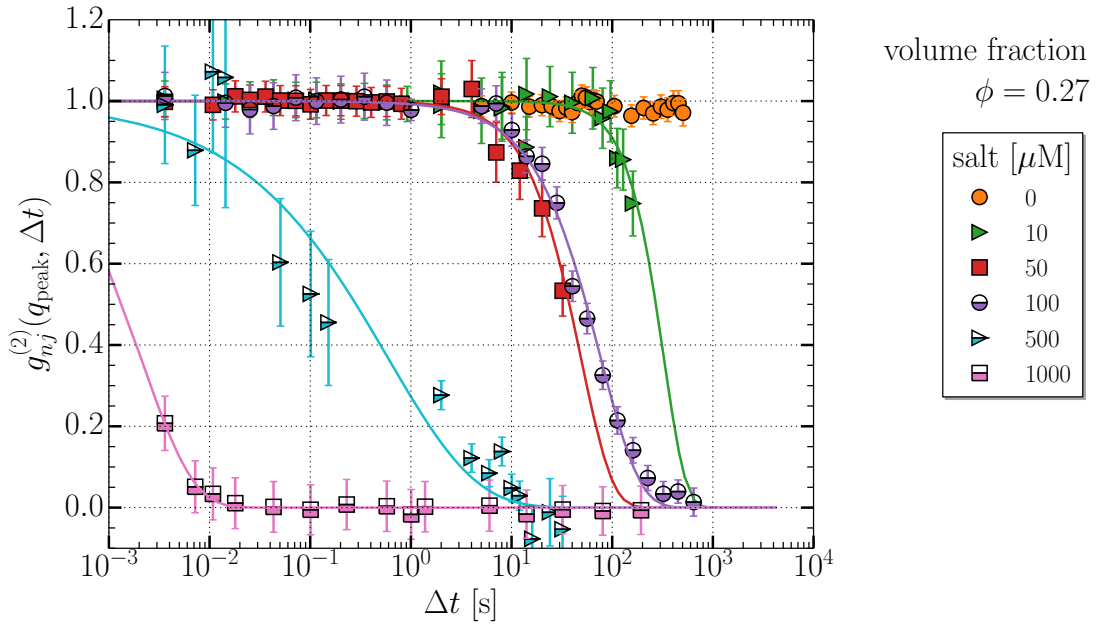

Figure 4.14: Normalized and joined intensity autocorrelation functions $g^{(2)}_{nj}(q_{\text{peak}}, \Delta t)$ as functions of the lag time Δt for samples with volume fraction $\phi = 0.27$ and different amount of salt indicated in the legend. The autocorrelation functions have been calculated at the momentum transfer value q_{peak} corresponding to the first maxima of $S(q)$. The solid lines show fits of Eq. (4.7).

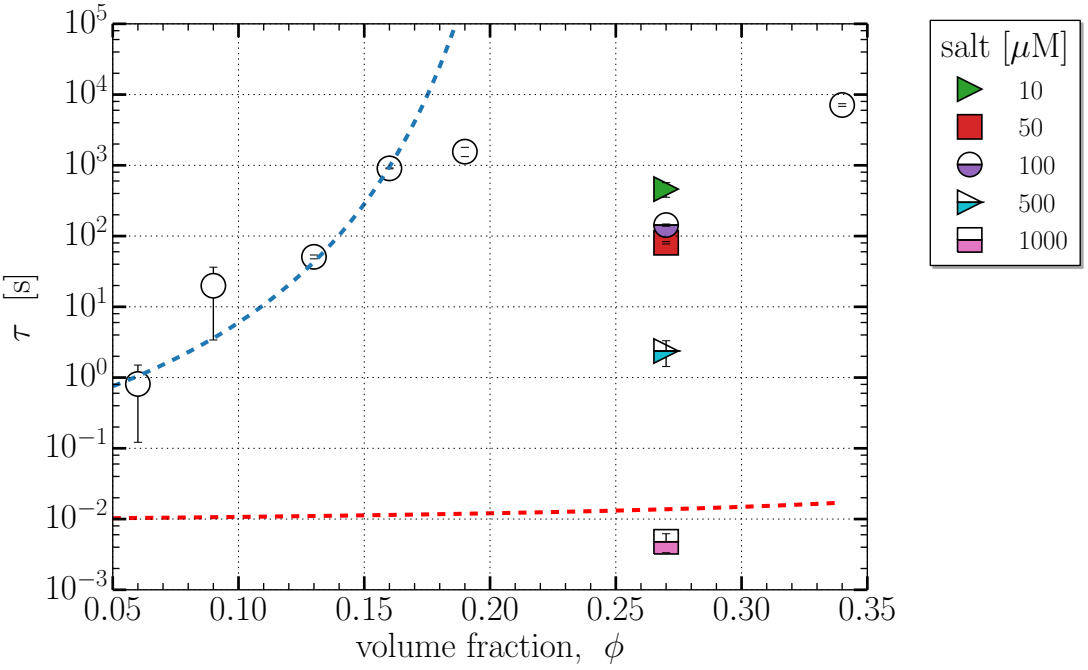

Figure 4.15: The characteristic relaxation time τ as a function of sample's volume fraction ϕ and electrolyte concentration (see legend). The relaxation times τ have been obtained from the fits of autocorrelation functions $g^{(2)}_{nj}$ (see Fig. 4.13 and Fig. 4.14)) with Eq. (4.7). The dashed blue line is a fit of Vogel-Fulcher-Tammann model (Eq. (4.8)) with parameter $\phi_0 = 0.27$. The dashed red line is a Vogel-Fulcher-Tammann model (Eq. (4.8)) for the hard sphere system.

and the electrolyte concentration is increased, the relaxation time decreases from 5×10^3 s to 5×10^{-3} s (see Fig. 4.15). The stretching parameter γ changes from 2 to 0.5 when the salt amount increases from 10 μM to 500 μM and reaches 0.8 for the highest salt amount of 1000 μM (see Fig. 4.16).

Samples without salt and with volume fractions $\phi > 0.19$ show extremely slow dynamics with very long relaxation times $\tau > 10^3$ s. This suggests an arrested type dynamics when the motion of the colloidal particles is restricted by neighboring particles interacting with each other [16]. Such non-diffusive dynamical behavior has been previously observed for glass forming fluids when the system approaches the glass transition [67, 109–111, 125]. The observed dynamical behavior of PA particles with $\phi > 0.19$ is in agreement with expectations from the phase diagram of charge-stabilized colloidal particles (see Table 3.2), which suggests that the samples are in a glassy state. The values of the stretching parameter γ are close to 2 (see Fig. 4.16) indicating a compressed exponential behavior of the $g^{(2)}$ functions (see Fig. 4.13) at these volume fractions. Such values of γ are also typical of the glass phase [67, 125, 134].

With decreasing volume fraction the dynamics of PA particles become faster. At the same time the stretching parameter γ changes from the compressed region ($\gamma > 1$) to the stretched region ($\gamma < 1$) at low volume fraction. This suggests that the dynami-

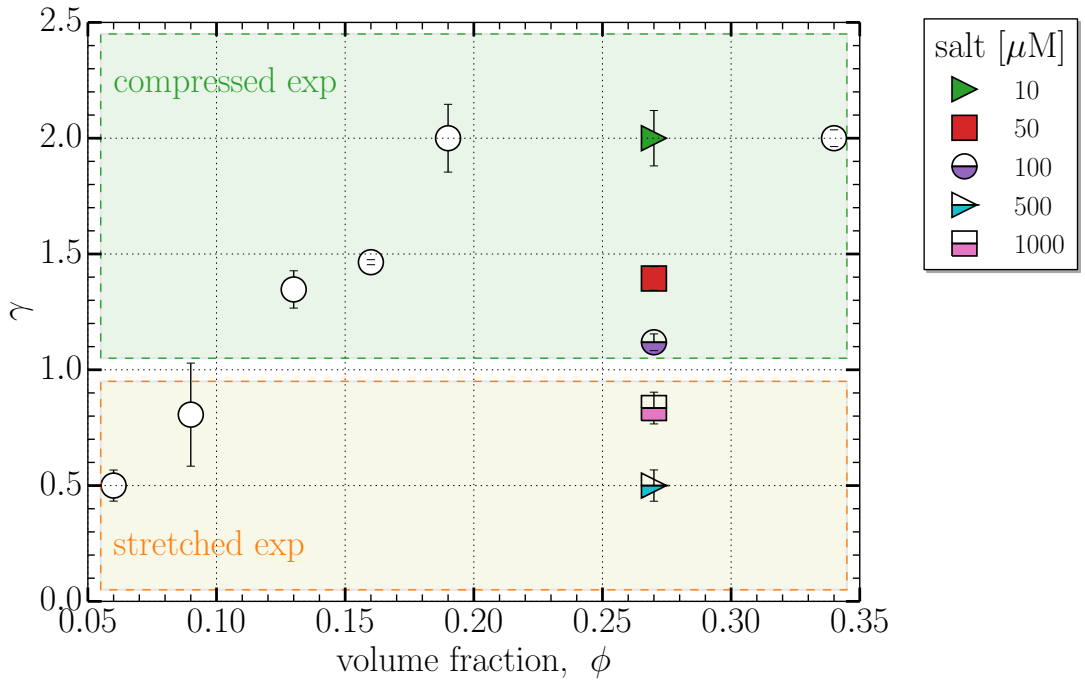

Figure 4.16: The stretching parameter γ as a function of sample's volume fraction ϕ and electrolyte concentration (see legend). Values of parameter γ were obtained from the fits of autocorrelation functions $g_{nj}^{(2)}$ (see Fig. 4.13 and Fig. 4.14) with Eq. (4.7). Green and yellow rectangles show the regions where the autocorrelation function $g_{nj}^{(2)}$ has a compressed and stretched exponential shape, respectively.

cal behavior of the system changes from non-diffusive to the sub-diffusive regime (see section 2.6.3). A decrease of relaxation time τ at low volume fractions is expected since the particles have more free volume to move within a sample. Similar dynamical changes following the increasing particle concentration have been found for hard sphere systems [67] at volume fractions in the region of $0.49 < \phi < 0.58$ when the system approaches the glassy state (see hard sphere phase diagram in Fig. 1.3).

The dependence of the relaxation time τ on the volume fraction for hard spheres is often described by the Vogel-Fulcher-Tammann (VFT) model [67, 222, 223]

$$\tau(\phi) = \tau_0 e^{D/(\phi_0 - \phi)} \,. \tag{4.8}$$

where τ_0 is a scaling parameter, D is the fragility index [223, 224]. Parameter ϕ_0 is the VFT glass transition volume fraction which for hard spheres varies between $0.56-0.62$ [67, 223, 224]. The relaxation time for hard spheres calculated by eq. (4.8) with parameters taken from [67][5] is presented in Fig. 4.15. The hard sphere system shows much faster dynamics in comparison to the PA particles at the same volume fractions. However, for the sample with volume fraction $\phi = 0.27$ when electrolyte concentration

[5] $\tau_0 = 0.007$ s, $\phi_0 = 0.56$, $D = D_0\phi_0$ with $D_0 = 0.35$.

increases the dynamics of the system become faster. At the highest electrolyte concentration (1000 μM) the relaxation time τ is close to the hard sphere case. In high concentrations electrolyte screens the interaction and the mobility of the particles increases [41]. Based on the observed γ values at different electrolyte concentrations it can be concluded that the system of PA-particles experienced different diffusive regimes. The stretching parameter γ decreases to 0.5 at a salt concentration of 500 μM, mirroring the behavior of the sample at decreasing volume fractions. The values of $\gamma < 1$ were generally observed for systems in the supercooled regime [94, 97]. Combination of intermediate relaxation times of 1 s with such values of stretching parameters may be interpreted as a result of coexistence of several dynamical regimes. The increase of salt concentration to 1000 μM brings the system to a free diffusive regime with relaxation time τ around 0.005 s and γ closer to 1. The values of relaxation time and stretching parameter are consistent with liquid state of the sample as suggested in Table 3.2. Within the VFT model with glass transition volume fraction $\phi_0 = 0.27$ the dynamics of PA particles is well described for volume fractions $\phi < 0.19$, however the model becomes inaccurate close to the transition to the glassy state ($\phi > 0.19$). The model does not describe the system behavior in the glass region, similar to hard sphere systems [67, 222].

4.4 Spatial correlation analysis

In the following section the experimental approach and the results of the XCCA are presented. First, the principal steps of the XCCA algorithm are laid out in section 4.4.1. The analysis results for PA colloidal samples at different particle and electrolyte concentrations are discussed further in section 4.4.2.

4.4.1 Data analysis procedure

Measurements were performed according to the scheme described in section 3.2.2. For the analysis the first two scattering patterns at each sample position were added together for better signal statistics. The summation is possible since the sample relaxation time $\tau = 1561$ s is much bigger than the time between two shots and the sample can be considered static. However, more scattering patterns cannot be summed because of radiation damage. An example of such a pattern from one position of sample PA-4 with volume fraction $\phi = 0.19$ is shown in Fig. 4.17.

The data was interpolated to polar coordinates with radial coordinate q and polar angle φ with 365 and 1621 steps, respectively. This grid is chosen so that the step size at the highest q is equal to the pixel size. The interpolated intensity as a function of q

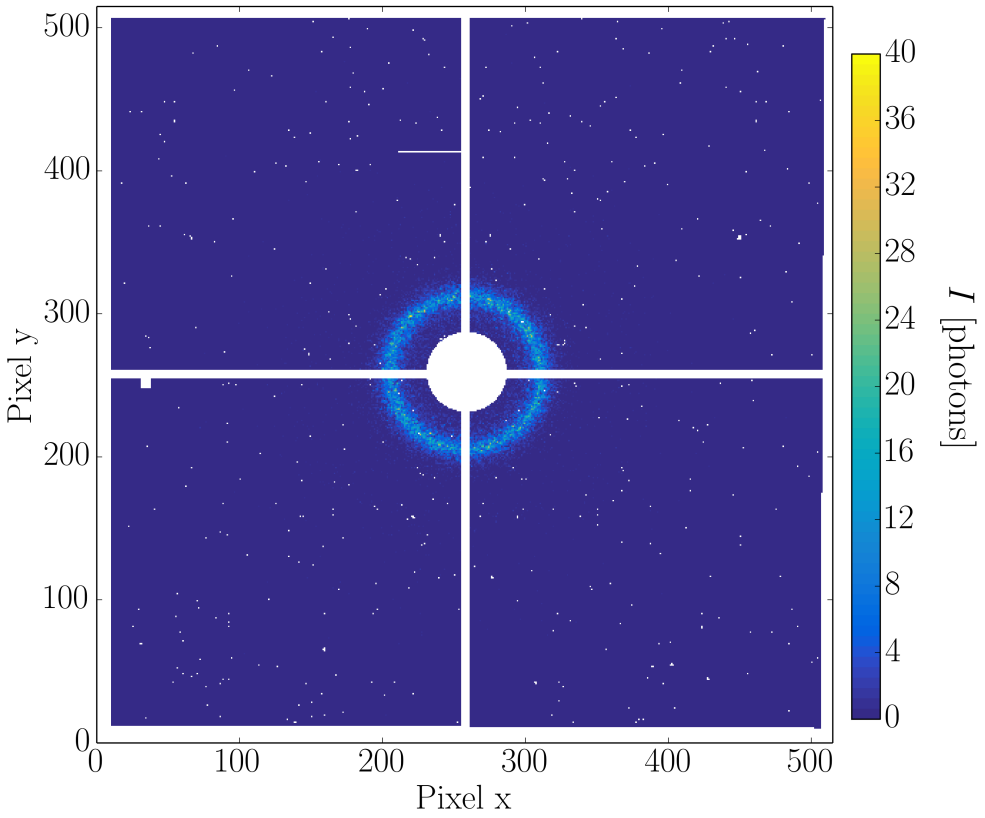

Figure 4.17: Sum of 2 speckle patterns taken at one sample position. Here, the sample is PA-4 with volume fraction $\phi = 0.19$. White color areas show region of masked pixels.

and φ is shown in Fig. 4.18. The q region for XCCA was chosen between 0.0015 Å^{-1} and 0.009 Å^{-1}. The maximum value on the colorscale for speckle patterns in Fig. 4.17 and Fig. 4.18 is different. The intensities on the speckle pattern have slightly different values after interpolation (see Fig. 4.18) in comparison to initial ones (see Fig. 4.17). This change is typical for the interpolation procedure – the neighboring values are effectively averaged. Nevertheless, the bright and dark speckle regions are conserved and the correlation function $C(q, \Delta\varphi)$ (see section 2.7.2) is not affected.

Calculation of angular Fourier coefficients

The standard approach for XCCA is to calculate directly $C(q, \Delta\varphi)$ according to eq. (2.54) [161, 173]. The expansion of the $C(q, \Delta\varphi)$ into a Fourier series (see eq. (2.55)) allows to extract the Fourier coefficients $C_l(q)$ reflecting the local orientational order [173].

In this work a mathematically equivalent approach to the traditional one for the calculation of Fourier coefficient $C_l(q)$ was explored. The method is based on the connection between coefficient $C_l(q)$ and the angular normalized intensity Fourier coefficient $\tilde{I}_l(q)$ (see eq. (2.58)). This connection can be utilized to

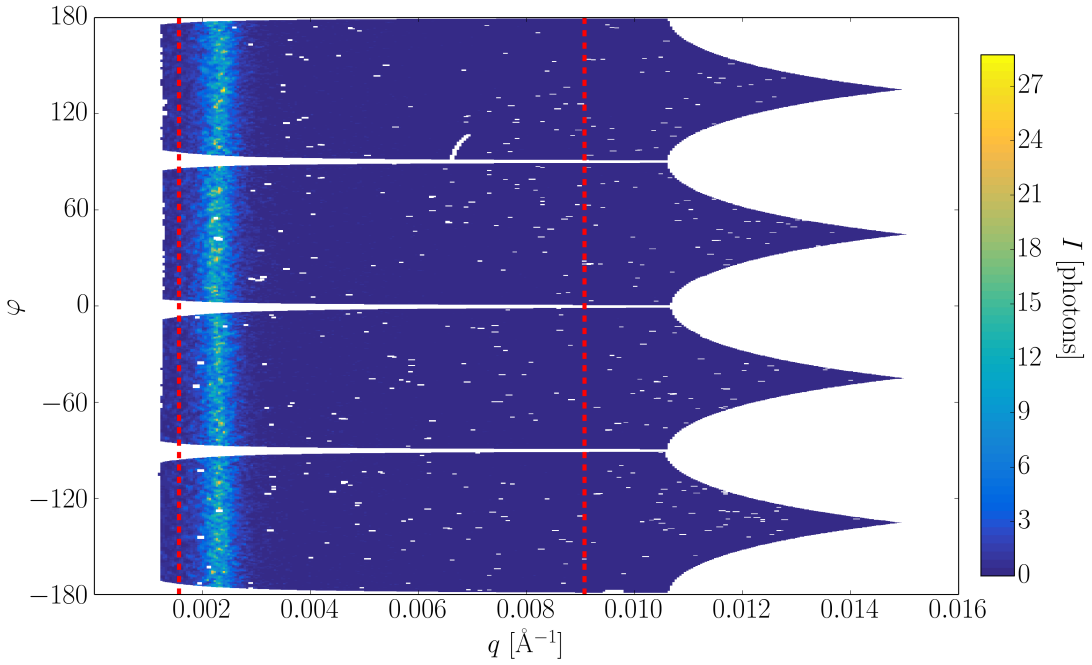

Figure 4.18: Scattered intensity data interpolated to polar coordinates. Red lines show ROI for XCCA of 0.0015 Å$^{-1} < q < 0.009$ Å^{-1}. The sample is PA-4 with volume fraction $\phi = 0.19$.

reduce computational time. In order to obtain the Fourier coefficients $\tilde{I}_l(q)$ the angular dependence of intensity $I_(q, \varphi)$ at each q is expanded into a Fourier series. This method is impeded by the gaps in the data due to masking. The gaps may obscure the values of some Fourier coefficients. To overcome this limitation the gaps were filled with randomly chosen values from the same q-ring of non-masked ROI. The interpolated scattered intensity treated accordingly is shown in Fig. 4.19 (a). Prior to the expansion of $I(q, \varphi)$ into a Fourier series, the scattered intensity is normalized according to eq. (2.57). The obtained $\tilde{I}(q, \varphi)$ is shown in Fig. 4.19 (b) as a function of momentum transfer q and azimuthal angle φ. In $\tilde{I}(q, \varphi)$ as a function of q a modulation of magnitude is observed. The relative statistical dispersion of the $\tilde{I}(q, \varphi)$ grows with q. In Fig. 4.19 (c) two cross sections $\tilde{I}(q, \varphi)$ of Fig. 4.19 (b) at constant q positions are shown as functions of azimuthal angle φ. The relative deviation of $\tilde{I}(q, \varphi)$ from the average at the q position corresponding to the first local minimum ($q = 0.004$ Å^{-1}) of radial averaged intensity profiles $I(q)$ is 2 times larger than at the first local maximum (for sample PA-4 $q_{\text{peak}} = 0.0022$ Å^{-1}).

Ideally the normalization to the average intensity value flattens the scattering pattern. However, in the analyzed experiment numerous zero values are present in the measured intensity. Therefore, an additional step in normalization was necessary for comparison of intensity Fourier coefficients at different momentum transfers q. They were normalized by matching the standard deviation of intensity at all q positions to the one at q_{peak} for each sample. An example of obtained normalized intensities $\hat{I}(q, \varphi)$

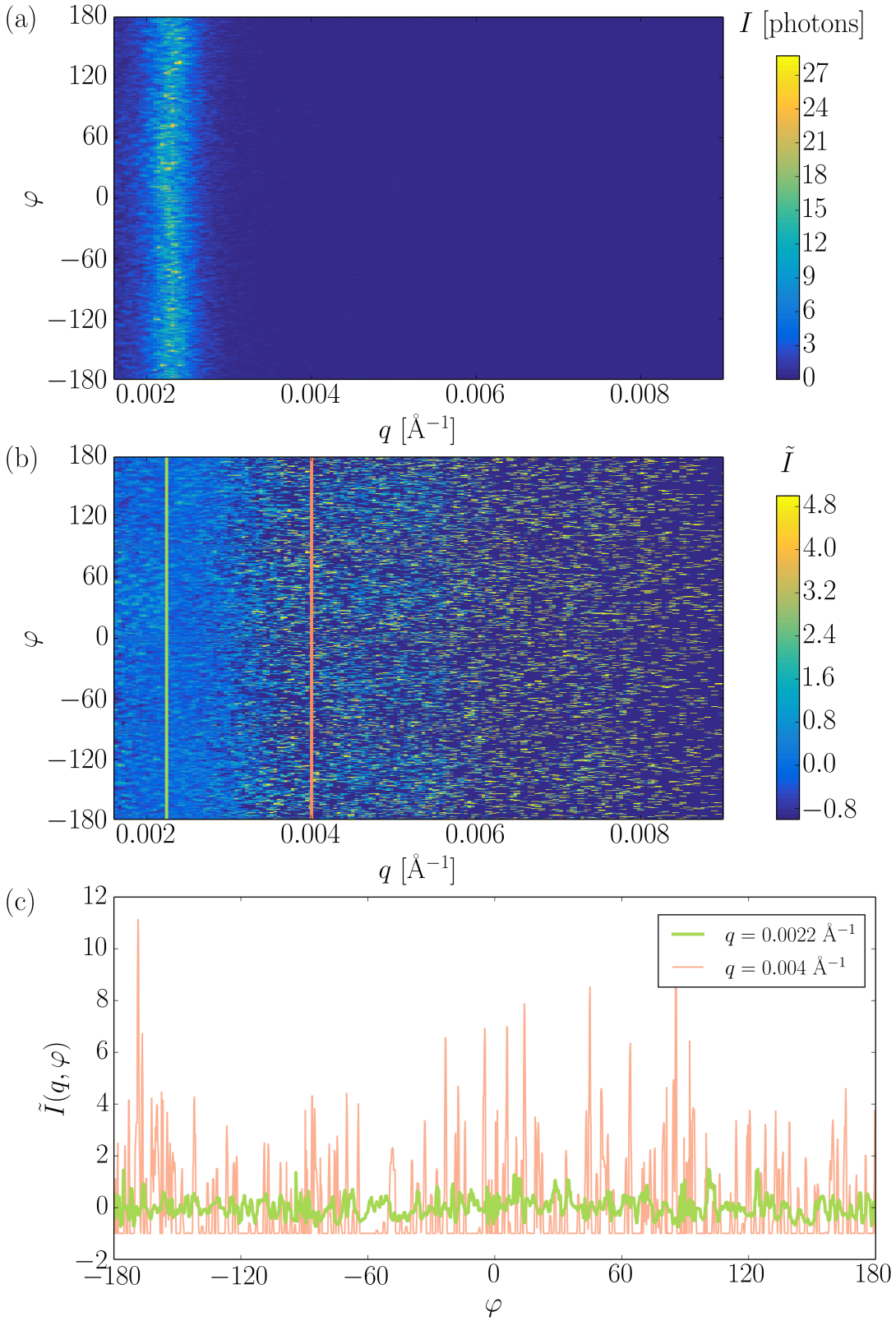

Figure 4.19: (a) Interpolated scattered intensity with assigned values for masked grid points. (b) Normalized scattered intensity $\tilde{I}(q,\varphi)$. Color scale is saturated for better visualization. (c) Normalized scattered intensity $\tilde{I}(q,\varphi)$ as a function of azimuthal angle φ at two particular momentum transfer values q (see legend). The cross section positions are indicated by green and orange lines in (b).

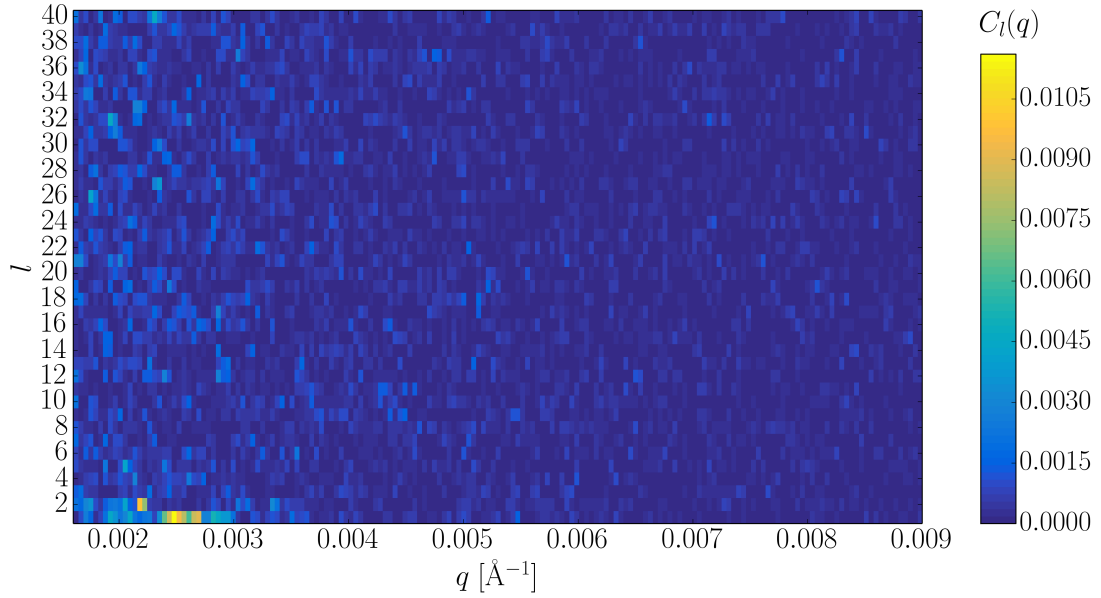

Figure 4.20: The coefficients $C_l(q)$ as function of the l-component and momentum transfer q obtained at one sample position. The sample is PA-4 with volume fraction $\phi = 0.19$.

can be found in Appendix C.

The angular Fourier coefficients $\hat{I}_l(q)$ are obtained similar to eq. (2.56). Eq. (2.58) was used to determine the coefficients $C_l(q)$ from $\hat{I}_l(q)$[6]. An example of calculated coefficients $C_l(q)$ as a function of the l-component and momentum transfer q is presented in Fig. 4.20. Typically, coefficients $C_l(q)$ show a maximum at $l = 1$. The effect is even more pronounced around the position of the structure factor maximum q_{peak}. The coefficient $C_{l=1}(q)$ corresponds to the 2π periodicity of $C(q, \Delta\varphi)$ and therefore is increased by the impact of speckle autocorrelation. The latter leads to the appearance of features at $\Delta\varphi = 2\pi N$ positions in the function $C(q, \Delta\varphi)$. It should also be considered that the Poisson noise contributes to coefficients $C_{l=1}(q)$, increasing their magnitude [195]. In addition an asymmetry of $I(q, \varphi)$ may potentially contribute to $l = 1$ coefficients [195].

Angular Fourier coefficients $C_l(q)$ calculated at one sample position do not allow a reliable extraction of local orientational order of the sample due to the low counting statistics and the presence of particle clusters with different symmetry. Therefore, it is necessary to perform ensemble averaging over many positions in the capillary.

Ensemble averaging

In colloidal systems particles may form clusters with different symmetries. These clusters can be oriented differently relative to the incoming beam. To obtain the measure of the degree of averaged local orientational order of the system, angular

[6] In Eq. (2.58) $\tilde{I}_l(q)$ is replaced by $\hat{I}_l(q)$.

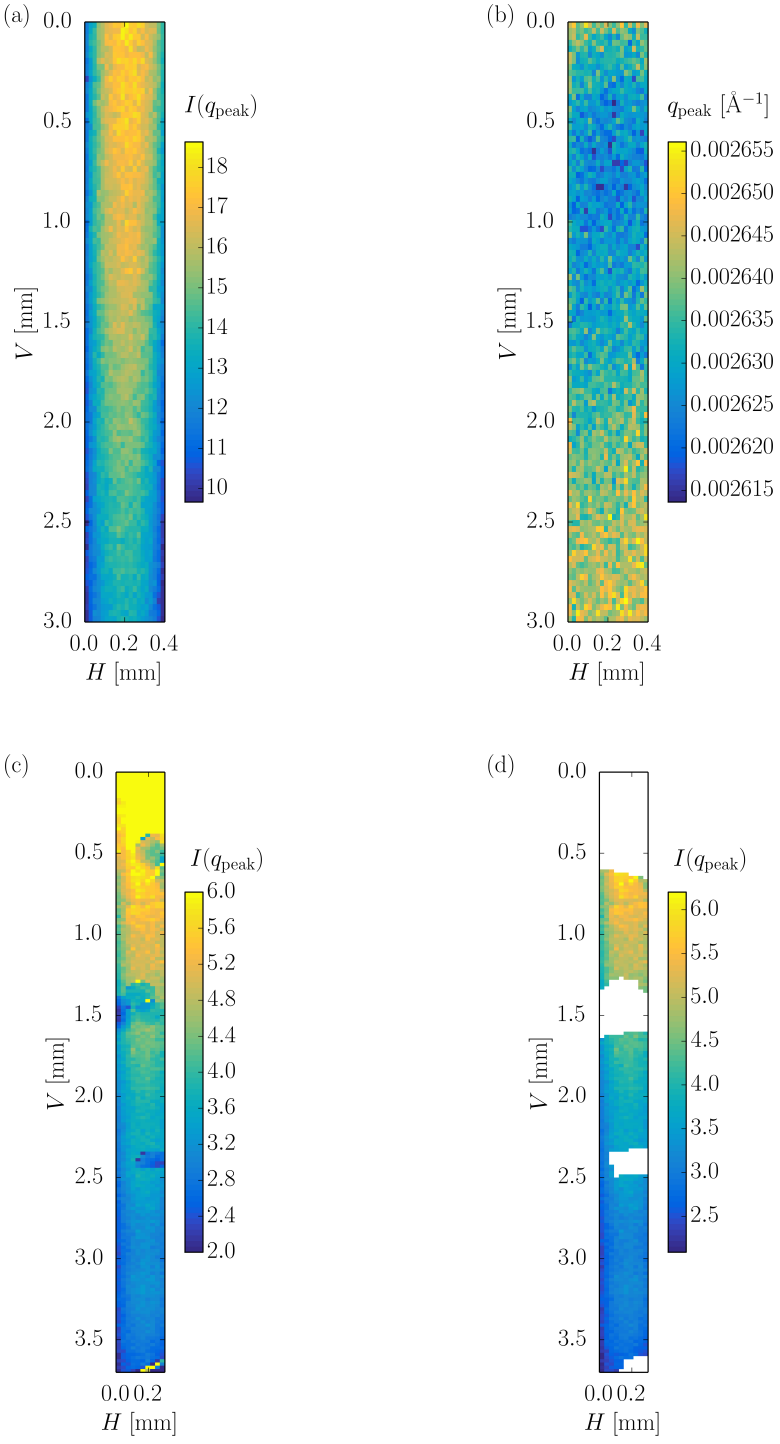

Figure 4.21: Distribution of magnitude $I(q_{\text{peak}})$ (a, c, d) and peak position q_{peak} (b) depending on the sample position. In (a) and (b) the sample is PA-1 with volume fraction $\phi = 0.34$. In (c) and (d) the sample is PA-6 with volume fraction $\phi = 0.13$. In (c) the color scale is chosen for better visibility of the regions with inhomogeneities. Panel (d) is the same as (c) with excluded inhomogeneity regions. In all plots the abscissa and ordinate axes are horizontal (H) and vertical (V) sample positions, respectively.

Fourier coefficients $C_l(q)$ were averaged over a large number of measured speckle patterns taken at different sample positions[7]. However, not all positions of the sample were used due to the presence of artifacts such as bubbles. In order to define the positions in the sample over which the coefficients $C_l(q)$ are averaged the following analysis was applied. From each two-pattern sum the angular averaged intensity $I(q)$ was obtained for every sample position. The position q_{peak} of the first intensity peak of $I(q)$ and its value $I(q_{\text{peak}})$ depending on the coordinate in the capillary were calculated. $I(q_{\text{peak}})$ and q_{peak} were obtained with a procedure similar to the one described in section 4.3.1. Examples of the distribution of $I(q_{\text{peak}})$ and q_{peak} for the sample PA-1 with volume fraction $\phi = 0.34$ are shown in Fig. 4.21 (a) and (b), respectively. In Fig. 4.21 (a) the decrease of intensity at the bottom (vertical position $V > 2$ mm) can be explained by a narrowing of the capillary. The observed peak positions q_{peak} (Fig. 4.21 (b)) do not change significantly.

In some cases inhomogeneities (e.g. bubbles) in the sample were observed (see Fig. 4.21 (c) for sample PA-6 with volume fraction $\phi = 0.13$). The inhomogeneous regions were excluded from the further analysis (see Fig. 4.21 (d)) and the remaining positions were used for ensemble averaging.

The ensemble averaged Fourier coefficients $\langle C_l(q)\rangle_e$ for sample PA-4 with volume fraction $\phi = 0.19$ are shown in Fig. 4.22 as a function of momentum transfer q and Fourier component l. Amplitudes of Fourier coefficients $\langle C_l(q)\rangle_e$ are encoded in the color scale in Fig. 4.22. In section 2.7.2 the angular Fourier coefficients obtained for a simple 2D system were studied at one particular momentum transfer $q = q_{nn}$ and the connection between real and reciprocal space symmetries was demonstrated. The Fourier coefficients $C_l(q)$ reflect a certain degree of local orientational order at the particular length scale defined by the momentum transfer q. Thus, a 2D map representation of Fourier coefficients $\langle C_l(q)\rangle_e$ presented in Fig. 4.22 reveals the dominant orientational order at different length scales. In Fig. 4.22 the l-components starting from the 4-th coefficient are shown since they reflect the symmetry properties of the sample. The Fourier coefficients $C_{l=1}(q)$ do not provide information about symmetry of local structures and their high magnitudes were already discussed above. The second coefficient $C_{l=2}(q)$ reflects the periodicity $2\pi/2$ of the diffraction pattern. Due to Friedel's rule $I(-\mathbf{q}) = I(\mathbf{q})$ the coefficient $C_{l=2}(q)$ does not represent meaningful structural information and is omitted in Fig. 4.22 and following results for better visualization. Friedel's rule in principle means that only even l-components would be present in an ideal case, however, odd l-components may also be non-zero due to e.g. noise contribution and non-planar X-ray wavefronts [166, 186].

[7] Ensemble averaging also helps to overcome insufficient counting statistics.

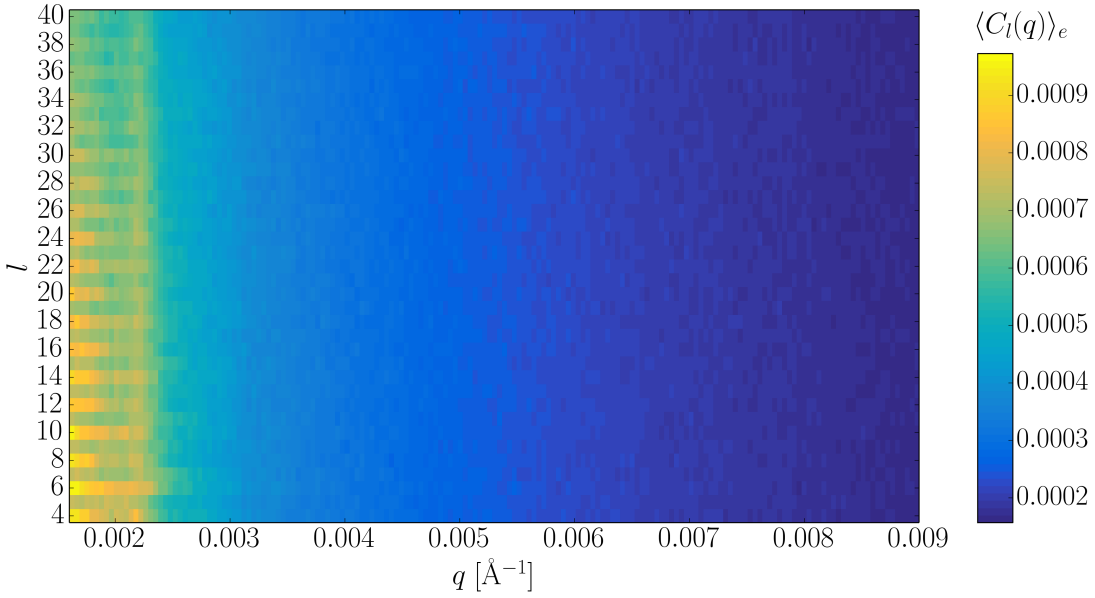

Figure 4.22: Ensemble averaged coefficients $\langle C_l(q)\rangle_e$ as a function of l-component and momentum transfer q for sample PA-4 with volume fraction $\phi = 0.19$.

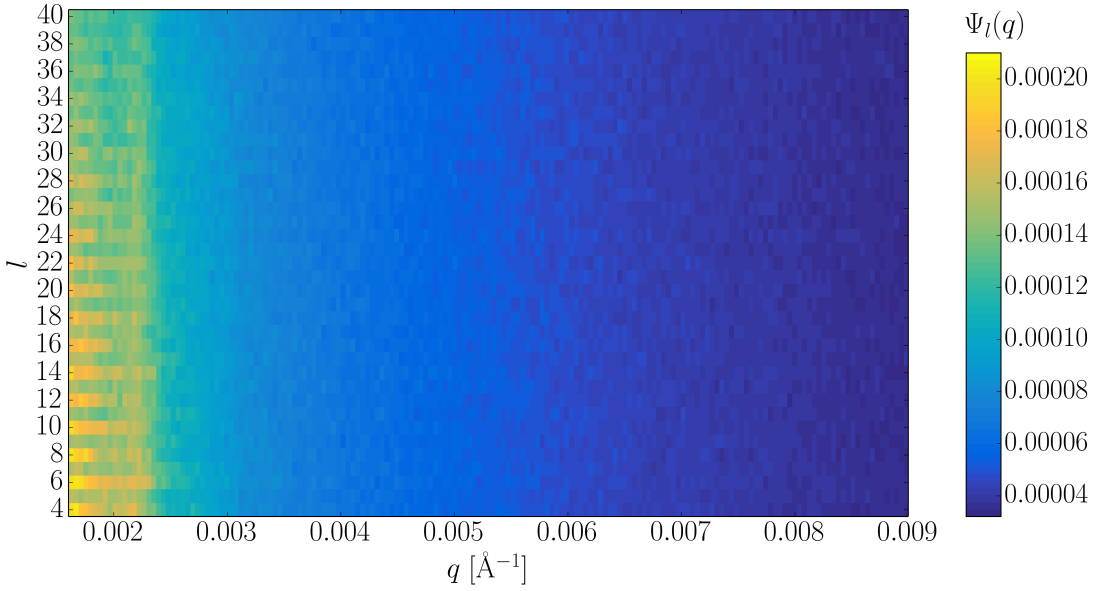

Figure 4.23: $\Psi_l(q)$ coefficient as a function of component l and momentum transfer q for sample PA-4 with volume fraction $\phi = 0.19$.

The amplitudes of the Fourier coefficients $\langle C_l(q)\rangle_e$ generally show variations at momentum transfers below and around the first intensity peak q_{peak}. At larger q the coefficients continuously decrease and do not display any dependence on the l-component in the latter region.

Note that the additional flattening normalization described above in section 4.4.1 does not significantly affect the values of Fourier coefficients $\langle C_l(q)\rangle_e$ below and around q_{peak}. The comparison of Fourier coefficients obtained with and without this normalization can be found in Appendix C.

In section 2.7.2 the variance $\Psi_l(q)$ was introduced by eq. (2.59) following [67, 166]. In Fig. 4.23 the coefficients $\Psi_l(q)$ are shown as a function of l-component and momentum transfer q. Comparison of coefficients $\Psi_l(q)$ (Fig. 4.23) and $\langle C_l(q)\rangle_e$ (Fig. 4.22) does not show noticeable differences in the component distribution. However, in the following the coefficients $\Psi_l(q)$ will be used in order to compare results to a similar XCCA study on 3D colloidal hard sphere system [67, 166, 186, 190].

4.4.2 Local orientational order in PA samples

XCCA results

The procedure specified above was applied to the samples at volume fractions $0.13 \leq \phi \leq 0.34$ and electrolyte concentrations from 0 to 500 μM. The results of the analysis are presented in the following.

In Fig. 4.24 2D maps of coefficients $\Psi_l(q)$ as a function of momentum transfer q and component l are shown for samples PA-1 ($\phi = 0.34$), PA-3 ($\phi = 0.25$), PA-6 ($\phi = 0.13$). A decrease of the amplitude of $\Psi_l(q)$ at momentum transfers $q > q_{\text{peak}}$ was observed for all l-components. The coefficients $\Psi_l(q)$ at $q > 0.004$ Å^{-1} are not presented – their decreasing behavior at these q is similar to sample PA-4 with volume fraction $\phi = 0.19$ discussed above (see Fig. 4.23). Even l-components in general have a higher magnitude than the neighboring odd ones. The increase of $\Psi_l(q)$ at $q < q_{\text{peak}}$ is an open question. This might be due to a technical issue in the calculation method: at smaller q the same amount of points per polar angle results in a higher number of correlation points per unit area and therefore per speckle. The coefficients $\Psi_l(q)$ have a similar order of magnitude to the hard sphere system studied in [67].

With decreasing volume fraction a peak in the amplitude of $\Psi_l(q)$ becomes more pronounced around certain q values[8]. For sample PA-1 ($\phi = 0.34$) the peak is mostly unnoticeable (see Fig. 4.24 (a)). For samples PA-3 ($\phi = 0.25$) and PA-6 ($\phi = 0.13$) the peak appeared in the ranges of 0.00233 Å$^{-1} < q < 0.00258$ Å^{-1} and

[8] Similarly, the appearance of a peak in $\Psi_l(q)$ with decreasing volume fraction has also been observed in [67].

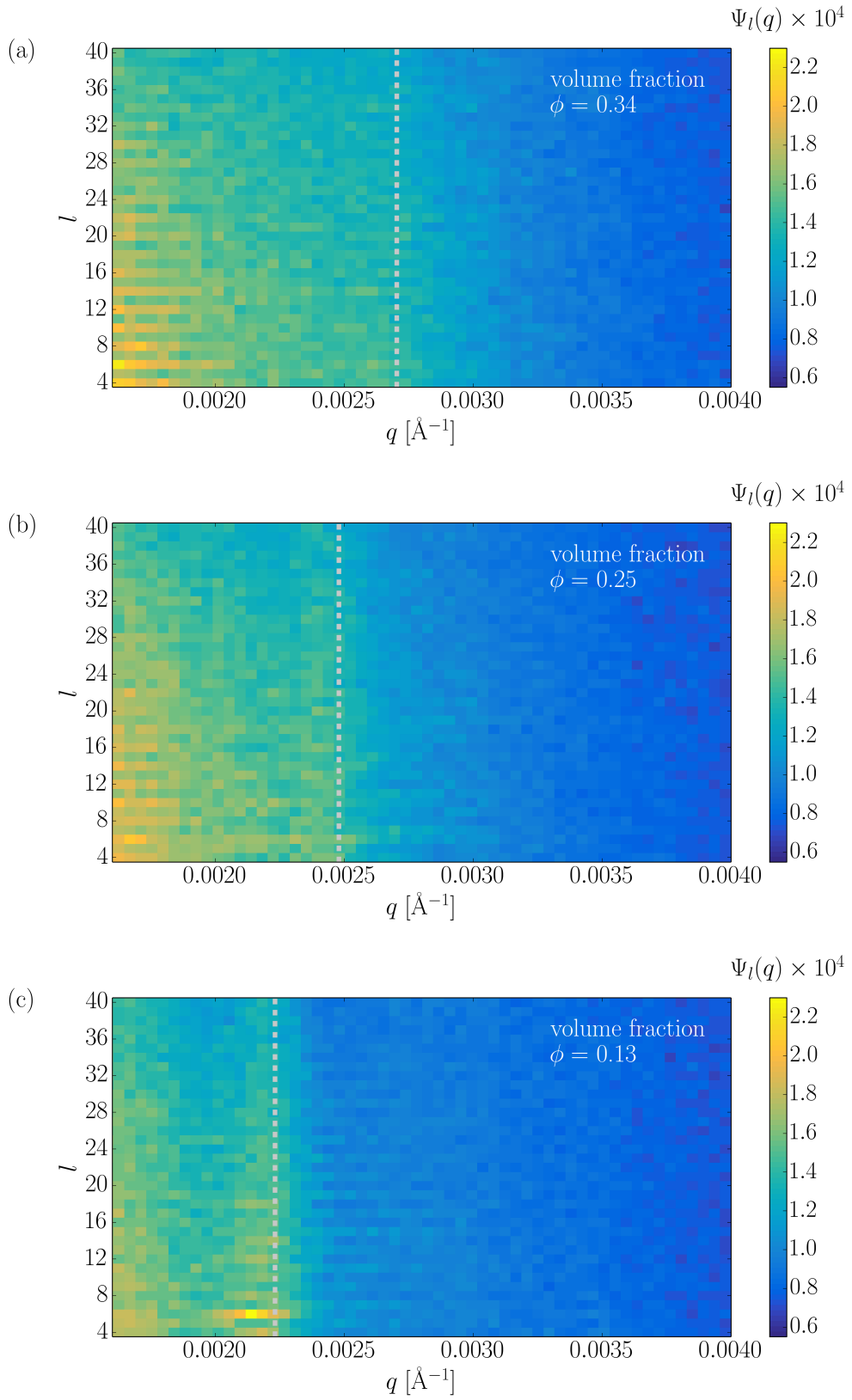

Figure 4.24: Coefficients $\Psi_l(q)$ as a function of component l and momentum transfer q for samples with volume fraction (a) 0.34, (b) 0.25, (c) 0.13. Dashed line shows the position of momentum transfer q_{peak}.

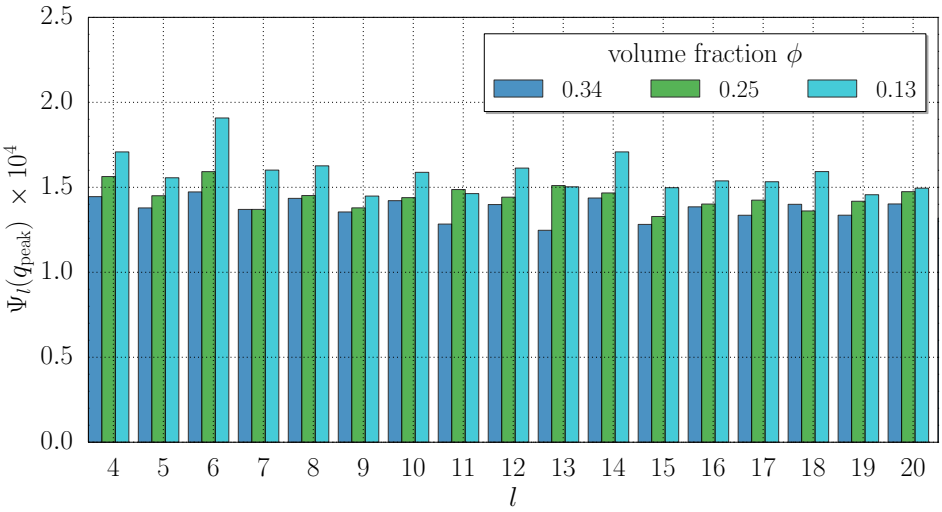

Figure 4.25: Coefficients $\Psi_l(q)$ as a function of component l for samples at different volume fractions (see legend). Coefficients were calculated at momentum transfer q_{peak} corresponding to the peak position of the structure factors $S(q)$.

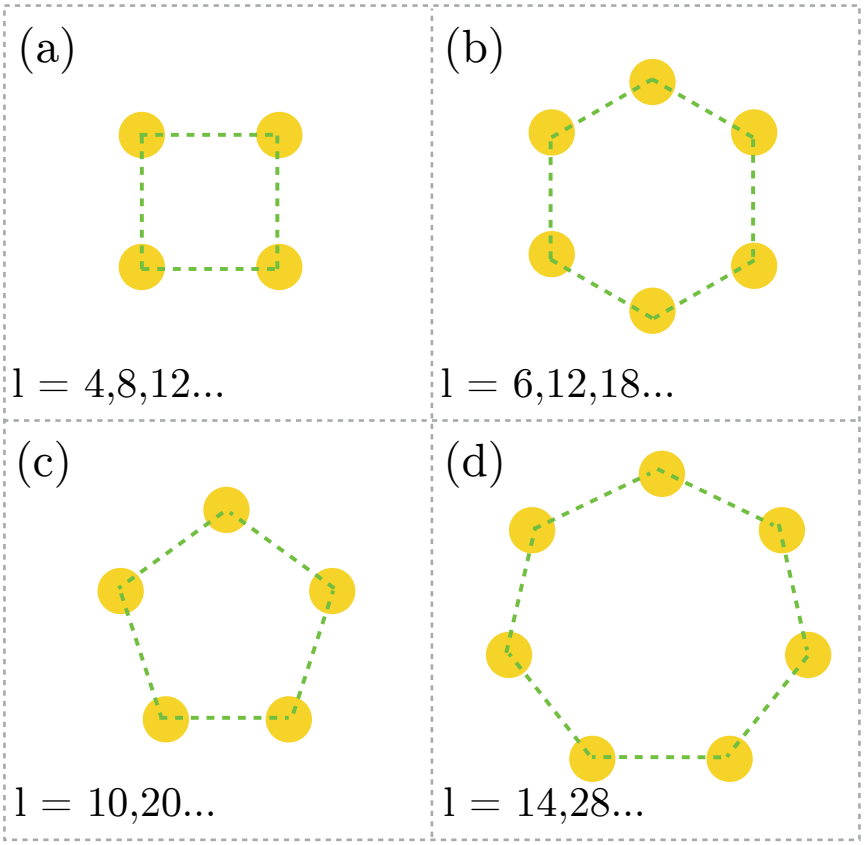

Figure 4.26: Schematic representation of the 2D projection of particles structure and its connection to dominating Fourier components in XCCA.

0.00207 Å$^{-1} < q < 0.00233$ Å^{-1}, respectively (see Fig. 4.24 (b) and (c)). These regions coincide with the position q_{peak} of the first peak of the structure factor $S(q)$ (see Fig. 4.3) in each case. The observation of the peak in $\Psi_l(q)$ coefficients at the q-positions corresponding to mean interparticle distances might suggest a certain local orientational symmetry at particular length scales.

The dependence of coefficients $\Psi_l(q)$ on l at the momentum transfer q_{peak} are shown in Fig. 4.25. For sample PA-1 with volume fraction $\phi = 0.34$ the coefficients $\Psi_l(q_{\text{peak}})$ with $l = 4, 6, 8, 10, 12, 14$ appear to dominate the others. In a 2-dimensional system these components would correspond to configurations presented in Fig. 4.26. In 3D such components might be produced by particle arrangements with similar 2D projections. A small difference between components suggests more or less equal population of all structures. With decreasing volume fraction an increase in amplitude of almost all coefficients $\Psi_l(q_{\text{peak}})$ is observed.

In particular at the volume fraction $\phi = 0.13$ (sample PA-6) the coefficient $\Psi_6(q_{\text{peak}})$ is significantly higher than the others. The arrangements with 6-fold symmetry are therefore presumably encountered more often. This suggests that hexagonal orientational symmetry is present locally in the structure at this volume fraction. This is consistent with the appearance of the peak in $\Psi_l(q)$ around q_{peak} (see Fig. 4.24).

The same analysis was applied for samples with fixed volume fraction $\phi = 0.27$ and different electrolyte concentrations varied between 0 μM and 500 μM . In Fig. 4.27 2D maps of coefficients $\Psi_l(q)$ are shown as a function of momentum transfer q and component l for three different electrolyte concentrations: 0, 100 and 500 μM. The behavior of $\Psi_l(q)$ depending on the electrolyte concentration bears some similarities to the dependence on the volume fraction. The coefficients in general decrease with momentum transfer q after the first structure factor peak position q_{peak}. The distinctive feature in $\Psi_l(q)$ at q_{peak} becomes more pronounced with increasing electrolyte concentration.

In Fig. 4.28 the dependence of coefficients $\Psi_l(q_{\text{peak}})$ on l is presented for different electrolyte concentrations. For the sample PA-2 (without salt) only a weak domination of several coefficients Ψ_l with $l = 6, 8, 12$ over the others is observed, and there is no unique dominating orientational order. A similar behavior has been noted for sample PA-1 without salt but with higher volume fraction of $\phi = 0.34$. Although the addition of salt to the PA system in general decreases magnitudes of almost all coefficients, coefficient $\Psi_{l=6}(q_{\text{peak}})$ dominates over others for sample PA-2d with electrolyte concentration of 500 μM. This means that at the q_{peak} there is a preferred local orientational order of particles for samples with higher electrolyte concentration.

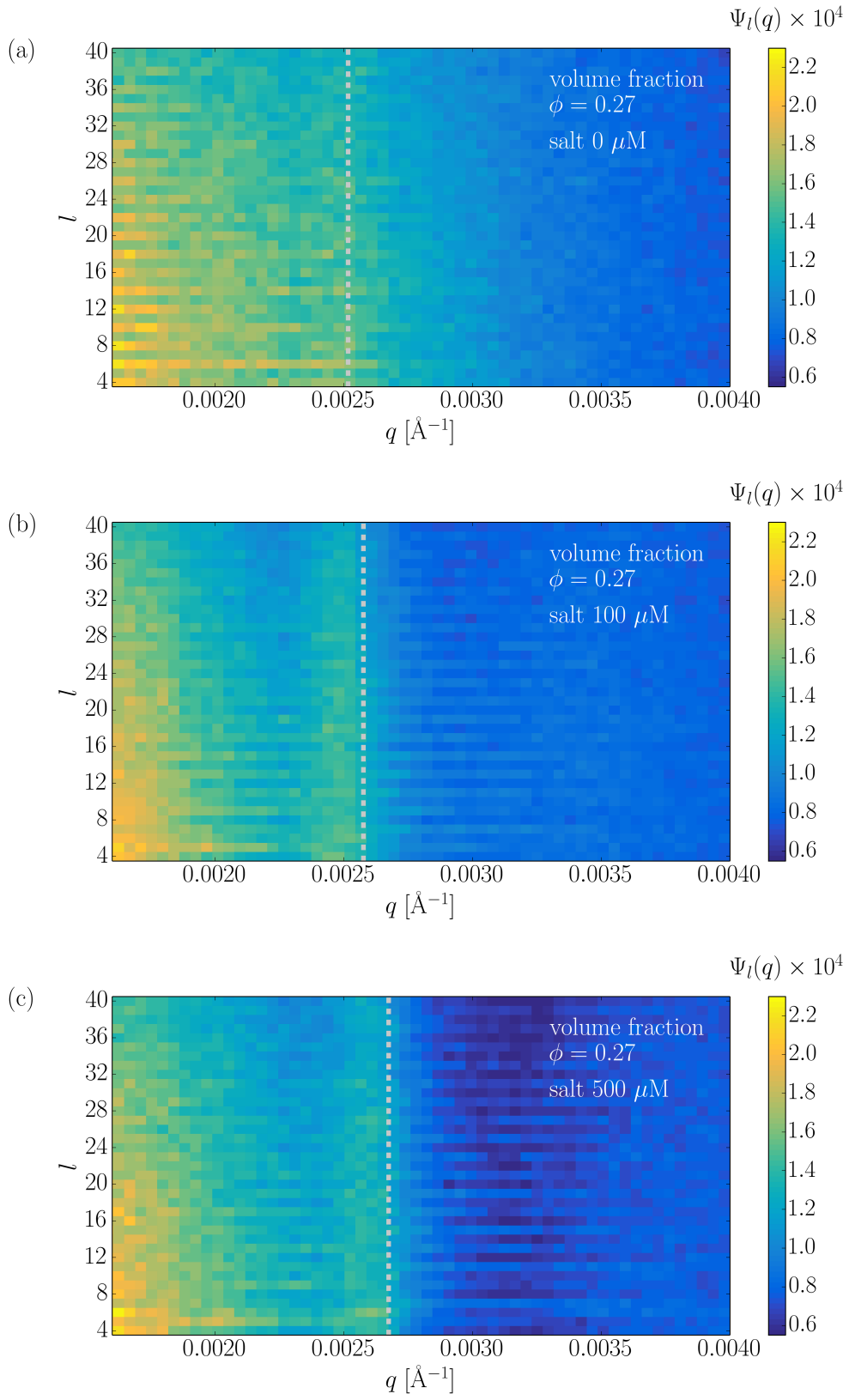

Figure 4.27: Coefficients $\Psi_l(q)$ as a function of component l and momentum transfer q for samples with volume fraction $\phi = 0.27$ and electrolyte concentration (a) 0 μM (b) 100 μM (c) 500 μM.

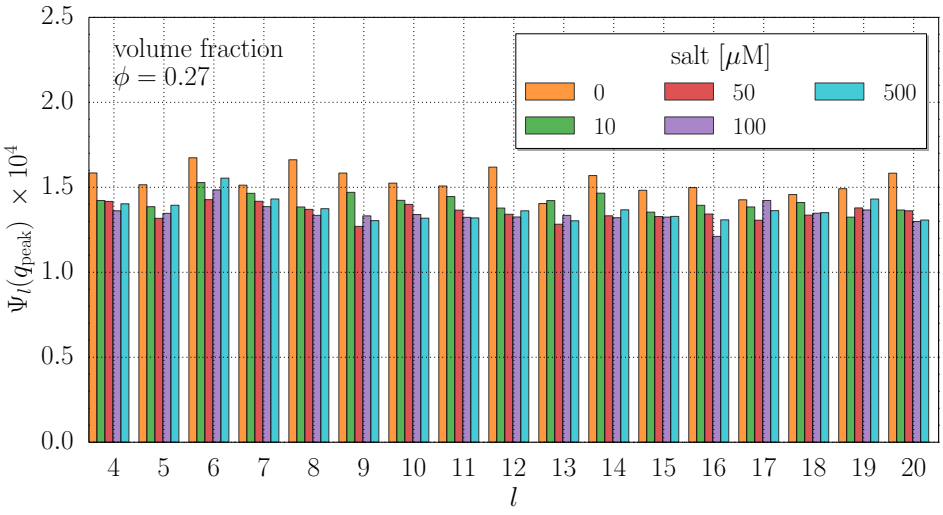

Figure 4.28: Coefficients $\Psi_l(q_{\text{peak}})$ as a function of component l for samples wiith volume fraction $\phi = 0.27$ and different electrolyte concentrations (see legend). Coefficients were calculated at momentum transfer q_{peak} corresponding to the peak position in structure factor $S(q)$.

Averaged degree of higher order correlations

In the previous section $\Psi_l(q)$ – a measure of orientational correlations with parameter l at a certain length scale q was discussed. In order to quantify the overall orientational order degree at a particular q an averaging over l-components was performed[9]. The resulting averaged functions $\langle\Psi(q)\rangle_l$ for samples at different volume fractions and electrolyte concentrations are shown in Fig. 4.29 (a) and (b), respectively. A different behavior of $\langle\Psi(q)\rangle_l$ is observed depending on the volume fraction ϕ and electrolyte concentration. At larger momentum transfers $q > 0.005$ Å^{-1} (not shown in Fig. 4.29) the amplitude of $\langle\Psi(q)\rangle_l$ continues to decrease and matches for all samples. For samples at high volume fractions $\phi = 0.34$ and $\phi = 0.27$ $\langle\Psi(q)\rangle_l$ shows a flat "shoulder" around q_{peak} (Fig. 4.29 (a)) and slowly decreases with increasing q. For samples at lower volume fractions $\phi < 0.25$ (Fig. 4.29 (a)) and for $\phi = 0.27$ with added electrolyte (Fig. 4.29 (b)), a peak is observed in $\langle\Psi(q)\rangle_l$ around the position q_{peak}. A similar behavior of $\langle\Psi(q)\rangle_l$ was observed in XCCA studies on hard-sphere samples at particle concentrations near the crystal-glass transition [67]. In the glass phase in hard-sphere systems $\Psi_l(q)$ decreases with momentum transfer q, and when the concentration is close to the crystal phase a peak appears at q_{peak}. The presence of the peak at a certain momentum transfer q indicates an increase of higher order correlations (or local orientational order) at a particular length scale. Most significant observed

[9] Averaging over the l-components was performed in [67] due to the absence of coefficient dependence on l. While this requirement is not strictly satisfied here, the averaging permits comparison of results in this thesis with [67].

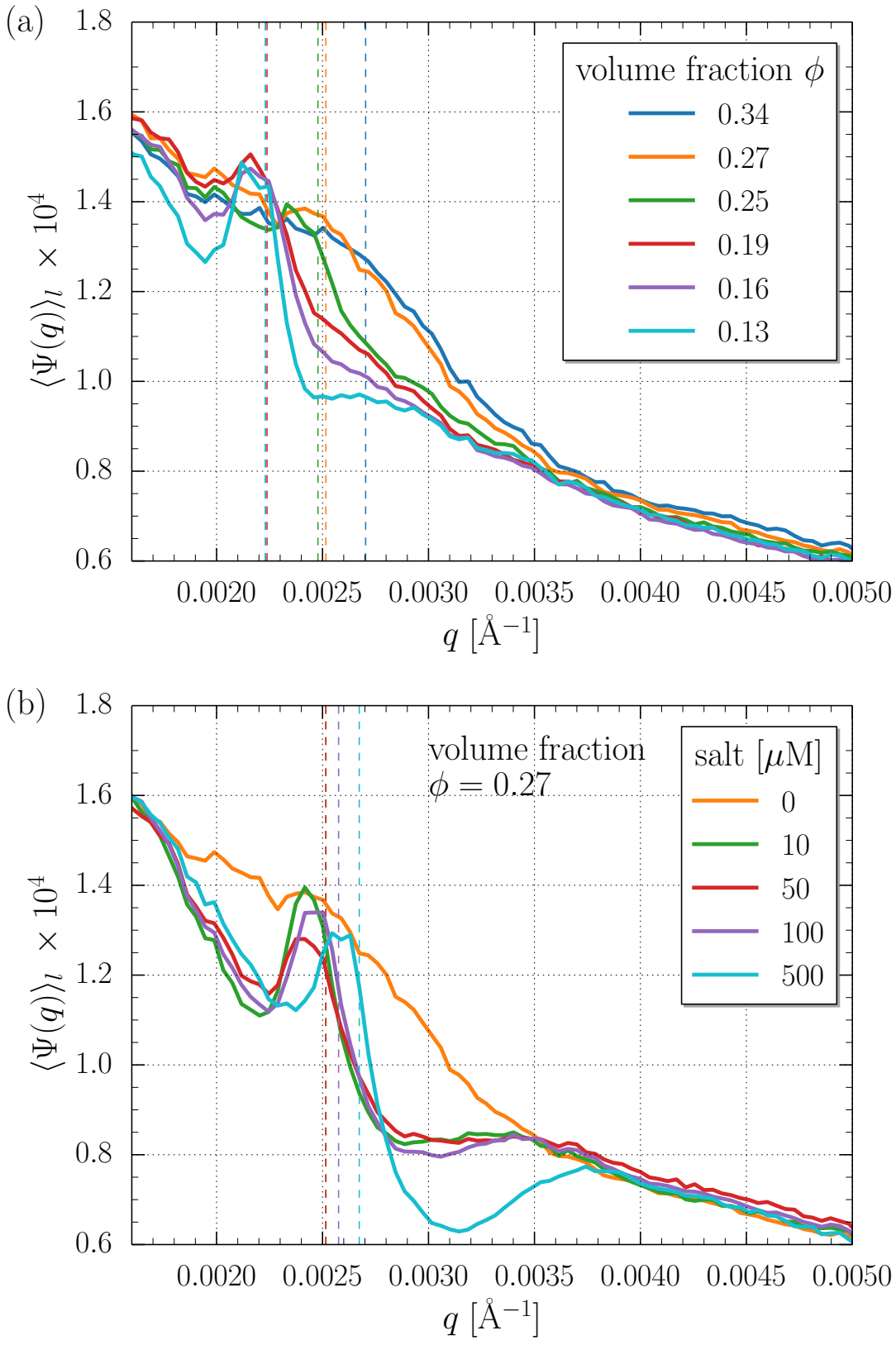

Figure 4.29: Averaged $\langle\Psi(q)\rangle_l$ as a function of momentum transfer q for samples at different volume fractions (a) and different electrolyte concentrations (b). In (b) for all samples the volume fraction $\phi = 0.27$. Dashed lines of the same color mark the position q_{peak} in $S(q)$.

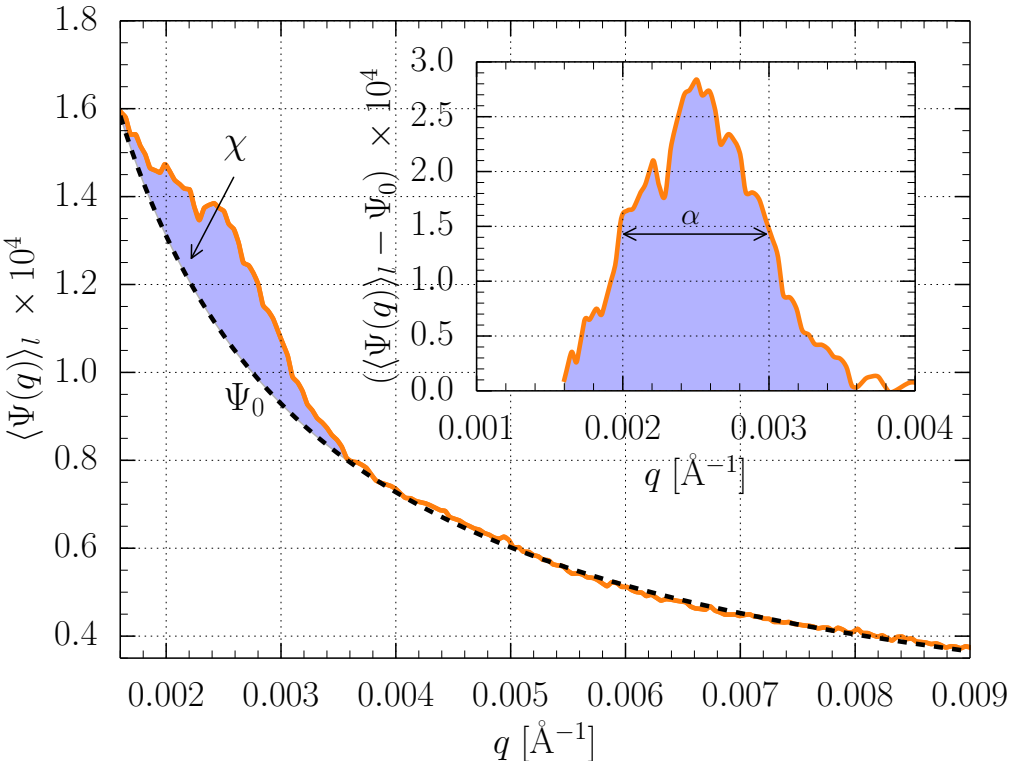

Figure 4.30: Averaged $\langle\Psi(q)\rangle_l$ as a function of momentum transfer q for the sample at $\phi = 0.27$ together with the background Ψ_0. The inset shows the subtraction of Ψ_0 from $\langle\Psi(q)\rangle_l$ as a function of momentum transfer q. Parameters χ and α are indicated.

changes in $\langle\Psi(q)\rangle_l$ for different samples are therefore in the peak width and total area under the peak. The peak width α can be used to compare the degree of local orientational order in different samples. On the other hand, the total area under the peak χ gives a total estimate for the degree of high order correlations over a range of length scales. The calculation of parameters α and χ is shown in Fig. 4.30 as an example for the sample with $\phi = 0.27$. Fig. 4.30 shows $\langle\Psi(q)\rangle_l$ together with background function ψ_0 used for calculation of parameters α and χ. A subtraction of ψ_0 from $\langle\Psi(q)\rangle_l$ as a function of momentum transfer q is shown in the inset of Fig. 4.30. In addition, the total area under the peak χ and the peak width α defined as full width at half maximum are presented.

Fig. 4.31 shows the dependencies of parameters χ and α on volume fraction ϕ (a, b) and on electrolyte concentration (c, d), respectively. The glassy region roughly determined from the phase diagram of charge stabilized colloids (see Fig. 1.4) is indicated in Fig. 4.31 by arrowbars. Both parameters describing higher order correlations (χ and α) grow up to the volume fraction of $\phi = 0.19$. In the region between $\phi = 0.19$ and $\phi = 0.25$ the peak width α continues to grow, while the integrated degree of high order correlations χ shows an almost constant behavior. A delayed growth of parame-

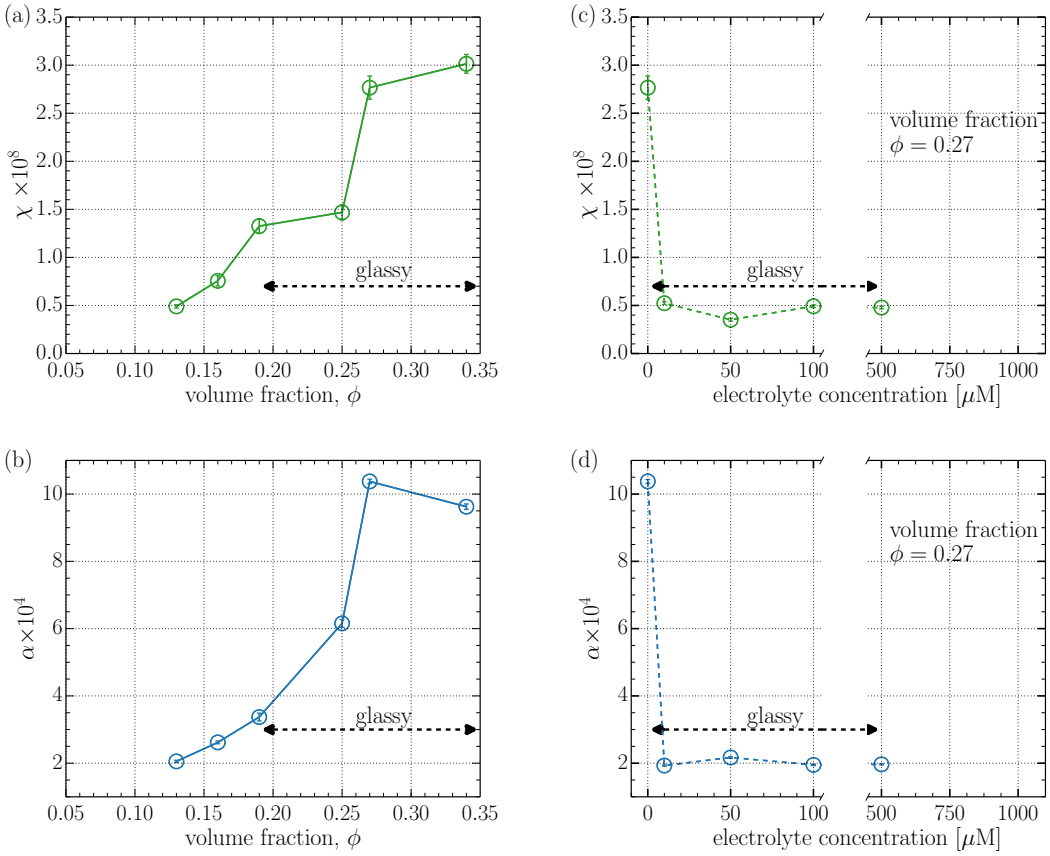

Figure 4.31: The integrated parameter χ and peak width α as a function of volume fraction ϕ (a, b) and electrolyte concentration (c, d). Arrowbar shows the glassy region roughly determined from phase diagram (see Fig. 1.4).

ter χ occurs at $\phi = 0.27$ and the parameter stays almost unchanged up to the volume fraction $\phi = 0.34$. The parameter α shows similar behavior for these volume fractions ϕ.

In the glassy phase parameter χ shows a stepwise increase in higher order correlations which are broadly distributed over length scales as suggested by the increasing peak width α. Otherwise, for lower volume fractions $\phi < 0.19$, the integrated degree of high order correlations has smaller values and its distribution is narrow since the peak width α decreases. PA samples at $\phi < 0.19$ are located in the crystal range on the phase diagram of charge stabilized particles. However, these PA samples are not crystallized, as suggested by the absence of the peaks in the averaged structure factor in comparison to study [22]. The narrowing of the peak of $\langle \Psi(q) \rangle_l$ and the observed domination of 6-component of $\Psi_6(q_{\text{peak}})$ for $\phi = 0.13$ (see Fig. 4.25) might suggest a formation of crystal precursors in the system.

When the volume fraction is kept constant ($\phi = 0.27$) and electrolyte concentration is increased the parameters χ and α show similar behavior (see Fig. 4.31 (c,d)). Even a small electrolyte amount causes a dramatic decrease in the degree of higher

order correlation χ and narrowing of length scale α over which these correlations are distributed. The χ and α for samples with salt have similar values to the case of $\phi = 0.13$.

In the next section the high order correlations of the samples will be compared to observed pair correlations and both will be discussed in parallel with sample dynamics.

4.5 Discussion of structural and dynamical results

In this section the structural results obtained in sections 4.2 and 4.4.1 are discussed together with the dynamical results obtained in section 4.3. In order to summarize the structural and dynamical properties of PA samples, the order parameter $S(q_{\mathrm{peak}})$ with position q_{peak}, the relaxation time τ and the orientational order parameter χ are shown in Fig. 4.32. On the left-hand side of the figures (see Fig. 4.32 (a,b,c)) the dependencies of these parameters on the volume fraction ϕ are presented. On the right side (see Fig. 4.32 (d,e,f)) the parameters $S(q_{\mathrm{peak}})$, q_{peak}, τ, χ are shown as a function of electrolyte concentration for samples at a fixed volume fraction of $\phi = 0.27$. The ordinate axes have the same scale limits on the left and on the right for easier comparison. In Fig. 4.32 (b) and (e) the relaxation time τ for samples at $\phi = 0.25$ and $\phi = 0.27$ is shown by a vertical dashed line since τ for these samples could only be estimated to be larger than 500 s. The arrowbars show the glass region that has been roughly determined from the phase diagram of charge stabilized particles (see Fig. 1.4). In the glassy state one finds the samples at high volume fractions ($\phi > 0.19$) and for $\phi = 0.27$ at electrolyte concentrations up to 500 μM. For the other samples the phase diagram suggests a crystalline state (see Fig. 1.4). The crystal phase, however, was not observed during the experiment, although PA samples crystallized within two months after the experiment. Therefore, samples that do not fall under the glassy state region of the phase diagram are considered to be in a metastable liquid state.

Consider now the sample series at different volume fractions (Fig. 4.32 (a,b,c)). The amplitude of the structure factor $S(q_{\mathrm{peak}})$ and its position q_{peak} (Fig. 4.32 (a)), and the relaxation time τ (Fig. 4.32 (b)) behave similarly when the volume fraction is increased. Two different regimes can be observed below and above the volume fraction $\phi = 0.19$. In the first regime (when $\phi < 0.19$) the amplitude of $S(q_{\mathrm{peak}})$ as well as relaxation time τ both increase. The increasing degree of pair correlations accompanied by slowdown of sample's dynamics as a result of increasing particle concentration has been previously observed in [41, 89, 98, 108]. In the second regime ($\phi > 0.19$), corresponding to the glassy phase, the amplitude of the structure factor $S(q_{\mathrm{peak}})$ stays

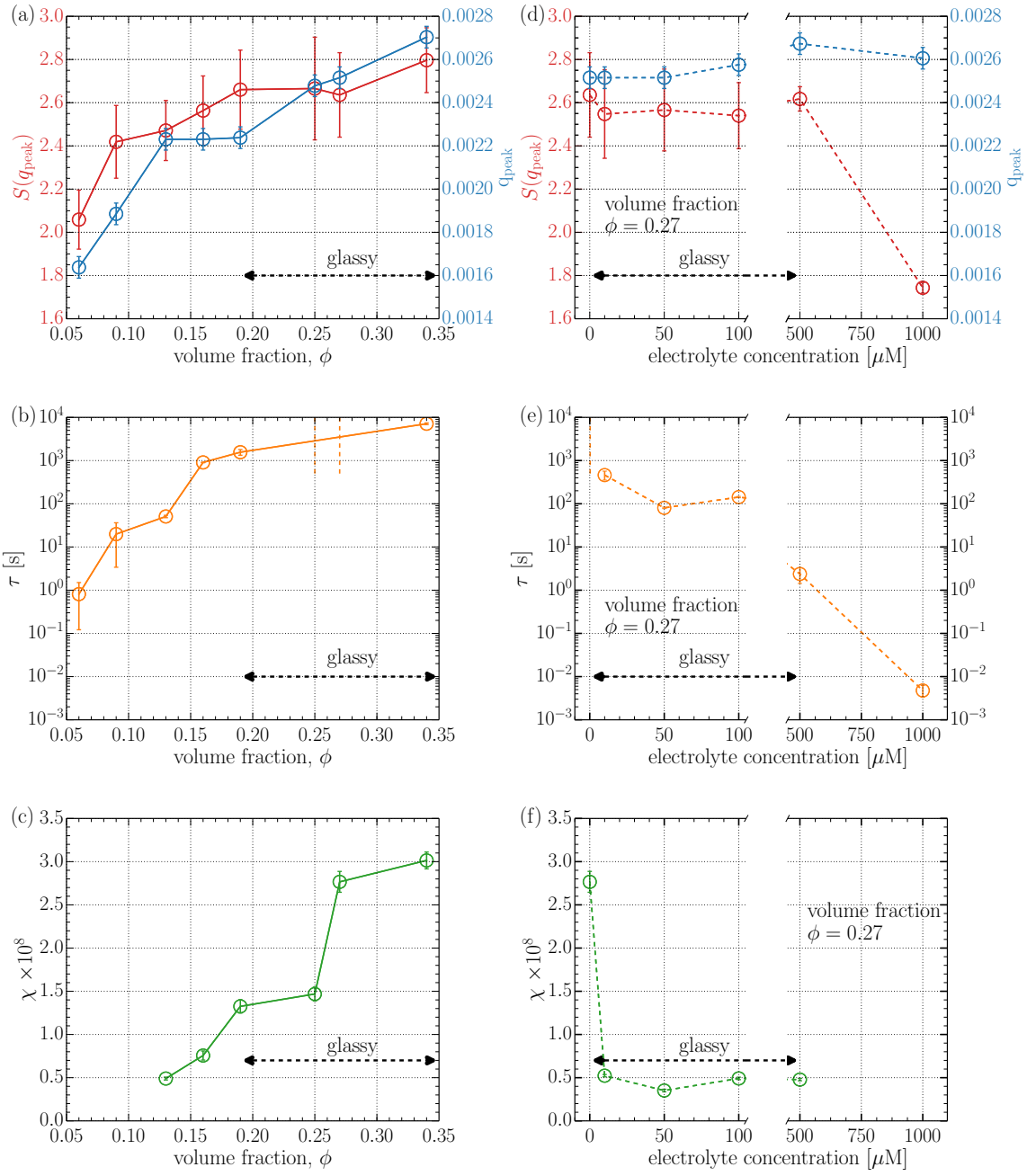

Figure 4.32: Structural and dynamical parameters. (a) Amplitude of the structure factor peak $S(q_{\text{peak}})$ and its position q_{peak}, (b) relaxation time τ and (c) degree of high order correlations as a function of volume fraction. (d) Amplitude of the structure factor peak $S(q_{\text{peak}})$ and its position q_{peak}, (e) relaxation time τ and (f) degree of high order correlations as a function of electrolyte concentration. The glassy region roughly determined from phase diagram (see Fig. 1.4) is shown by arrowbar.

almost constant. The growth rate of relaxation time τ decreases significantly, and τ reaches closer to saturation. Consider now the behavior of orientational order parameter χ (Fig. 4.32 (c)). In the first region ($\phi < 0.19$) the χ parameter increases, similarly to the behavior of $S(q_{\mathrm{peak}})$ and τ. However, upon reaching the glassy phase parameter χ demonstrates a change in behavior. Above $\phi = 0.19$ the parameter χ stagnates up to a volume fraction of $\phi = 0.25$. However, a strong increase is observed above $\phi = 0.25$. Such behavior can be explained by a delayed development of angular ordering upon entry the glassy phase. Consider the behavior of χ starting from the highest volume fraction $\phi = 0.34$ – from the glassy region. In contrast to the almost constant behavior of $S(q_{\mathrm{peak}})$, the parameter χ decreases already at concentration of $\phi = 0.27$ which is still in the glass region.

If the volume fraction is kept constant ($\phi = 0.27$) and the electrolyte concentration is increased, the PA samples change from the glass state into the metastable liquid. Similar to the experiment with changing volume fractions, the dependence of $S(q_{\mathrm{peak}})$ on electrolyte concentration shows a similar trend to the dependence of τ (see Fig. 4.32 (d,e)). The relaxation time τ decreases upon addition of salt because of the increasing charge screening on the particle surface. The interparticle interaction between charge-screened particles becomes weaker and particles become more mobile. In the glass region (electrolyte concentrations up to 500 μM) the amplitude of the structure factor peak $S(q_{\mathrm{peak}})$ is almost unchanged. In contrast, the parameter χ decreases already at lower electrolyte concentrations of about 10 μM (see Fig. 4.32 (f)) and stays almost constant upon addition of salt. The magnitude of the χ parameter is similar to the one observed for volume fraction $\phi = 0.13$; the same is true for the magnitude of the relaxation time τ. This supports the notion that χ and τ are correlated.

In summary, the relaxation time τ increases with increasing volume fraction ϕ. In the glassy region a slowdown of the samples's dynamics is still present but less pronounced. The pair correlation order parameter $S(q_{\mathrm{peak}})$ is mostly constant in the glassy state, while the orientational order parameter χ increases. Thus, high-order correlations grow in the glassy state. The role of higher order correlations in the system undergoing liquid-crystal transition have been reported in [225–227]. The computer simulations of hard spheres indicate that fluctuations in bond orientational order are high in fact be responsible for the transition. The analysis of the behavior of χ depending both on volume fraction and electrolyte concentration demonstrates that it is very sensitive to the structural properties of samples in the glassy state and in the vicinity of glass transition, and can therefore be considered interesting for future studies in materials undergoing a glass transitions.

SUMMARY AND OUTLOOK

This thesis is centered around an experimental investigation of the structural and dynamical properties of crystallizing and glass-forming fluids by X-ray scattering methods. The experiments were performed on colloidal dispersions, which are commonly used as model systems for studies of phase transitions. Charge stabilized polymethacrylate (PA) nanoparticles were synthesized by means of free radical emulsion polymerization. The interparticle interaction in the system was tuned by introducing different amounts of salt to the dispersion. Two sample series of PA particle dispersions with different volume fractions and electrolyte concentrations were studied in the vicinity of the glass transition. The structural and dynamical properties of the colloidal samples were investigated in experiments in Small Angle X-ray Scattering (SAXS) geometry.

First, a conventional SAXS analysis was performed. The analysis of dilute dispersions with screened particle interaction revealed a particle radius of 1200 Å and a low size polydispersity of 10%. Structure factors $S(q)$ were obtained for samples at volume fractions in the range $0.06 \leq \phi \leq 0.34$, and for samples with electrolyte concentration ranging from 0 μM up to 1000 μM at a constant volume fraction of $\phi = 0.27$. The peak position of the static structure factor q_{peak} shifted to higher momentum transfers q with increasing volume fractions, indicating shorter interparticle distances. When salt was added q_{peak} stayed almost constant – consistent with the constant volume fraction of $\phi = 0.27$. The degree of pair correlations between the particle positions within the sample was characterized by the order parameter $S(q_{\mathrm{peak}})$ – the amplitude of the structure factor peak. The pair correlations increase with the volume fraction until $\phi = 0.19$. Above $\phi = 0.19$, when the system is in the glassy state, the order parameter is almost constant. A similar constant behavior is observed at a volume fraction $\phi = 0.27$ when salt is introduced into the sample up to a concentration of 500 μM. Further increase of the electrolyte concentration (1000 μM) shows a decrease of particle ordering, which is consistent with a weakening of the particle interactions due to increasing screening by the electrolyte.

Beyond the conventional SAXS analysis, PA samples at volume fractions of $0.13 \leq \phi \leq 0.34$ and electrolyte concentrations ranging from 0 μM up to 500 μM

were investigated by means of X-ray Cross Correlation Analysis (XCCA) in order to study the local orientational order of the particles and to characterize the higher order particle correlations in the sample. Local orientational order was compared on length scales of the interparticle distances ($2\pi/q_{\mathrm{peak}}$). At high volume fractions no single dominating component of local orientational order was observed. At volume fraction $\phi = 0.13$ it was found that 6-fold symmetry was the most pronounced, indicating a prefered local hexagonal ordering in the sample structure. A less pronounced local 6-fold symmetry was also observed for a sample at a volume fraction $\phi = 0.27$ with electrolyte concentration of 500 μM. The averaged degree of higher order correlations χ grows with increasing concentration up to the volume fraction $\phi = 0.19$, similar to the pair correlation parameter $S(q_{\mathrm{peak}})$ in SAXS analysis. In the glassy state the degree of higher order correlations stays constant up to a volume fraction of $\phi = 0.25$, above which a strong increase is observed.

The dynamics of the system was studied by X-ray Photon Correlation Spectroscopy (XPCS). Different dynamical behavior was observed for PA particles depending on volume fraction and electrolyte concentration. The relaxation time varied from 1 s for the lowest volume fraction $\phi = 0.06$ up to 7000 s for the highest volume fraction $\phi = 0.34$. When the volume fraction is fixed at $\phi = 0.27$ and the electrolyte concentration is increased, the relaxation time decreases from 5000 s to 0.005 s at an electrolyte concentration of 1000 μM – similar to the samples at different volume fractions ϕ. At the highest electrolyte concentration of 1000 μM the sample dynamics can be described as free diffusion with a relaxation time $\tau = 0.005$ s.

The structural properties of the PA sample were studied in conjunction with the dynamics of the system. With increasing volume fraction up to the concentration of $\phi = 0.19$ the dynamics of the sample slow down while the degree of pair correlations and higher order correlations increases. At $\phi = 0.19$ the system approaches the glassy phase. The pair correlation order parameter $S(q_{\mathrm{peak}})$ is mostly constant in the glassy phase. Despite the absence of dominant orientational order, the integrated degree of higher order correlations over different length scales increases stepwise – i.e. a delayed angular ordering was observed upon the transition to the glassy phase.

When the particle concentration is kept constant at $\phi = 0.27$, with increasing electrolyte concentration the interparticle interactions are screened and the dynamics of the sample becomes faster in a still dense dispersion. While the degree of pair correlations stays almost unchanged up to the electrolyte concentration of 500 μM, the integrated degree of higher order correlations in the sample decreases significantly already at low electrolyte concentrations.

The combined SAXS, XCCA and XPCS study was performed for the first time on 3D charge stabilized colloidal samples at different particle and electrolyte concen-

trations. In standard SAXS experiments the structural information is averaged and no significant changes of the pair correlations $S(q)$ are observed. In contrast, XCCA revealed changes in the structural properties in the glassy phase associated with formation of higher order correlations. It is possible with XCCA to extract information on the local orientational order that is unaccessible by other X-ray scattering techniques. Such higher order structural correlations play an important role in crystallization and the glass transition, and XCCA is an appropriate tool to reveal them. However, more systematic studies are needed, such as finer steps in salt concentrations to capture more points on the phase diagram. When further developments in X-ray source and detector technology will become available [68], it will be possible to measure fast dynamics, for example at very low volume fractions. Another interesting venue of investigation would be to study the influence of parameters such as particle charge, polydispersity and particles' shape on dynamical and structural properties of the system.

APPENDIX A

The error estimation of the $g^{(2)}(q, \Delta t)$ in XPCS

The absolute error $\Delta g^{(2)}(q, \Delta t)$ of the $g^{(2)}(q, \Delta t)$ function in XPCS was calculated by

$$\Delta g^{(2)}(q, \Delta t) = \sqrt{\left(\frac{\partial g^{(2)}(q, \Delta t)}{\partial \xi}\Delta\overline{\xi}\right)^2 + \left(\frac{\partial g^{(2)}(q, \Delta t)}{\partial \eta}\Delta\overline{\eta}\right)^2}\,, \tag{A.1}$$

where $\xi = \langle I_p(t) I_p(t + \Delta t)\rangle_t$ and $\eta = \langle I_p(t)\rangle_t$. The $\Delta\overline{\xi}$ and $\Delta\overline{\eta}$ are standard errors of the mean

$$\Delta\overline{\xi} = \frac{1}{\sqrt{N_{pix}}}\frac{1}{\sqrt{N_t}}\Delta\xi\,, \tag{A.2}$$

$$\Delta\overline{\eta} = \frac{1}{\sqrt{N_{pix}}}\frac{1}{\sqrt{N_t}}\Delta\eta\,, \tag{A.3}$$

where N_{pix} and N_t are number of pixels within the ROI and total number of scattering patterns, respectively. The $\Delta\xi$ and $\Delta\eta$ are corrected standard deviation

$$\Delta\xi = \sqrt{\frac{1}{N_{pix} - 1}\sum_{i=1}^{N_{pix}}(\xi_i - \overline{\xi})^2}\,, \tag{A.4}$$

$$\Delta\eta = \sqrt{\frac{1}{N_{pix} - 1}\sum_{i=1}^{N_{pix}}(\eta_i - \overline{\eta})^2}\,. \tag{A.5}$$

APPENDIX B

Derivation of $C_l(q) = \tilde{I}_l(q)$ in XCCA

In section 2.7.2 the expression $C_l(q) = \tilde{I}_l(q)$ was postulated. Here, the derivation of this expression is presented. The cross correlation function $C(q, \Delta\varphi)$ and its Fourier coefficients $C_l(q)$ are expressed as

$$C(q, \Delta\varphi) = \frac{\langle I(q,\varphi)I(q,\varphi+\Delta\varphi)\rangle - \langle I(q,\varphi)\rangle^2}{\langle I(q,\varphi)\rangle^2} , \tag{B.1}$$

$$C_l(q) = \frac{1}{2\pi}\int_0^{2\pi} C(q,\Delta\varphi)e^{-il\Delta\varphi}\mathrm{d}\Delta\varphi . \tag{B.2}$$

Substituting eq. (B.1) in eq. (B.2), $C_l(q)$ is expressed as

$$C_l(q) = \frac{1}{2\pi}\int_0^{2\pi} \frac{\langle I(q,\varphi)I(q,\varphi+\Delta\varphi)\rangle - \langle I(q,\varphi)\rangle^2}{\langle I(q,\varphi)\rangle^2} e^{il\Delta\varphi}\mathrm{d}\Delta\varphi . \tag{B.3}$$

The brackets $\langle\rangle$ denote the averaging over azimuthal angle φ[1]

$$\langle f(\varphi)\rangle_\varphi = \frac{1}{2\pi}\int_0^{2\pi} f(\varphi)\mathrm{d}\varphi . \tag{B.4}$$

The expression $\langle I(q,\varphi)\rangle^2$ can be written in the form

$$\langle I(q,\varphi)\rangle^2 = \langle I(q,\varphi)\rangle\langle I(q,\varphi+\Delta\varphi)\rangle . \tag{B.5}$$

Adding and subtracting $\langle I(q,\varphi)\rangle\langle I(q,\varphi+\Delta\varphi)\rangle$ in eq. (B.3), and by taking into account eq. (B.4) and eq. (B.5), $C_l(q)$ takes the form

[1] In section 2.7.2 $\langle\rangle_\varphi$ was used instead of $\langle\rangle$.

$$C_l(q) = \frac{1}{2\pi}\frac{1}{\langle I(q,\varphi)\rangle^2}\int_0^{2\pi}\Big[\frac{1}{2\pi}\int_0^{2\pi} I(q,\varphi)I(q,\varphi+\Delta\varphi)\mathrm{d}\varphi + \frac{1}{2\pi}\int_0^{2\pi}\langle I(q,\varphi)\rangle\langle I(q,\varphi+\Delta\varphi)\rangle\mathrm{d}\varphi - \frac{1}{2\pi}\int_0^{2\pi}\langle I(q,\varphi)\rangle I(q,\varphi+\Delta\varphi)\mathrm{d}\varphi - \frac{1}{2\pi}\int_0^{2\pi}\langle I(q,\varphi+\Delta\varphi)\rangle I(q,\varphi)\mathrm{d}\varphi\Big]e^{il\Delta\varphi}\mathrm{d}\Delta\varphi\,. \tag{B.6}$$

In eq. (B.6) the expression in square brackets can be regrouped as

$$\Big[...\Big] = \frac{1}{2\pi}\int_0^{2\pi}\big(I(q,\varphi)-\langle I(q,\varphi)\rangle\big)\big(I(q,\varphi+\Delta\varphi)-\langle I(q,\varphi+\Delta\varphi)\rangle\big)\,. \tag{B.7}$$

By expressing the exponent in eq. (B.6) in the form

$$e^{il\Delta\varphi} = e^{il(\Delta\varphi+\varphi-\varphi)}\,, \tag{B.8}$$

and taking into account eq. (B.7), $C_l(q)$ takes the form

$$C_l(q) = \frac{1}{\langle I(q,\varphi)\rangle^2}\frac{1}{2\pi}\int_0^{2\pi}\big(I(q,\varphi)-\langle I(q,\varphi)\rangle\big)e^{-il\varphi} \cdot\Big(\frac{1}{2\pi}\int_0^{2\pi}\big(I(q,\varphi+\Delta\varphi)-\langle I(q,\varphi+\Delta\varphi)\rangle\big)e^{il(\varphi+\Delta\varphi)}\mathrm{d}\Delta\varphi\Big)\mathrm{d}\varphi\,. \tag{B.9}$$

Consider the second integral in eq. (B.9). Introducing a replacement $\varphi+\Delta\varphi=\tilde{\varphi}$, the integration limits change to φ and $2\pi+\varphi$. Due to the 2π periodicity in $I(q,\varphi)$, the φ in the integration limits can be set to 0 and the integration result will be not depend on the variable φ. Therefore integration over variables φ and $\tilde{\varphi}$ are independent, and eq. (B.9) takes the form

$$C_l(q) = \frac{1}{\langle I(q,\varphi)\rangle^2}\frac{1}{2\pi}\int_0^{2\pi}\big(I(q,\varphi)-\langle I(q,\varphi)\rangle\big)e^{-il\varphi}\mathrm{d}\varphi \cdot\frac{1}{2\pi}\int_0^{2\pi}\big(I(q,\tilde{\varphi})-\langle I(q,\tilde{\varphi})\rangle\big)e^{il\tilde{\varphi}}\mathrm{d}\tilde{\varphi}\,. \tag{B.10}$$

Considering that

$$\tilde{I}(q,\varphi) = \frac{I(q,\varphi)-\langle I(q,\varphi)\rangle}{\langle I(q,\varphi)\rangle}\,, \tag{B.11}$$

eq. (B.10) takes the form

$$C_l(q) = \frac{1}{2\pi}\int_0^{2\pi} \tilde{I}(q,\varphi)e^{-il\varphi}\mathrm{d}\varphi \cdot \frac{1}{2\pi}\int_0^{2\pi} \tilde{I}(q,\tilde{\varphi})e^{il\tilde{\varphi}}\mathrm{d}\tilde{\varphi}\ . \tag{B.12}$$

In eq. (B.12) the first integral is the Fourier coefficient $\tilde{I}_l(q)$ of normalized intensity, expressed as

$$\tilde{I}_l(q) = \frac{1}{2\pi}\int_0^{2\pi} \tilde{I}(q,\varphi)e^{-il\varphi}\mathrm{d}\varphi\ . \tag{B.13}$$

The second integral in eq. (B.12) is the conjugated coefficient $\tilde{I}_l^*(q)$. Therefore, eq. (B.10) leads to

$$C_l(q) = |\tilde{I}_l(q)|^2\ . \tag{B.14}$$

APPENDIX C

Normalization of intensities in XCCA

In section 4.4.1 an additional step of intensity normalization on a standard deviation of intensity at all momentum transfers q to the deviation at q_{peak} was introduced. Here, the resulting intensities $\tilde{I}(q,\varphi)$ and $\hat{I}(q,\varphi)$, and coefficients $\Psi_l(q)$ calculated with and without this analysis step are compared.

In Fig. C.1 scattered intensity $I(q,\varphi)$ is shown as a function of momentum transfer q and azimuthal angle φ for the sample PA-4 with volume fraction $\phi = 0.19$.

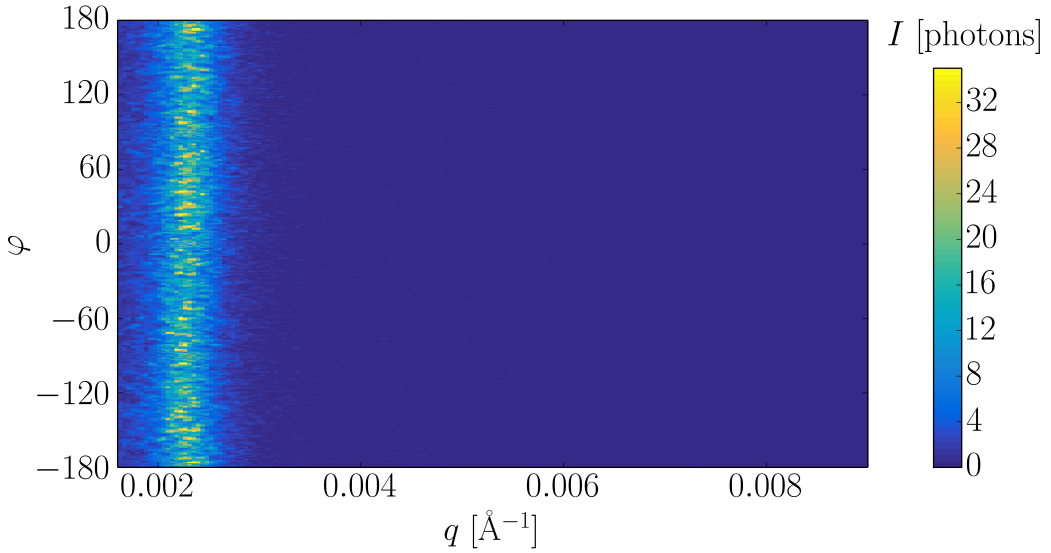

Figure C.1: Interpolated scattered intensity with assigned values for masked grid points as a function of momentum transfer q and azimuthal angle φ for sample PA-4 with $\phi = 0.19$.

Normalization of $I(q,\varphi)$ on azimuthally averaged intensity value at each momentum transfer q is performed according to

$$\tilde{I}(q,\varphi) = \frac{I(q,\varphi) - \langle I(q,\varphi)\rangle}{\langle I(q,\varphi)\rangle}\,, \tag{C.1}$$

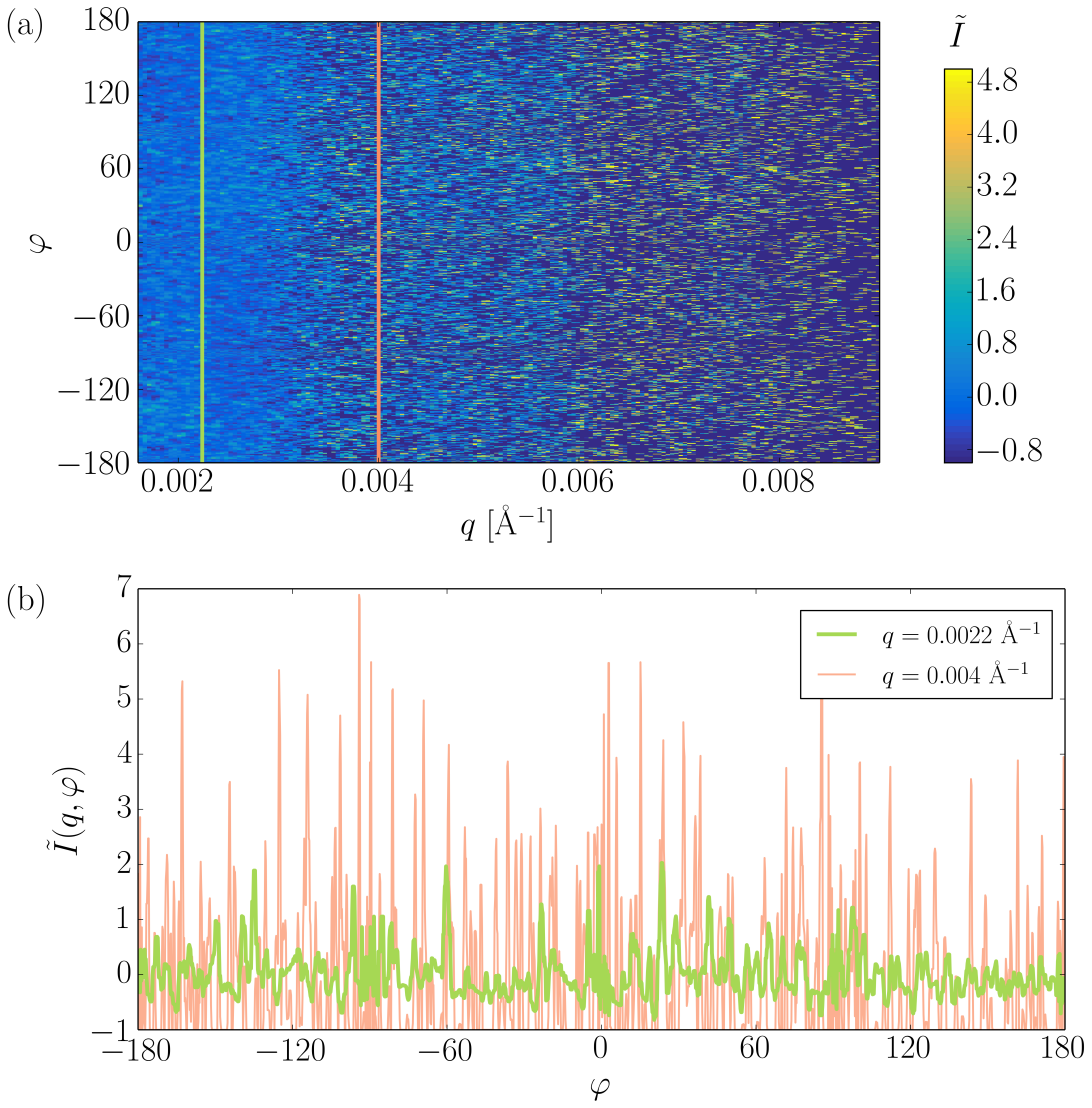

Figure C.2: (a) Normalized scattered intensity $\tilde{I}(q,\varphi)$. Color scale is saturated for better visualization. (b) Normalized scattered intensity $\tilde{I}(q,\varphi)$ as a function of azimuthal angle φ at two particular momentum transfer values q (see legend). The cross section positions are indicated by green and orange lines in (a).

and the results are presented in Fig. C.2. The resulting $\tilde{I}(q,\varphi)$ is shown as a function of momentum transfer q and azimuthal angle φ in Fig. C.2 (a). Although the normalization with eq. (C.1) ideally removes dependence of intensities on q, the modulation of $\tilde{I}(q,\varphi)$ in q is still observed. In Fig. C.2 (b) $\tilde{I}(q,\varphi)$ is shown as a function of azimuthal angle φ at two particular momentum transfers q. The relative deviation at higher momentum transfer q is more than $2-3$ times larger than at q_{peak}.

The intensities obtained after matching the standard deviation of intensity at all q to the one at q_{peak} are shown in Fig. C.3. The resulting intensity distribution $\hat{I}(q,\varphi)$ is much less dependent on q (see Fig. C.3 (a)) and standard deviation at different momentum transfers q has similar values (see Fig. C.3 (b)).

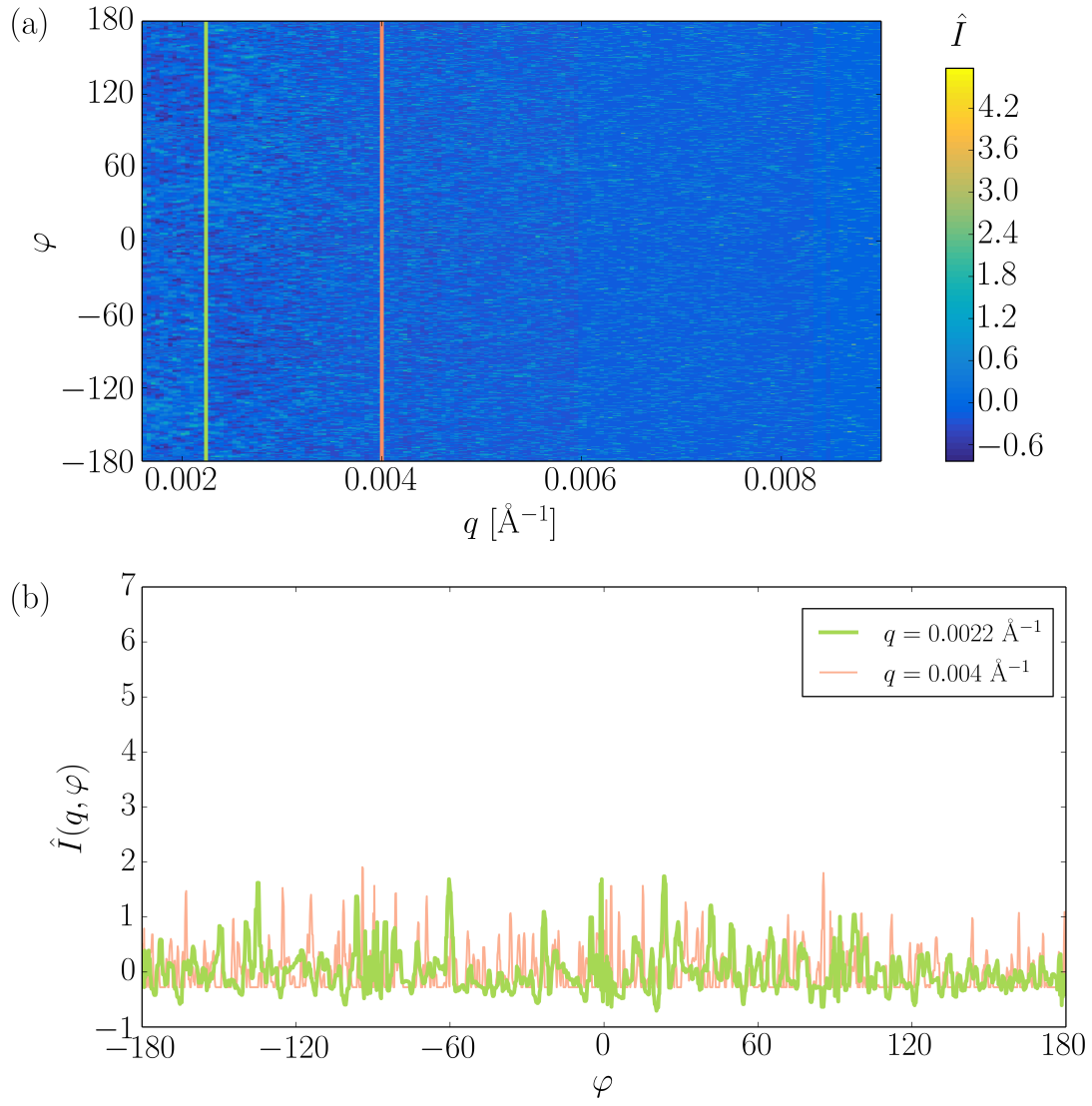

Figure C.3: (a) Normalized scattered intensity $\hat{I}(q,\varphi)$. (b) Normalized scattered intensity $\hat{I}(q,\varphi)$ as a function of azimuthal angle φ at two particular momentum transfer values q (see legend). The cross section positions are indicated by green and orange lines in (a).

The coefficients $\Psi_l(q)$ obtained with normalization on average intensities and with additional normalization on standard deviation are shown in Fig. C.4 (a) and (b), respectively. In Fig. C.4 (a) the amplitude of $\Psi_l(q)$ increases with q. The modulation on q in $\Psi_l(q)$ mirrors the modulation in $\tilde{I}(q,\varphi)$. The normalization on standard deviation insures a correct comparison of $\Psi_l(q)$ at different momentum transfers q.

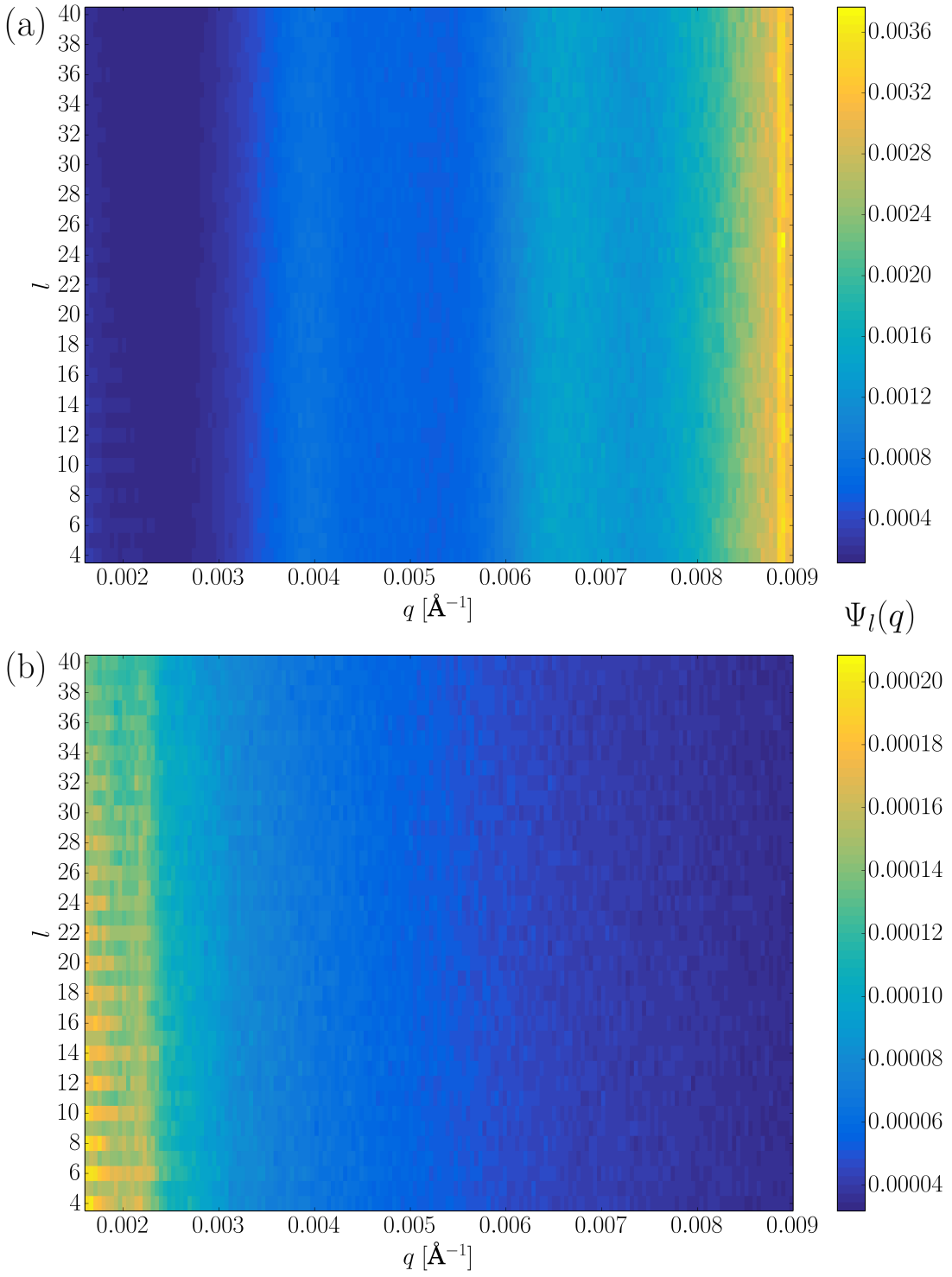

Figure C.4: Coefficient $\Psi_l(q)$ for sample PA-4 with volume fraction $\phi = 0.19$ as a function of component l and momentum transfer q obtained with normalization on average intensities (a) and with additional normalization on standard deviation (b).

BIBLIOGRAPHY

[1] D. H. Everett. Manual of symbols and terminology for physicochemical quantities and units, appendix ii: Definitions, terminology and symbols in colloid and surface chemistry. *Pure Appl. Chem.*, 31:577–638, 1972.

[2] E. Frey and K. Kroy. Brownian motion: a paradigm of soft matter and biological physics. *Ann. Phys.*, 14:20–50, 2005.

[3] M. Fanun. *The role of colloidal systems in environmental protection*. Elsevier, 2014.

[4] G. Konstantatos and E. H. Sargent. *Colloidal quantum dot optoelectronics and photovoltaics*. Cambridge University Press, 2013.

[5] S. P. Stoylov and M. V. Stoimenova. *Molecular and colloidal electro-optics*, volume 134. CRC Press, 2016.

[6] E. Matijevic. *Medical applications of colloids*. Springer, 2008.

[7] D. H. Everett. *Basic principles of colloid science*. Royal Society of Chemistry, 1988.

[8] J. Zinn-Justin, J. P. Hansen, and D. Levesque. Liquids, freezing and glass transition. *Les Houches Summer School (Amsterdam: North-Holland)*, 1991.

[9] W. Poon. Colloids as big atoms. *Science*, 304:830–831, 2004.

[10] S. Auer and D. Frenkel. Prediction of absolute crystal-nucleation rate in hard-sphere colloids. *Nature*, 409:1020–1023, 2001.

[11] K. Zahn and G. Maret. Dynamic criteria for melting in two dimensions. *Phys. Rev. Lett.*, 85:3656, 2000.

[12] T. Eckert and E. Bartsch. Re-entrant glass transition in a colloid-polymer mixture with depletion attractions. *Phys. Rev. Lett.*, 89:125701, 2002.

[13] N. R. Jana, L. Gearheart, and C. J. Murphy. Wet chemical synthesis of high aspect ratio cylindrical gold nanorods. *J. Phys. Chem. B*, 105:4065–4067, 2001.

[14] V. Malik, B. Grobety, V. Trappe, H. Dietsch, and P. Schurtenberger. A closer look at the synthesis and formation mechanism of hematite nanocubes. *Colloids Surf., A*, 445:21–29, 2014.

[15] N. Nun, S. Hinrichs, M. A. Schroer, D. Sheyfer, G. GrÃijbel, and B. Fischer. Tuning the size of thermoresponsive poly(n-isopropyl acrylamide) grafted silica microgels. *Gels*, 3:34, 2017.

[16] P. N. Pusey. Colloidal suspensions. *Liquids, Freezing and Glass Transition*, 1991.

[17] H. C. Hamaker. The London – van der Waals attraction between spherical particles. *Physica*, 4:1058–1072, 1937.

[18] N. I. Lebovka. *Aggregation of charged colloidal particles*. Springer, 2012.

[19] P. N. Pusey, E. Zaccarelli, C. Valeriani, E. Sanz, W. C. Poon, and M. E. Cates. Hard spheres: crystallization and glass formation. *Phil. Trans. R. Soc. A*, 367:4993–5011, 2009.

[20] A. Stradner, H. Sedgwick, F. Cardinaux, and W. C. Poon. Equilibrium cluster formation in concentrated protein solutions and colloids. *Nature*, 432:492, 2004.

[21] P. N. Pusey and W. Van Megen. Phase behaviour of concentrated suspensions of nearly hard colloidal spheres. *Nature*, 320:340–342, 1986.

[22] E. B. Sirota, H. D. Ou-Yang, S. K. Sinha, P. M. Chaikin, J. D. Axe, and Y. Fujii. Complete phase diagram of a charged colloidal system: A synchrotron x-ray scattering study. *Phys. Rev. Lett.*, 62:1524–1527, 1989.

[23] T. Kanai, N. Boon, P. J. Lu, E. Sloutskin, A. B. Schofield, F. Smallenburg, R. Van Roij, M. Dijkstra, and D. A. Weitz. Crystallization and reentrant melting of charged colloids in nonpolar solvents. *Phys. Rev. E*, 91, 2015.

[24] W. W. Wood and J. D. Jacobson. Preliminary results from a recalculation of the monte carlo equation of state of hard spheres. *J. Chem. Phys.*, 27:1207–1208, 1957.

[25] B. J. Alder and T. Wainwright. Phase transition for a hard sphere system. *J. Chem. Phys.*, 27:1208–1209, 1957.

[26] W. G. Hoover and F. H. Ree. Melting transition and communal entropy for hard spheres. *J. Chem. Phys.*, 49:3609–3617, 1968.

[27] F. F. Abraham. An isothermal-isobaric computer simulation of the supercooled-liquid/glass transition region: Is the short-range order in the amorphous solid fcc? *J. Chem. Phys.*, 72:359–365, 1980.

[28] P. N. Pusey and W. Van Megen. Observation of a glass transition in suspensions of spherical colloidal particles. *Phys. Rev. Lett.*, 59:2083, 1987.

[29] R. J. Speedy. The hard sphere glass transition. *Mol. Phys.*, 95:169–178, 1998.

[30] E. R. Weeks, J. C. Crocker, A. C. Levitt, A. Schofield, and D. A. Weitz. Three-dimensional direct imaging of structural relaxation near the colloidal glass transition. *Science*, 287:627–631, 2000.

[31] M. Fasolo and P. Sollich. Equilibrium phase behavior of polydisperse hard spheres. *Phys. Rev. Lett.*, 91:068301, 2003.

[32] P. Sollich and N. B. Wilding. Crystalline phases of polydisperse spheres. *Phys. Rev. Lett.*, 104:118302, 2010.

[33] G. L. Hunter and E. R. Weeks. The physics of the colloidal glass transition. *Rep. Prog. Phys.*, 75:066501, 2012.

[34] P. A. Hiltner and I. M. Krieger. Diffraction of light by ordered suspensions. *J. Phys. Chem.*, 73:2386–2389, 1969.

[35] A. Kose, M. Ozaki, K. Takano, Y. Kobayashi, and S. Hachisu. Direct observation of ordered latex suspension by metallurgical microscope. *J. Colloid Interface Sci.*, 44:330–338, 1973.

[36] Y. Monovoukas and A. P. Gast. The experimental phase diagram of charged colloidal suspensions. *J. Colloid Interface Sci.*, 128:533–548, 1989.

[37] A. Yethiraj and A. Van Blaaderen. A colloidal model system with an interaction tunable from hard sphere to soft and dipolar. *Nature*, 421:513–517, 2003.

[38] F. Smallenburg, N. Boon, M. Kater, M. Dijkstra, and R. Van Roij. Phase diagrams of colloidal spheres with a constant zeta-potential. *J. Chem. Phys.*, 134:074505, 2011.

[39] S. Hachisu, Y. Kobayashi, and A. Kose. Phase separation in monodisperse latexes. *J. Colloid Interface Sci.*, 42:342–348, 1973.

[40] S. Hachisu and Y. Kobayashi. Kirkwood-alder transition in monodisperse latexes. II. Aqueous latexes of high electrolyte concentration. *J. Colloid Interface Sci.*, 46:470–476, 1974.

[41] F. Westermeier, B. Fischer, W. Roseker, G. Grübel, G. Nägele, and M. Heinen. Structure and short-time dynamics in concentrated suspensions of charged colloids. *J. Chem. Phys.*, 137:114504, 2012.

[42] D. Hone, S. Alexander, P. M. Chaikin, and P. Pincus. The phase diagram of charged colloidal suspensions. *J. Chem. Phys.*, 79:1474–1479, 1983.

[43] M. O. Robbins, K. Kremer, and G. S. Grest. Phase diagram and dynamics of Yukawa systems. *J. Chem. Phys.*, 88:3286–3312, 1988.

[44] S. Hamaguchi, R. T. Farouki, and D. H. E. Dubin. Triple point of Yukawa systems. *Phys. Rev. E*, 56:4671–4682, 1997.

[45] A. Hynninen and M. Dijkstra. Phase diagrams of hard-core repulsive Yukawa particles. *Phys. Rev. E*, 68:021407, 2003.

[46] C. L. Klix, C. P. Royall, and H. Tanaka. Structural and Dynamical Features of Multiple Metastable Glassy States in a Colloidal System with Competing Interactions. *Phys. Rev. Lett.*, 104:165702, 2010.

[47] J. X. Liu and Y. F. Men. Phase behavior of charge stablized colloid dispersion with added water soluble polymers. *Chin. J. Polym. Sci.*, 31:1218–1224, 2013.

[48] W. C. Röntgen. Über eine neue Art von Strahlen. *Sitzungsberichte der Wuerzburger Physik.-medic. Gesellschaft*, 1895.

[49] O. Glatter and O. Kratky. *Small angle X-ray scattering*. Academic press, 1982.

[50] J. Als-Nielsen and D. McMorrow. *Elements of modern X-ray physics*. John Wiley & Sons, 2011.

[51] D. Paganin. *Coherent X-ray optics*. Oxford University Press on Demand, 2006.

[52] D. Levy and M. Zayat. *The Sol-Gel Handbook: Synthesis, Characterization and Applications.* John Wiley & Sons, 2015.

[53] A. Guinier. Structure of age-hardened aluminium-copper alloys. *Nature*, 142:569–570, 1938.

[54] A. Guinier and G. Fournet. Scattering of x-rays, 1955.

[55] D. I. Svergun L. A. Feigin and G. W. Taylor. *Structure analysis by small-angle X-ray and neutron scattering*. Springer, 1987.

[56] H. Schnablegger and Y. Singh. The SAXS Guide. *Anton Paar GmbH*, 2013.

[57] H. Brumberger. *Modern aspects of small-angle scattering*, volume 451. Springer Science & Business Media, 2013.

[58] B. R. Pauw. Everything SAXS: small-angle scattering pattern collection and correction. *J. Phys.: Condens. Matter*, 25:383201, 2013.

[59] T. Li, A. J. Senesi, and B. Lee. Small angle x-ray scattering for nanoparticle research. *Chem. Rev.*, 116:11128–11180, 2016.

[60] R. Hosemann and S. N. Bagchi. *Direct analysis of diffraction by matter*. North-Holland Pub. Co., 1962.

[61] J. S. Pedersen. Determination of size distribution from small-angle scattering data for systems with effective hard-sphere interactions. *J. Appl. Crystallogr.*, 27:595–608, 1994.

[62] W. H. De Jeu. *Basic X-ray Scattering for Soft Matter*. Oxford University Press, 2016.

[63] L. S. Ornstein and F. Zernike. Accidental deviations of density and opalescence at the critical point of a single substance. *Proc. Acad. Sci. Amsterdam*, 17:793–806, 1914.

[64] J. S. Høye and L. Blum. Solution of the yukawa closure of the ornstein-zernike equation. *J. Stat. Phys.*, 16:399–413, 1977.

[65] Y. Liu, E. Fratini, P. Baglioni, W. Chen, and S. Chen. Effective long-range attraction between protein molecules in solutions studied by small angle neutron scattering. *Phys. Rev. Lett.*, 95:118102, 2005.

[66] M. A. Schroer, C. Gutt, F. Lehmkühler, B. Fischer, I. Steinke, F. Westermeier, M. Sprung, and G. Grübel. Nano-beam x-ray microscopy of dried colloidal films. *Soft Matter*, 11:5465–5472, 2015.

[67] F. Lehmkühler, C. Gutt, B. Fischer, L. Müller, B. Ruta, M. A. Schroer, D. Sheyfer, M. Sprung, K. Tono, T. Katayama, M. Yabashi, T. Ishikawa, and G. Grübel. Short and medium range order in glass- and crystal-forming hard-sphere systems. *In preparation*.

[68] E. Weckert. The potential of future light sources to explore the structure and function of matter. *IUCrJ*, 2:230–245, 2015.

[69] A. G. Shabalin, J. M. Meijer, R. Dronyak, O. M. Yefanov, A. Singer, R. P. Kurta, U. Lorenz, O. Yu. Gorobtsov, D. Dzhigaev, S. Kalbfleisch, J. Gulden, A. V. Zozulya, M. Sprung, A. V. Petukhov, and I. A. Vartanyants. Revealing three-dimensional structure of an individual colloidal crystal grain by coherent x-ray diffractive imaging. *Phys. Rev. Lett.*, 117:138002, 2016.

[70] A. V. Martin, A. J. D'Alfonso, F. Wang, R. Bean, F. Capotondi, R. A. Kirian, E. Pedersoli, L. Raimondi, F. Stellato, and C. H. Yoon. X-ray holography with a customizable reference. *Nat. Commun.*, 5, 2014.

[71] D. Dzhigaev. *Characterization of nanowires by coherent x-ray diffractive imaging and ptychography*. PhD thesis, 2017.

[72] G. Grübel and F. Zontone. Correlation spectroscopy with coherent X-rays. *J. Alloys Compd.*, 362:3–11, 2004.

[73] Z. Kam. Determination of Macromolecular Structure in Solution by Spatial Correlation of Scattering Fluctuations. *Macromolecules*, 10:927–934, 1977.

[74] P. Wochner, C. Gutt, T. Autenrieth, T. Demmer, V. Bugaev, A. D. Ortiz, A. Duri, F. Zontone, G. Grübel, and H. Dosch. X-ray cross correlation analysis uncovers hidden local symmetries in disordered matter. *Proc. Natl. Acad. Sci. U.S.A.*, 106:11511–11514, 2009.

[75] M. J. Beran and G. B. Jr. Parrent. *Theory of partial coherence.* 1964.

[76] J. W. Goodman. *Statistical optics.* 1985.

[77] L. Mandel and E. Wolf. *Optical coherence and quantum optics.* 1995.

[78] M. Born and E. Wolf. *Principles of optics (7th (expanded) ed.).* 1999.

[79] B. J. Berne and R. Pecora. *Dynamic light scattering: with applications to chemistry, biology, and physics*. Courier Corporation, 1976.

[80] M. Sutton, S. G. J. Mochrie, T. Greytak, S. E. Nagler, L. E. Berman, G. Held, and G. B. Stephenson. Observation of speckle by diffraction with coherent X-rays, 1991.

[81] E. R. Pike and J. B. Abbiss. *Light scattering and photon correlation spectroscopy*, volume 40. Springer Science & Business Media, 2012.

[82] G. Grübel, G. B. Stephenson, C. Gutt, H. Sinn, and Th. Tschentscher. XPCS at the European X-ray free electron laser facility. *Nucl. Instrum. Methods Phys. Res., Sect. B*, 262:357 – 367, 2007.

[83] S. B. Dierker, R. Pindak, R. M. Fleming, I. K. Robinson, and L. Berman. X-ray Photon Correlation Spectroscopy Study of Brownian Motion of Gold Colloids in Glycerol. *Phys. Rev. Lett.*, 75:449–452, 1995.

[84] O. G. Shpyrko. X-ray photon correlation spectroscopy. *IUCrJ*, 21:1057–1064, 2014.

[85] G. Grübel, D. Abernathy, G. B. Stephenson, S. Brauer, I. McNulty, S. G. J. Mochrie, B. McClain, A. Sandy, M. Sutton, E. Dufresne, I. K. Robinson, R. Fleming, R. Pindak, and S. Dierker. Intensity fluctuation spectroscopy using coherent X-rays. *ESRF Newsletter*, 23:14–16, 1995.

[86] S. Brauer, G. B. Stephenson, M. Sutton, R. Brüning, E. Dufresne, S. G. J. Mochrie, G. Grübel, J. Als-Nielsen, and D. L. Abernathy. X-ray Intensity Fluctuation Spectroscopy observations of critical dynamics in Fe_3Al. *Phys. Rev. Lett.*, 74:2010–2013, 1995.

[87] T. Thurn-Albrecht, W. Steffen, A. Patkowski, G. Meier, E. W. Fischer, G. Grübel, and D. L. Abernathy. Photon correlation spectroscopy of colloidal palladium using a coherent X-ray beam. *Phys. Rev. Lett.*, 77:5437–5440, 1996.

[88] O. K. C. Tsui and S. G. J. Mochrie. Dynamics of concentrated colloidal suspensions probed by X-ray correlation spectroscopy. *Phys. Rev. E*, 57:2030–2034, 1998.

[89] L. B. Lurio, D. Lumma, A. R. Sandy, M. A. Borthwick, P. Falus, S. G. J. Mochrie, J. F. Pelletier, M. Sutton, L. Regan, A. Malik, and G. B. Stephenson. Absence of scaling for the intermediate scattering function of a hard-sphere suspension: Static and dynamic X-ray scattering from concentrated polystyrene latex spheres. *Phys. Rev. Lett.*, 84:785–788, 2000.

[90] J. Lal, D. Abernathy, L. Auvray, O. Diat, and G. Grübel. Dynamics and correlations in magnetic colloidal systems studied by X-ray photon correlation spectroscopy. *Eur. Phys. J. E*, 4:263–271, 2001.

[91] D. Pontoni, T. Narayanan, J. M. Petit, G. Grübel, and D. Beysens. Microstructure and dynamics near an attractive colloidal glass transition. *Phys. Rev. Lett.*, 90:188301, 2003.

[92] R. Bandyopadhyay, D. Liang, H. Yardimci, D. A. Sessoms, M. A. Borthwick, S. G. J. Mochrie, J. L. Harden, and R. L. Leheny. Evolution of particle-scale dynamics in an aging clay suspension. *Phys. Rev. Lett.*, 93:228302, 2004.

[93] A. Robert, J. Wagner, T. Autenrieth, W. Härtl, and G. Grübel. Coherent X-rays as a new probe for the investigation of the dynamics of opaque colloidal suspensions. *J. Magn. Magn. Mater.*, 289:47–49, 2005.

[94] A. Fluerasu, A. Moussaïd, A. Madsen, and A. Schofield. Slow dynamics and aging in colloidal gels studied by X-ray photon correlation spectroscopy. *Phys. Rev. E*, 76:010401, 2007.

[95] X. Lu, S. G. J. Mochrie, S. Narayanan, A. R. Sandy, and M. Sprung. How a liquid becomes a glass both on cooling and on heating. *Phys. Rev. Lett.*, 100:045701, 2008.

[96] E. Wandersman, A. Duri, A. Robert, E. Dubois, V. Dupuis, and R. Perzynski. Probing heterogeneous dynamics of a repulsive colloidal glass by time resolved X-ray correlation spectroscopy. *J. Phys.: Condens. Matter*, 20:155104, 2008.

[97] C. Caronna, Yu. Chushkin, A. Madsen, and A. Cupane. Dynamics of nanoparticles in a supercooled liquid. *Phys. Rev. Lett.*, 100:055702, 2008.

[98] A. Robert, J. Wagner, W. Härtl, T. Autenrieth, and G. Grübel. Dynamics in dense suspensions of charge-stabilized colloidal particles. *Eur. Phys. J. E*, 25:77–81, 2008.

[99] E. M. Herzig, A. Robert, D. D. Van 't Zand, L. Cipelletti, P. N. Pusey, and P. S. Clegg. Dynamics of a colloid-stabilized cream. *Phys. Rev. E*, 79:011405, 2009.

[100] A. Duri, T. Autenrieth, L. M. Stadler, O. Leupold, Yu. Chushkin, G. Grübel, and C. Gutt. Two-dimensional heterogeneous dynamics at the surface of a colloidal suspension. *Phys. Rev. Lett.*, 102:145701, 2009.

[101] A. Fluerasu, P. Kwasniewski, C. Caronna, F. Destremaut, J. B. Salmon, and A. Madsen. Dynamics and rheology under continuous shear flow studied by X-ray photon correlation spectroscopy. *New J. Phys.*, 12:035023, 2010.

[102] X. Lu, S. G. J. Mochrie, S. Narayanan, A. R. Sandy, and M. Sprung. Temperature-dependent structural arrest of silica colloids in a water-lutidine binary mixture. *Soft Matter*, 6:6160–6177, 2010.

[103] B. Fischer, J. Wagner, C. Gutt, F. Westermeier, and G. Grübel. Structure and dynamics of glassy charged colloids studied with coherent small angle X-ray scattering. *J. Phys. Conf. Ser.*, 247:012026, 2010.

[104] K. Laszlo, A. Fluerasu, A. Moussaid, and E. Geissler. Deswelling kinetics of PNIPA gels. *Soft Matter*, 6:4335–4338, 2010.

[105] M. Sikorski, A. R. Sandy, and S. Narayanan. Depletion-induced structure and dynamics in bimodal colloidal suspensions. *Phys. Rev. Lett.*, 106:188301, 2011.

[106] M. Spannuth, S. G. J. Mochrie, S. S. L. Peppin, and J. S. Wettlaufer. Dynamics of colloidal particles in ice. *J. Chem. Phys.*, 135:224706, 2011.

[107] H. Guo, S. Ramakrishnan, J. L. Harden, and R. L. Leheny. Gel formation and aging in weakly attractive nanocolloid suspensions at intermediate concentrations. *J. Chem. Phys.*, 135:154903, 2011.

[108] D. Orsi, A. Fluerasu, A. Moussaïd, F. Zontone, L. Cristofolini, and A. Madsen. Dynamics in dense hard-sphere colloidal suspensions. *Phys. Rev. E*, 85:011402, 2012.

[109] P. Kwasniewski, A. Fluerasu, and A. Madsen. Anomalous dynamics at the hard-sphere glass transition. *Soft Matter*, 10:8698–8704, 2014.

[110] R. Angelini, A. Madsen, A. Fluerasu, G. Ruocco, and B. Ruzicka. Aging behavior of the localization length in a colloidal glass. *Colloids Surf., A*, 460:118 – 122, 2014.

[111] R. Angelini and B. Ruzicka. Non-diffusive dynamics in a colloidal glass: Aging versus rejuvenation. *Colloids Surf., A*, 483:316–320, 2015.

[112] Z. H. Cai, B. Lai, W. B. Yun, I. McNulty, K. G. Huang, and T. R. Russell. Observation of X-ray speckle by coherent scattering at grazing incidence. *Phys. Rev. Lett.*, 73:82–85, 1994.

[113] S. G. J. Mochrie, A. M. Mayes, A. R. Sandy, M. Sutton, S. Brauer, G. B. Stephenson, D. L. Abernathy, and G. Grübel. Dynamics of block copolymer micelles revealed by X-Ray intensity fluctuation spectroscopy. *Phys. Rev. Lett.*, 78:1275–1278, 1997.

[114] H. Kim, A. Rühm, L. B. Lurio, J. K. Basu, J. Lal, D. Lumma, S. G. J. Mochrie, and S. K. Sinha. Surface dynamics of polymer films. *Phys. Rev. Lett.*, 90:068302, 2003.

[115] K. Hyunjung, A. Rühm, L. B. Lurio, J. K. Basu, J. Lal, S. G. J. Mochrie, and S. K. Sinha. X-ray photon correlation spectroscopy on polymer films with molecular weight dependence. *Physica B*, 336:211 – 215, 2003.

[116] H. Kim, A. Rühm, L. B. Lurio, J. K. Basu, J. Lal, S. G. J. Mochrie, and S. K. Sinha. Synchrotron radiation studies of the dynamics of polymer films. *J. Phys.: Condens. Matter*, 16:S3491, 2004.

[117] P. Falus, M. A. Borthwick, and S. G. J. Mochrie. Fluctuation dynamics of block copolymer vesicles. *Phys. Rev. Lett.*, 94:016105, 2005.

[118] S. Narayanan, D. R. Lee, A. Hagman, X. Li, and J. Wang. Particle dynamics in polymer-metal nanocomposite thin films on nanometer-length scales. *Phys. Rev. Lett.*, 98:185506, 2007.

[119] S. Srivastava, A. K. Kandar, J. K. Basu, M. K. Mukhopadhyay, L. B. Lurio, S. Narayanan, and S. K. Sinha. Complex dynamics in polymer nanocomposites. *Phys. Rev. E*, 79:021408, 2009.

[120] A. K. Kandar, S. Srivastava, J. K. Basu, M. K. Mukhopadhyay, S. Seifert, and S. Narayanan. Unusual dynamical arrest in polymer grafted nanoparticles. *J. Chem. Phys.*, page 121102, 2009.

[121] H. Guo, G. Bourret, M. K. Corbierre, S. Rucareanu, R. B. Lennox, K. Laaziri, L. Piche, M. Sutton, J. L. Harden, and R. L. Leheny. Nanoparticle motion within glassy polymer melts. *Phys. Rev. Lett.*, 102:075702, 2009.

[122] O. Czakkel and A. Madsen. Evolution of dynamics and structure during formation of a cross-linked polymer gel. *Europhys. Lett.*, 95:28001, 2011.

[123] H. Guo, G. Bourret, R. B. Lennox, M. Sutton, J. L. Harden, and R. L. Leheny. Entanglement-controlled subdiffusion of nanoparticles within concentrated polymer solutions. *Phys. Rev. Lett.*, 109:055901, 2012.

[124] R. Hernández, A. Nogales, M. Sprung, C. Mijangos, and T. A. Ezquerra. Slow dynamics of nanocomposite polymer aerogels as revealed by x-ray photocorrelation spectroscopy (XPCS). *J. Chem. Phys.*, 140:024909, 2014.

[125] H. Conrad, F. Lehmkühler, B. Fischer, F. Westermeier, M. A. Schroer, Yu. Chushkin, C. Gutt, M. Sprung, and G. Grübel. Correlated heterogeneous dynamics in glass-forming polymers. *Phys. Rev. E*, 91:042309, 2015.

[126] A. Nogales and A. Fluerasu. X-ray Photon Correlation Spectroscopy for the study of polymer dynamics. *Eur. Polym. J.*, 81:494–504, 2016.

[127] F. Livet, F. Bley, J. P. Simon, R. Caudron, J. Mainville, M. Sutton, and D. Lebolloch. Statics and kinetics of the ordering transition in the $AuAgZn_2$ alloy. *Phys. Rev. B*, 66:134108, 2002.

[128] A. Fluerasu, M. Sutton, and E. M. Dufresne. X-ray Intensity Fluctuation Spectroscopy studies on phase-ordering systems. *Phys. Rev. Lett.*, 94:055501, 2005.

[129] M. Leitner, B. Sepiol, L. M. Stadler, B. Pfau, and G. Vogl. Atomic diffusion studied with coherent X-rays. *Nat. Mater.*, 8:717–720, 2009.

[130] L. Müller, M. Waldorf, C. Gutt, G. Grübel, A. Madsen, T. R. Finlayson, and U. Klemradt. Slow aging dynamics and avalanches in a gold-cadmium alloy investigated by X-Ray photon correlation spectroscopy. *Phys. Rev. Lett.*, 107:105701, 2011.

[131] M. Leitner, B. Sepiol, L. M. Stadler, and B. Pfau. Time-resolved study of the crystallization dynamics in a metallic glass. *Phys. Rev. B*, 86:064202, 2012.

[132] S. O. Hruszkewycz, M. Sutton, P. H. Fuoss, B. Adams, S. Rosenkranz, J. K. F. Ludwig, W. Roseker, D. Fritz, M. Cammarata, and D. Zhu. High contrast X-ray speckle from atomic-scale order in liquids and glasses. *Phys. Rev. Lett.*, 109:185502, 2012.

[133] B. Ruta, Yu. Chushkin, G. Monaco, L. Cipelletti, E. Pineda, P. Bruna, V. M. Giordano, and M. Gonzalez-Silveira. Atomic-scale relaxation dynamics and aging in a metallic glass probed by X-Ray photon correlation spectroscopy. *Phys. Rev. Lett.*, 109:165701, 2012.

[134] B. Ruta, G. Baldi, G. Monaco, and Yu. Chushkin. Compressed correlation functions and fast aging dynamics in metallic glasses. *J. Chem. Phys.*, 138:054508, 2013.

[135] A. Madsen, J. Als-Nielsen, and G. Grübel. Viscosity of a liquid crystal near the nematic–smectic a phase transition. *Phys. Rev. Lett.*, 90:085701, 2003.

[136] I. Sikharulidze, B. Farago, I. P. Dolbnya, A. Madsen, and W. H. De Jeu. Surface and bulk elasticity determined fluctuation regimes in smectic membranes. *Phys. Rev. Lett.*, 91:165504, 2003.

[137] D. D. Van't Zand, Yu. Chushkin, L. Belkoura, C. V. Lobo, R. Strey, K. Lyakhova, and P. S. Clegg. Anisotropic dynamics of the tenuous gel in a liquid crystal–nanoparticle composite. *Soft Matter*, 8:4062–4066, 2012.

[138] O. G. Shpyrko, E. D. Isaacs, J. M. Logan, Y. Feng, G. Aeppli, R. Jaramillo, H. C. Kim, T. F. Rosenbaum, P. Zschack, and M. Sprung. Direct measurement of antiferromagnetic domain fluctuations. *Nature*, 447:68–71, 2007.

[139] S. W. Chen, H. Guo, K. A. Seu, K. Dumesnil, S. Roy, and S. K. Sinha. Jamming behavior of domains in a spiral antiferromagnetic system. *Phys. Rev. Lett.*, 110:217201, 2013.

[140] Q. Zhang, E. M. Dufresne, P. Chen, J. Park, M. P. Cosgriff, M. Yusuf, Y. Dong, D. D. Fong, H. Zhou, Z. Cai, R. J. Harder, S. J. Callori, M. Dawber, P. G. Evans, and A. R. Sandy. Thermal fluctuations of ferroelectric nanodomains in a ferroelectric-dielectric $\mathrm{PbTiO_3/SrTiO_3}$ superlattice. *Phys. Rev. Lett.*, 118:097601, 2017.

[141] C. Gutt, T. Ghaderi, V. Chamard, A. Madsen, T. Seydel, M. Tolan, M. Sprung, G. Grübel, and S. K. Sinha. Observation of heterodyne mixing in surface X-ray photon correlation spectroscopy experiments. *Phys. Rev. Lett.*, 91:076104, 2003.

[142] A. Madsen, T. Seydel, M. Sprung, C. Gutt, M. Tolan, and G. Grübel. Capillary waves at the transition from propagating to overdamped behavior. *Phys. Rev. Lett.*, 92:096104, 2004.

[143] A. Malik, A. R. Sandy, L. B. Lurio, G. B. Stephenson, S. G. J. Mochrie, I. McNulty, and M. Sutton. Coherent X-ray study of fluctuations during domain coarsening. *Phys. Rev. Lett.*, 81:5832, 1998.

[144] Yu. Chushkin, C. Caronna, and A. Madsen. A novel event correlation scheme for X-ray photon correlation spectroscopy. *J. Appl. Crystallogr.*, 45:807–813, 2012.

[145] M. Sutton. A review of X-ray intensity fluctuation spectroscopy. *C. R. Phys.*, 9:657 – 667, 2008.

[146] R. L. Leheny. XPCS: Nanoscale motion and rheology. *Curr. Opin. Colloid Interface Sci.*, 17:3–12, 2012.

[147] I. Snook, W. Van Megen, and R. J. A. Tough. Diffusion in concentrated hard sphere dispersions: Effective two particle mobility tensors. *J. Chem. Phys.*, 78:5825–5836, 1983.

[148] M. D. Ediger. Spatially heterogeneous dynamics in supercooled liquids. *Annu. Rev. Phys. Chem.*, 51:99–128, 2000.

[149] N. A. Clark, B. J. Ackerson, and A. J. Hurd. Multidetector scattering as a probe of local structure in disordered phases. *Phys. Rev. Lett.*, 50:1459–1462, 1983.

[150] B. J. Ackerson and N. A. Clark. Cross-correlation intensity fluctuation spectroscopy applied to colloidal suspensions. *Faraday Discuss. Chem. Soc.*, 76:219–228, 1983.

[151] P. N. Pusey and J. G. Rarity. Measurement of higher-order correlation functions by intensity cross-correlation light scattering. *Le Journal de Physique Colloques*, 46:43, 1985.

[152] W. G. Griffin and P. N. Pusey. Anticorrelations in light scattered by nonspherical particles. *Phys. Rev. Lett.*, 43:1100–1104, 1979.

[153] Z. Kam. The reconstruction of structure from electron micrographs of randomly oriented particles. *J. Theor. Biol.*, 82:15–39, 1980.

[154] Z. Kam, I. Gafni, and M.b M. Kessel. Enhancement of two-dimensional projections from electron microscope images using spatial correlations. *Ultramicroscopy*, 7:311–320, 1982.

[155] T. Latychevskaia, G. F. Mancini, and F. Carbone. The role of the coherence in the cross-correlation analysis of diffraction patterns from two-dimensional dense mono-disperse systems. *Sci. Rep.*, 5:16573, 2015.

[156] O. Yu. Gorobtsov, G. Mercurio, G. Brenner, U. Lorenz, N. Gerasimova, R. P. Kurta, F. Hieke, P. Skopintsev, I. Zaluzhnyy, S. Lazarev, D. Dzhigaev, M. Rose, A. Singer, W. Wurth, and I. A. Vartanyants. Statistical properties of a free-electron laser revealed by hanbury brown–twiss interferometry. *Phys. Rev. A*, 95:023843, 2017.

[157] D. K. Saldin, V. L. Shneerson, R. Fung, and A. Ourmazd. Structure of isolated biomolecules obtained from ultrashort x-ray pulses: Exploiting the symmetry of random orientations. *J. Phys.: Condens. Matter*, 21, March 2009.

[158] D. K. Saldin, V. L. Shneerson, M. R. Howells, S. Marchesini, H. N. Chapman, M. Bogan, D. Shapiro, R. A. Kirian, U. Weierstall, K. E. Schmidt, and J. C. H. Spence. Structure of a single particle from scattering by many particles randomly oriented about an axis: Toward structure solution without crystallization? *New J. Phys.*, 12, 2010.

[159] M. Altarelli, R. P. Kurta, and I. A. Vartanyants. X-ray cross-correlation analysis and local symmetries of disordered systems: General theory. *Phys. Rev. B*, 82:104207, 2010.

[160] M. Altarelli, R. P. Kurta, and I. A. Vartanyants. Erratum: X-ray cross-correlation analysis and local symmetries of disordered systems: General theory [phys. rev. b 82, 104207 (2010)]. *Phys. Rev. B*, 86:179904, 2012.

[161] R. P. Kurta, M. Altarelli, E. Weckert, and I. A. Vartanyants. X-ray cross-correlation analysis applied to disordered two-dimensional systems. *Phys. Rev. B*, 85, 2012.

[162] V. Elser. Three-dimensional structure from intensity correlations. *New J. Phys.*, 13:123014, 2011.

[163] P. Wochner, M. Castro-Colin, S. N. Bogle, and V. N. Bugaev. Of fluctuations and cross-correlations: Finding order in disorder. *Int. J. Mater. Res.*, 102:874–888, 2011.

[164] R. P. Kurta, Y. Chesnokov, E. Weckert, and I. A. Vartanyants. Cross-correlation analysis of X-ray scattering from oxygen clusters. *J. Phys. Conf. Ser.*, 463:012046, 2013.

[165] R. P. Kurta, M. Altarelli, and I. A. Vartanyants. X-ray cross-correlation analysis of disordered ensembles of particles: Potentials and limitations. *Adv. Condens. Matter Phys.*, 2013:959835, 2013.

[166] F. Lehmkühler, G. Grübel, and C. Gutt. Detecting orientational order in model systems by X-ray cross-correlation methods. *J. Appl. Crystallogr.*, 47:1315–1323, 2014.

[167] B. Pedrini, A. Menzel, V. A. Guzenko, C. David, R. Abela, and C. Gutt. Model-independent particle species disentanglement by X-ray cross-correlation scattering. *Sci. Rep.*, 7:45618, 2017.

[168] D. K. Saldin, H. C. Poon, V. L. Shneerson, M. Howells, C. N. Chapman, R. A. Kirian, K. E. Schmidt, and J. C. H. Spence. Beyond small-angle X-ray scattering: Exploiting angular correlations. *Phys. Rev. B*, 81:174105, 2010.

[169] M. J. Bogan, S. Boutet, A. Barty, W. H. Benner, M. Frank, L. Lomb, R. Shoeman, D. Starodub, M. M. Seibert, S. P. Hau-Riege, B. Woods, P. Decorwin-Martin, S. Bajt, J. Schulz, U. Rohner, B. Iwan, N. Timneanu, S. Marchesini, I. Schlichting, J. Hajdu, and H. N. Chapman. Single-shot femtosecond x-ray diffraction from randomly oriented ellipsoidal nanoparticles. *Phys. Rev. Spec. Top. Accel Beams*, 13:094701, 2010.

[170] D. K. Saldin, H. C. Poon, M. J. Bogan, S. Marchesini, D. A. Shapiro, R. A. Kirian, U. Weierstall, and J. C. H. Spence. New light on disordered ensembles: Ab initio structure determination of one particle from scattering fluctuations of many copies. *Phys. Rev. Lett.*, 106:115501, 2011.

[171] R. A. Kirian. Structure determination through correlated fluctuations in x-ray scattering. *J. Phys. B*, 45, 2012.

[172] D. Starodub, A. Aquila, S. Bajt, M. Barthelmess, A. Barty, C. Bostedt, J. D. Bozek, N. Coppola, R. B. Doak, S. W. Epp, B. Erk, L. Foucar, L. Gumprecht, C. Y. Hampton, A. Hartmann, R. Hartmann, P. Holl, S. Kassemeyer, N. Kimmel, H. Laksmono, M. Liang, N. D. Loh, L. Lomb, A. V. Martin, K. Nass, C. Reich, D. Rolles, B. Rudek, A. Rudenko, J. Schulz, R. L. Shoeman, R. G. Sierra, H. Soltau, J. Steinbrener, F. Stellato, S. Stern, G. Weidenspointner, M. Frank, J. Ullrich, L. StrÃijder, I. Schlichting, H. N. Chapman, J. C. H. Spence, and M. J. Bogan. Single-particle structure determination by correlations of snapshot X-ray diffraction patterns. *Nat. Commun.*, 3:1–7, 2012.

[173] B. Pedrini, A. Menzel, M. Guizar-Sicairos, V. A. Guzenko, S. Gorelick, C. David, B. D. Patterson, and R. Abela. Two-dimensional structure from random multiparticle X-ray scattering images using cross-correlations. *Nat. Commun.*, 4:1–9, 2013.

[174] H. Liu, B. K. Poon, D. K. Saldin, J. C. H. Spence, and P. H. Zwart. Three-dimensional single-particle imaging using angular correlations from X-ray laser data. *Acta Cryst. A*, 69:1–9, 2013.

[175] G. Chen, P. H. Zwart, and D. Li. Component particle structure in heterogeneous disordered ensembles extracted from high-throughput fluctuation X-ray scattering. *Phys. Rev. Lett.*, 110:195501, 2013.

[176] R. A. Kirian and D. K. Saldin. Structure Determination from Disordered Ensembles of Identical Particles. *Synchrotron Radiat. News*, 26:20–25, 2013.

[177] E. Malmerberg, C. A. Kerfeld, and P. H. Zwart. Operational properties of fluctuation X-ray scattering data. *IUCrJ*, 2:309–316, 2015.

[178] H. C. Poon and D. K. Saldin. Use of triple correlations for the sign determinations of expansion coefficients of symmetric approximations to the diffraction volumes of regular viruses. *Structural Dynamics*, 2:4922476, 2015.

[179] R. P. Kurta. Multiple-wavelength resonant fluctuation X-ray scattering. *J. Phys. B*, 49:165001, 2016.

[180] S. Ma and H. Liu. Facilitating model reconstruction for single-particle scattering using small-angle X-ray scattering methods. *J. Appl. Crystallogr.*, 49:665–671, 2016.

[181] M. Uddin. Reconstructing three-dimensional helical structure with an X-ray free electron laser. *J. Appl. Crystallogr.*, 49:450–456, 2016.

[182] R. P. Kurta, R. Dronyak, M. Altarelli, E. Weckert, and I. A. Vartanyants. Solution of the phase problem for coherent scattering from a disordered system of identical particles. *New J. Phys.*, 15:013059, 2013.

[183] R. P. Kurta, B. I. Ostrovskii, A. Singer, O. Yu. Gorobtsov, A. G. Shabalin, D. Dzhigaev, O. M. Yefanov, A. V. Zozulya, M. Sprung, and I. A. Vartanyants. X-ray cross-correlation analysis of liquid crystal membranes in the vicinity of the hexatic-smectic phase transition. *Phys. Rev. E*, 88:044501, 2013.

[184] C. Gutt, L. Grodd, E. Mikayelyan, U. Pietsch, R. J. Kline, and S. Grigorian. Local orientational structure of a P3HT π-π Conjugated network investigated by X-ray nanodiffraction. *J. Phys. Chem. Lett.*, 5:2335–2339, 2014.

[185] R. P. Kurta, L. Grodd, E. Mikayelyan, O. Yu. Gorobtsov, I. Fratoddi, I. Venditti, M. Sprung, S. Grigorian, and I. A. Vartanyants. Structural properties of π-π conjugated network in polymer thin films studied by X-ray cross-correlation analysis. *J. Phys. Conf. Ser.*, 499:012021, 2014.

[186] M. A. Schroer, C. Gutt, and G. Grübel. Characteristics of angular cross correlations studied by light scattering from two-dimensional microsphere films. *Phys. Rev. E*, 90:012309, 2014.

[187] D. Mendez, T. J. Lane, J. Sung, J. Sellberg, C. Levard, H. Watkins, A. E. Cohen, M. Soltis, S. Sutton, J. Spudich, V. Pande, D. Ratner, and S. Doniach. Observation of correlated X-ray scattering at atomic resolution. *Philos. Trans. R. Soc. London, Ser. B*, 369:1–6, 2014.

[188] R. P. Kurta, L. Grodd, E. Mikayelyan, O. Yu. Gorobtsov, I. A. Zaluzhnyy, I. Fratoddi, I. Venditti, M. V. Russo, M. Sprung, I. A. Vartanyants, and S. Grigorian. Local structure of semicrystalline P3HT films probed by nanofocused coherent X-rays. *Phys. Chem. Chem. Phys.*, 17:7404–7410, 2015.

[189] I. A. Zaluzhnyy, R. P. Kurta, E. A. Sulyanova, O. Yu. Gorobtsov, A. G. Shabalin, A. V. Zozulya, A. P. Menushenkov, M. Sprung, B. I. Ostrovskii, and I. A. Vartanyants. Spatially resolved X-ray studies of liquid crystals with strongly developed bond-orientational order. *Phys. Rev. E*, 91:042506, 2015.

[190] F. Lehmkühler, and L. Müller B. Fischer, B. Ruta, and G. Grübel. Structure beyond pair correlations: X-ray crosscorrelation from colloidal crystals. *J. Appl. Crystallogr.*, 49:2046–2052, 2016.

[191] A. C. Y. Liu, R. F. Tabor, L. Bourgeois, M. D. De Jonge, S. T. Mudie, and T. C. Petersen. Calculation of Projected Bond-Orientational Order Parameters to Quantify Local Symmetries from Transmission Diffraction Data. *Phys. Rev. Lett.*, 116:205501, 2016.

[192] A. C. Liu, R. F. Tabor, L. Bourgeois, M. D. De Jonge, S. T. Mudie, and T. C. Petersen. Probing local order in glasses from limited-volume electron and x-ray diffraction. *J. Stat. Mech: Theory Exp.*, 2016, 2016.

[193] M. A. Schroer, F. Westermeier, F. Lehmkühler, H. Conrad, A. Schavkan, A. V. Zozulya, B. Fischer, W. Roseker, M. Sprung, C. Gutt, and G. Grübel. Colloidal crystallite suspensions studied by high pressure small angle X-ray scattering. *J. Chem. Phys.*, 144:4941563, 2016.

[194] I. A. Zaluzhnyy, R. P. Kurta, A. P. Menushenkov, B. I. Ostrovskii, and I. A. Vartanyants. Direct reconstruction of the two-dimensional pair distribution function in partially ordered systems with angular correlations. *Phys. Rev. E*, 94:030701, 2016.

[195] A. V. Martin. Orientational order of liquids and glasses via fluctuation diffraction. *IUCrJ*, 4:24–36, 2017.

[196] I. A. Zaluzhnyy, R. P. Kurta, E. A. Sulyanova, O. Yu. Gorobtsov, A. G. Shabalin, A. V. Zozulya, A. P. Menushenkov, M. Sprung, A. Krówczynski, E. Górecka, B. I. Ostrovskii, and I. A. Vartanyants. Structural studies of the bond-orientational order and hexatic-smectic transition in liquid crystals of various compositions. *Soft Matter*, page 00343, 2017.

[197] I. Zaluzhnyy, R. P. Kurta, A. André, O. Yu. Gorobtsov, M. Rose, P. Skopintsev, I. Besedin, A. V. Zozulya, M. Sprung, I. A. Vartanyants F. Schreiber, and M. Scheele. Quantifying angular correlations between the atomic lattice and superlattice of nanocrystals assembled with directional linking. *Nano Lett.*, pages 3511–3517, 2017.

[198] A. C. Y. Liu, R. F. Tabor, M. D. de Jonge, S. T. Mudie, and T. C. Petersen. Favored local structures in amorphous colloidal packings measured by microbeam x-ray diffraction. *Proceedings of the National Academy of Sciences*, page 201707198, 2017.

[199] E. Saldin, E. V. Schneidmiller, and M. V. Yurkov. *The physics of free electron lasers*. Springer Science & Business Media, 2013.

[200] M. A. Schroer, C. Gutt, F. Lehmkühler, B. Fischer, I. Steinke, F. Westermeier, M. Sprung, and G. Grübel. Nano-beam X-ray microscopy of dried colloidal films. *Soft Matter*, 11:5465–5472, 2015.

[201] K. A. Seu, S. Roy, R. Su, D. H. Parks, E. Shipton, E. E. Fullerton, and S. D. Kevan. Momentum transfer resolved memory in a magnetic system with perpendicular anisotropy. *Appl. Phys. Lett.*, 98:2569952, 2011.

[202] R. Su, K. A. Seu, D. Parks, J. J. Kan, E. E. Fullerton, S. Roy, and S. D. Kevan. Emergent rotational symmetries in disordered magnetic domain patterns. *Phys. Rev. Lett.*, 107:257204, 2011.

[203] K. Chesnel, J. Nelson, B. Wilcken, and S. D. Kevan. Mapping spatial and field dependence of magnetic domain memory by soft X-ray speckle metrology. *IUCrJ*, 19:293–306, 2012.

[204] R. P. Kurta, M. Altarelli, and I. A. Vartanyants. Structural analysis by X-ray intensity angular cross correlations. *Adv. Chem. Phys.*, 161:1, 2016.

[205] W. V. Smith and R. H. Ewart. Kinetics of emulsion polymerization. *J. Chem. Phys.*, 16:592–599, 1948.

[206] W. D. Harkins. A general theory of the mechanism of emulsion polymerization1. *J. Am. Chem. Soc.*, 69:1428–1444, 1947.

[207] E. Stettin K. Witkowski W. Hergeth, W. Lebek and K. Schmutzler. Particle formation in emulsion polymerization, 2. aggregation of primary particles. *Die Makromolekulare Chemie*, 193:1607–1621, 1992.

[208] F. K. Hansen and J. Ugelstad. Particle nucleation in emulsion polymerization. i. a theory for homogeneous nucleation. *J. Polym. Sci., Part A: Polym. Chem.*, 16:1953–1979, 1978.

[209] S. C. Thickett and R. G. Gilbert. Emulsion polymerization: state of the art in kinetics and mechanisms. *Polymer*, 48:6965–6991, 2007.

[210] C. D. Immanuel. Principles of polymerization-fourth edition by george odian. *AIChE J.*, 54:3029–3029, 2008.

[211] B. Fischer. Private communication.

[212] G. Grübel, J. Als-Nielsen, and A. K. Freund. The TROIKA beamline at ESRF. *Le Journal de Physique IV*, 4:9–27, 1994.

[213] M. Mattenet. Coherence preserving pseudo channel-cut monochromator at the esrf troika beamline. *MEDSI/Pan-American SRI 2008 Meeting*, 2008.

[214] R. Steinmann, Yu. Chushkin, C. Caronna, J. Chavanne, and A. Madsen. A small-angle scattering chamber for x-ray photon correlation spectroscopy at low temperatures. *Rev. Sci. Instrum.*, 82:025109, 2011.

[215] E. Thiele. Equation of state for hard spheres. *J. Chem. Phys.*, 39:474–479, 1963.

[216] T. Hao and R. E. Riman. Calculation of interparticle spacing in colloidal systems. *J. Colloid Interface Sci.*, 297:374–377, 2006.

[217] A. Madsen, A. Fluerasu, and B. Ruta. Structural dynamics of materials probed by X-ray photon correlation spectroscopy. *Synchrotron Light Sources and Free-Electron Lasers: Accelerator Physics, Instrumentation and Science Applications*, pages 1617–1641, 2016.

[218] P. Falus, L. B. Lurio, and S. G. J. Mochrie. Optimizing the signal-to-noise ratio for X-ray photon correlation spectroscopy. *Journal of synchrotron radiation*, 13:253–259, 2006.

[219] F. Ehrburger-Dolle, I. Morfin, F. Bley, F. Livet, G. Heinrich, S. Richter, L. Piché, and M. Sutton. Xpcs investigation of the dynamics of filler particles in stretched filled elastomers. *Macromolecules*, 45:8691–8701, 2012.

[220] Y. Shinohara, N. Yamamoto, H. Kishimoto, and Y. Amemiya. X-ray irradiation induces local rearrangement of silica particles in swollen rubber. *Journal of synchrotron radiation*, 22:119–123, 2015.

[221] D. Lumma, L. B. Lurio, S. G. J. Mochrie, and M. Sutton. Area detector based photon correlation in the regime of short data batches: Data reduction for dynamic X-ray scattering. *Rev. Sci. Instrum.*, 71:3274–3289, 2000.

[222] G. Brambilla, M. D. El, M. Pierno, L. Berthier, L. Cipelletti, G. Petekidis, and A. B. Schofield. Probing the equilibrium dynamics of colloidal hard spheres above the mode-coupling glass transition. *Phys. Rev. Lett.*, 102:085703, 2009.

[223] M. Leocmach and H. Tanaka. Roles of icosahedral and crystal-like order in hard spheres glass transition. *Nat. Commun.*, pages 1–8, 2012.

[224] J. Taffs, S. R. Williams, H. Tanaka, and C. P. Royall. Structure and kinetics in the freezing of nearly hard spheres. *Soft Matter*, 9:297–305, 2013.

[225] H. J. Schöpe, G. Bryant, and W. van Megen. Two-step crystallization kinetics in colloidal hard-sphere systems. *Phys. Rev. Lett.*, 96:175701, 2006.

[226] J. R. Savage and A. D. Dinsmore. Experimental evidence for two-step nucleation in colloidal crystallization. *Phys. Rev. Lett.*, 102:198302, 2009.

[227] J. Russo and H. Tanaka. The microscopic pathway to crystallization in supercooled liquids. *Sci. Rep.*, 2, 2012.

EIDESSTATTLICHE VERSICHERUNG

Hiermit erkläre ich an Eides statt, dass ich die vorliegende Dissertationsschrift selbst verfasst und keine anderen als die angegebenen Quellen und Hilfsmittel benutzt habe.

I hereby declare, on oath, that I have written the present dissertation by my own and have not used other than the acknowledged resources and aids.

Hamburg

Unterschrift (Signature) _____ D. Sheyfer

ACKNOWLEDGMENTS

I would like to acknowledge people who have supported and helped me – directly or indirectly – to make this project possible.

First, I would like to thank my supervisors Prof. Dr. Gerhard Grübel and Prof. Dr. Alf Mews, and also The Hamburg Centre for Ultrafast Imaging for giving me the opportunity to work on this project. I am thankful to Prof. Dr. Gerhard Grübel for his guidance and the invaluable support. I have benefited hugely from his enthusiasm, advice and trust during my time as his student.

I also would like to thank everyone in the Coherence X-ray Scattering group at DESY. Especially I am deeply thankful to Felix Lehmkühler for his help during the beamtime, a careful reading of the manuscript, many useful greenish notes, for his suggestions and advice, for valuable discussions and help with german language. Danke schön, Felix! I am very indebted to Birgit Fischer who opened for me DESY in 2012 being my supervisor during the summer student program. She introduced me to a colloidal production world – teaching me chemical 'cooking'. I am thankful for her advice and encouragement even after she moved on from the group. Thank you Birgit for your help during the beamtime, for many discussions and careful thesis reading.

I am grateful to people at ID10 beamline at ESRF who have always been willing to help during the experiments. I am especially very thankful to Yuriy Chushkin for his support during the experiment and good advice during my manuscript writing. I am also thankful to Martin A. Schroer for support at the ESRF experiment and enjoyable beamtime nightshifts.

Many thanks go to Michael Sprung for his fruitful suggestions with data analysis and helping with the matlab programming – thank you, Michael! I also would like to thank Fabian Westermeier for his help in fitting the data. Pawel Kwasniewski is gratefully acknowledged for help during the beamtime and introduction to ipython programming world. I am also thankful Avni Jain for good scientific discussions.

Colleagues, which I shared the office with – Magnus Berntsen, Martin A. Schroer, Joana Valerio, Michael Koof – I am very thankful for fruitful scientific and non-scientific enjoyable discussions. Thank you also for your understanding of my problem with very bright light. For enjoyable coffee mornings, I thank Irina and

Joana. I also would like to thank a brilliant secretary of our group – Donatella Rosetti – for her help with organization questions.

I am very grateful to all my friends who have supported me during phd. Your support and encouragement were worth more than I can express on paper, but I'll try.

Many thanks go to Oleg Gorobtsov for his enormous brilliant support with english wording and fruitful thesis discussions accompanied by a variety of different sorts of tea and TV-shows. Olelelelleg, spasibushki!

I am also very thankful to Anatoly Shabalin. Anatoly has always supported me in scientific and non-scientific questions. After leaving Hamburg he continues to support me in life from the other side of the ocean with a good advice and positive mood. Spasibo, Tolyan!

I thank Joaninha, who has supported me during my hard periods at work and has given me good advice in life. Obregadinho! I also thank Wojciech Roseker for good advice at work and his non-scientific support especially during my knee troubles.

Many thanks go to Ksenia Maximova, Dmitry Dzhigaev, Sergei Savin, Ivan Zaluzhnyy and Natalia Zolotova who also studied with me at "MEPhI" in Moscow. I was very happy and pleasantly surprised to find you in Hamburg. I also would like to thank my University friends in Moscow – Kirill Borodako, Ignat Moskalenko, Andrey Mikhaylyuk, Elena Selivanova, Lesya Korchuganova, Olga Svistunova – for their far-distance support and warmly visits in Hamburg.

I am grateful to all my relatives in the south of Germany as well as my uncle Albert and its family in Moscow for their support during my studies.

Maria Naumova and Carsten Richter, I thank you for preventing me from work all time and performing nice breaks with football, parkour, cycling, tatort evening. Ruslan Kurta, Olexander Yefanov, Alex Schavkan, Svitozar Serkez, Pavel Lytaev, Ruslan Khubbutdinov, Jana Tatur, Denis Veretennikov, Nastasia Mukharamova, Olga Merkulova, Igor Khokhriakov, Artur and Ksenia Lobanov – thank you for plenty of nice fruitful discussions with tea and not only with tea.

Especially, I would like to thank Rustam Rysov, Alexandra Tolsikova and Aram Kalaydzhyan for an enjoyable time in DESY, CFEL coffee&tea, many interesting trips and awesome holidays. I am grateful for your support in numerous scientific and non-scientific questions. Spasibo! Dyakuyu!

Last but not least I want to thank my grandmother Dina, and my parents – Viktor and Sveta – for all their love and support during my studies in last years. Spasibo vam bolshoe!